UNIVERSITÄT PADERBORN
Die Universität der Informationsgesellschaft

FAKULTÄT FÜR
ELEKTROTECHNIK,
INFORMATIK UND
MATHEMATIK

Time-Optimal Control of Synchronous Machines in the Whole Modulation Range Considering Current and Torque Constraints

Von der Fakultät für Elektrotechnik, Informatik und Mathematik
der Universität Paderborn

zur Erlangung des akademischen Grades

Doktor der Ingenieurwissenschaften (Dr.-Ing.)

genehmigte Dissertation
von

M.Sc. Anian Brosch

Erster Gutachter:	Prof. Dr.-Ing. Oliver Wallscheid
Zweiter Gutachter:	Assoc. Prof. Fabio Tinazzi
Dritter Gutachter:	Prof. Dr.-Ing. Joachim Böcker

Tag der mündlichen Prüfung: 24.07.2024

Kolbermoor 2024

Diss. EIM-E/379

Acknowledgments

This dissertation is the result of my work as a research associate at the Department of Power Electronics and Electrical Drives at the Paderborn University. Although the individual work of the doctoral student is the central element of any doctoral thesis, it is undisputed that the external conditions have a significant influence on the success or failure of the doctoral project. I would like to take this opportunity to thank all those who have contributed to this supportive environment.

First of all, I would like to thank Prof. Dr.-Ing. Joachim Böcker, now emeritus, for giving me the opportunity to conduct research in the field of electrical drives by employing me at his chair. My thanks also go to Prof. Dr.-Ing. Oliver Wallscheid, my direct supervisor and doctoral advisor, for his exemplary and intensive cooperation and the trust he placed in me. The sense for mathematically and linguistically precisely formulated statements that Mr. Böcker and Mr. Wallscheid conveyed to me has shaped and enriched me for life. I would like to express my deepest gratitude to Assoc. Prof. Fabio Tinazzi for the fruitful time during my research stay in Italy as well as for being the co-advisor of the doctoral thesis.

Furthermore, I would like to thank my colleagues for the professional and private time we spent together in Paderborn and for technical discussions until late at night as well as numerous bike rides.

Last but not least, I would like to thank my family and my girlfriend. They have always supported me unconditionally and provided an irreplaceable balance to my research activities.

Abstract

Improving the power and torque density as well as the control dynamics of electric drives are crucial targets for drive control algorithms to save weight and installation space. In order to fully exploit the potential of the electric drive during transient and steady-state operation for a given maximum current and DC-link voltage, a continuous control set model predictive flux control (CCS-MPFC) scheme for synchronous machines (SM) is presented. The CCS-MPFC is able to reach operating points for given reference torques in the shortest possible time, i.e., time-optimal control (TOC) performance, while preventing transient overcurrents as well as torque overshoots and undershoots. In addition, the entire speed and modulation range of the inverter, from linear modulation to overmodulation, including six-step operation, can be seamlessly utilized to its maximum extent. To maintain control accuracy, the (nonlinear) flux linkage maps of the SM are continuously corrected during operation at sufficiently high speeds to compensate for temperature changes, manufacturing deviations, and aging effects.

A seamless transition to the overmodulation range is enabled by the proposed harmonic reference generator (HRG) and pulse clipping (PC) scheme. The HRG calculates and adds harmonic components induced by the voltage hexagon in the overmodulation range to the mean flux linkage reference of the CCS-MPFC. Specific switching behavior and inverter states in the overmodulation range, e.g., six-step operation, are ensured by the PC scheme. This results in approx. 10 % higher power of the drive above the nominal speed compared to drive control schemes that are limited to the linear modulation range, e.g., proportional-integral field-oriented control (PI-FOC). Although the HRG and PC maximize the voltage utilization during steady-state operation, time-suboptimal control results during transient operation.

Using Pontryagin's principle, the TOC problem for SMs without consideration of current and torque limits is solved during online operation and incorporated via a pre-rotation of the reference flux linkage in the stator-fixed coordinate system of the CCS-MPFC. To prevent transient overcurrents as well as torque overshoots and undershoots, current and torque limits are incorporated via state constraints of the CCS-MPFC. Here, the time to reach the rated torque from zero torque at rated speed was reduced by 67 % compared to PI-FOC and by 57 % compared to a deadbeat controller. Since the proposed reference pre-rotation (RPR) method assumes a circular shape of the flux linkage reference, its application is limited to the linear modulation range.

To take advantage of both the RPR and HRG methods, they are combined into a time-optimal harmonic reference generator (TO-HRG). Extensive experimental and simulative investigations as well as comparisons with state-of-the-art methods on an interior permanent magnet synchronous machine drive with significant (cross-)saturation effects empirically prove the TOC performance in the entire modulation range of the presented TO-HRG with the proposed state-constrained CCS-MPFC and PC scheme.

Zusammenfassung

Die Erhöhung der Leistungs- und Drehmomentdichte sowie der Dynamik von elektrischen Antrieben ist zentrales Ziel von Antriebsregelungen, um Gewicht und Bauraum einzusparen. Um das Potenzial elektrischer Antriebe im transienten und stationären Betrieb für gegebenen Maximalstrom und gegebene Zwischenkreisspannung voll auszuschöpfen, wird in dieser Arbeit eine modulatorbasierte modellprädiktive Flussregelung (CCS-MPFC für engl.: continuous control set model predictive flux control) für Synchronmaschinen (SM) vorgestellt. Diese Regelung ist in der Lage, Arbeitspunkte für gegebene Referenzdrehmomente in kürzest möglicher Zeit zu erreichen, wobei transiente Überströme sowie Drehmomentüber- und -unterschwinger verhindert werden. Darüber hinaus kann die gesamte Zwischenkreisspannung des Umrichters nahtlos von der linearen Modulation bis zur Übermodulation einschließlich Blocktaktung ausgenutzt werden.

Ein nahtloser Übergang in den Übermodulationsbereich wird durch einen harmonischen Referenzgenerator (HRG) und eine Pulsunterdrückung (PC für engl.: pulse clipping) ermöglicht. Der HRG berechnet und addiert die durch das Spannungshexagon des Umrichters induzierten Flussoberschwingungen im Übermodulationsbereich zur mittleren Flussreferenz der CCS-MPFC. Das spezifische Schaltverhalten und die vorgesehene Wahl der Elementarvektoren des Umrichters im Übermodulationsbereich, z. B. Blocktaktung, werden mit Hilfe des PC sichergestellt. Dies führt zu einer ca. 10 % höheren Leistung des Antriebs oberhalb der Nenndrehzahl im Vergleich zu Antriebsregelungen, die auf den linearen Modulationsbereich beschränkt sind, z. B. Proportional-Integral feldorientierte Regelung (PI-FOR). Obwohl HRG und PC stationär die Spannungsausnutzung maximieren, ergibt sich im transienten Betrieb eine zeitsuboptimale Regelung.

Mit Hilfe des Prinzips von Pontryagin wird das Optimierungsproblem zur zeitoptimalen Regelung von SMs ohne Berücksichtigung von Strom- und Drehmomentgrenzen in jedem Abtastschritt gelöst und über eine Vordrehung des Referenzflusses im statorfesten Koordinatensystem eingearbeitet. Um transiente Überströme und Drehmomentüber- und -unterschwinger zu verhindern, werden Strom- und Drehmomentgrenzen über Zustandsbeschränkungen innerhalb des Optimierungsproblems der CCS-MPFC berücksichtigt. Hier konnte die Zeit bis zum Erreichen des Nenndrehmoments ausgehend vom Nulldrehmoment bei Nenndrehzahl im Vergleich zur PI-FOR um 67 % und zu einem Dead-Beat-Regler um 57 % reduziert werden. Da die Referenzvordrehung (RPR für engl.: reference pre-rotation) eine kreisförmige Trajektorie der Flussreferenz annimmt, ist die Anwendung der RPR auf den linearen Modulationsbereich limitiert.

Um die Vorteile von RPR und HRG zu nutzen, werden diese zu einem zeitoptimalen harmonischen Referenzgenerator (TO-HRG für engl.: time-optimal harmonic reference generator) kombiniert. Umfangreiche experimentelle und simulative Untersuchungen an einer permanentmagneterregten Synchronmaschine mit vergrabenen Magneten sowie Vergleiche mit dem Stand der Technik entsprechenden Verfahren bestätigen empirisch zeitoptimales Regelverhalten über den gesamten Modulationsbereich der vorgestellten Methodik bestehend aus TO-HRG, zustandsbeschränkter CCS-MPFC und PC.

Own Publications

Relevant own Work for the Thesis

- A. Brosch, O. Wallscheid, and J. Böcker. "Model predictive control of permanent magnet synchronous motors in the overmodulation region including six-step operation," *IEEE Open Journal of Industry Applications*, vol. 2, pp. 47–63, 2021. DOI: 10.1109/OJIA.2021.3066105.

- A. Brosch, O. Wallscheid, and J. Böcker, "Model predictive torque control for permanent-magnet synchronous motors using a stator-fixed harmonic flux reference generator in the entire modulation range," *IEEE Transactions on Power Electronics*, vol. 38, no. 4, pp. 4391–4404, 2023. DOI: 10.1109/TPEL.2022.3229619.

- A. Brosch, O. Wallscheid, and J. Böcker. "Time-optimal model predictive control of permanent magnet synchronous motors considering current and torque constraints," *IEEE Transactions on Power Electronics*, vol. 38, no. 7, pp. 7945–7957, 2023. DOI: 10.1109/TPEL.2023.3265705.

- A. Brosch, O. Wallscheid, and J. Böcker. "Time-optimal model predictive control of permanent magnet synchronous motors in the whole speed and modulation range considering current and torque limits," *Preprint submitted to IEEE Open Journal of the Industrial Electronics Society*, vol. 4, pp. 643–658, 2023. DOI: 10.1109/OJIES.2023.3335069.

Further own Work

As Main Author

- A. Brosch, S. Hanke, O. Wallscheid, and J. Böcker. "Data-driven recursive least squares estimation for model predictive current control of permanent magnet synchronous motors," *IEEE Transactions on Power Electronics*, vol. 36, no. 2, pp. 2179–2190, 2021. DOI: 10.1109/TPEL.2020.3006779.

- A. Brosch, O. Wallscheid, and J. Böcker. "Torque and inductance estimation for finite model predictive control of highly utilized permanent magnet synchronous motors," *IEEE Transactions on Industrial Informatics*, vol. 17, no. 12, pp. 8080–8091, 2021. DOI: 10.1109/TII.2021.3060469.

- A. Brosch, J. Rauhaus, O. Wallscheid, D. Zimmer, and J. Böcker. "Data-driven adaptive torque oscillation compensation for multi-motor drive systems," *IEEE Open Journal of Industry Applications*, vol. 3, pp. 66–78, 2022. DOI: 10.1109/OJIA.2022.3171333.

- A. Brosch, O. Wallscheid, and J. Böcker. "Long-term memory recursive least squares online identification of highly utilized permanent magnet synchronous motors for finite-control-set model predictive control," *IEEE Transactions on Power Electronics*, vol. 38, no. 2, pp. 1451–1467, 2023. DOI: 10.1109/TPEL.2022.3206598.
- A. Brosch, F. Tinazzi, O. Wallscheid, M. Zigliotto, and J. Böcker. "Finite set sensorless control with minimum a priori knowledge and tuning effort for interior permanent magnet synchronous motors," *IEEE Transactions on Power Electronics*, vol. 38, no. 10, pp. 12508–12519, 2023. DOI: 10.1109/TPEL.2023.3294557.

As Co-Author

- G. Book, A. Traue, P. Balakrishna, A. Brosch, M. Schenke, S. Hanke, W. Kirchgässner, and O. Wallscheid. "Transferring online reinforcement learning for electric motor control from simulation to real-world experiments," *IEEE Open Journal of Power Electronics*, vol. 2, pp. 187–201, 2021. DOI: 10.1109/OJPEL.2021.3065877.
- I. D. De Martin, A. Brosch, F. Tinazzi, and M. Zigliotto. "Continuous control set model predictive torque control with minimum current magnitude criterion for synchronous electric motor drive," *IEEE Transactions on Industrial Electronics*, vol. 71, no. 7, pp. 6787–6796, 2023. DOI: 10.1109/TIE.2023.3308132.
- L. Hölsch, A. Brosch, R. Steckel, T. Braun, S. Wendel, J. Böcker, and O. Wallscheid. "Insights and challenges of co-simulation-based optimal pulse pattern evaluation for electric drives," *IEEE Transactions on Energy Conversion*, 2024. DOI: 10.1109/TEC.2024.3374962.

Nomenclature

Abbrevations

BVP	boundary value problem
CCS	continuous control set
CCS-MPCC	continuous control set model predictive current control
CCS-MPFC	continuous control set model predictive flux control
DB-DTFC	deadbeat direct torque and flux control
DBFC	deadbeat flux control
DSC	direct self control
DTC	direct torque control
FCS	finite control set
FMC	flux map correction
GFO	Gopinath-style flux observer
HRG	harmonic reference generator
IGBT	insulated-gate bipolar transistor
IM	induction machine
IPMSM	interior permanent magnet synchronous machine
IVP	initial value problem
LUT	look-up table
MPC	model predictive control
MTPC	maximum torque per current
MTPV	maximum torque per voltage
ODE	ordinary differential equation
OPC	operating point controller
PC	pulse clipping
PI	proportional-integral

PI-FOC	proportional-integral field-oriented control
PMSM	permanent magnet synchronous machine
QP	quadratic program
RPR	reference pre-rotation
RRCC	rotating reference chase control
SM	synchronous machine
SPMSM	surface permanent magnet synchronous machine
SVM	space vector modulation
SynRM	synchronous reluctance machine
TO-HRG	time-optimal harmonic reference generator
TO-MPC	time-optimal model predictive control
TOC	time-optimal control(ler)
VAC	voltage angle control
VSI	voltage source inverter

Symbols

$\delta\boldsymbol{\psi}$	flux linkage correction of the FMC
ε	electrical angle
ε_0	initial electrical rotor angle
$\varepsilon_{\mathrm{rpr}}$	pre-rotation angle of the RPR
ϑ	terminal costs
λ	Laplace variable
$\boldsymbol{\lambda}$	costate variable
τ	time constant
Φ	running costs
$\psi, \boldsymbol{\psi}$	flux linkage
$\overline{\psi^*}, \overline{\boldsymbol{\psi}^*}$	flux linkage reference without harmonic content in the overmodulation range
$\tilde{\psi}^*, \tilde{\boldsymbol{\psi}}^*$	harmonic content of the flux linkage reference in the overmodulation range
ψ_{p}	permanent magnet flux linkage
$\hat{\psi}_{\mathrm{cm}}, \hat{\boldsymbol{\psi}}_{\mathrm{cm}}$	flux linkage estimate of a current model
$\hat{\psi}_{\mathrm{vm}}, \hat{\boldsymbol{\psi}}_{\mathrm{vm}}$	flux linkage estimate of a voltage model
ω	electrical speed

ω_0	characteristic frequency of the GFO
ω_{fmc}	speed threshold of the FMC
$\boldsymbol{A}_x, \boldsymbol{B}_x, \boldsymbol{E}_x$	system matrices of the state-space representation of the linear parameter-varying prediction models for flux linkage, current, and torque with $x \in \{\psi, i, T\}$
$\boldsymbol{\mathcal{A}}_x$	matrix of linear current, voltage, and torque inequality constraints formulation with $x \in \{\mathcal{I}, \mathcal{U}, \mathcal{T}\}$
$\boldsymbol{\mathcal{A}}_x^{'}, \boldsymbol{b}_x^{'}$	linear inequality quantities for torque and current mapped to the input space with $x \in \{\mathcal{I}, \mathcal{T}\}$
$\boldsymbol{b}_x$	vector of linear current, voltage, and torque inequality constraints formulation with $x \in \{\mathcal{I}, \mathcal{U}, \mathcal{T}\}$
C	integration constant
D	damping ratio of the GFO
$e, \boldsymbol{e}$	error of current trajectories computed with the HRG in the overmodulation range
$\boldsymbol{f}_{\mathrm{c}}$	function that maps state and input of a continuous-time nonlinear system to the rate of change of the state
$\boldsymbol{f}_{\mathrm{d}}$	function that maps state and input of a discrete-time nonlinear system to the successor state
$\boldsymbol{g}$	terminal condition
G_{cm}	voltage model transfer function
G_{vm}	current model transfer function
$\boldsymbol{h}$	path constraints
H	Hamiltonian
$\boldsymbol{H}_x, \boldsymbol{h}_x, \eta_x$	quatric quantities characterizing the loci of a SM to calculate a loss-optimal operating point with $x \in \{\boldsymbol{I}_{\mathrm{max}},$ Iso-Torque, Iso-Voltage, MTPC, MTPV$\}$
$i, \boldsymbol{i}$	current
$i_{\mathrm{d,max}}$	maximum permissible d-current during transient operation
$i_{\mathrm{lin}}, \boldsymbol{i}_{\mathrm{lin}}$	current at which the nonlinear magnetization of an SM is linearized
$\boldsymbol{I}_2$	2×2 identity matrix
I_{max}	maximum permissible current during stationary operation
$I_{\mathrm{max,dyn}}$	maximum permissible current during transient operation
$\boldsymbol{J}$	cost function(al)
k	discrete time step
K_{p}	proportional gain of a PI controller or PI element
ℓ	stage costs

$\boldsymbol{L}_\Delta$	differential inductance matrix of a nonlinearly magnetized SM
L_{xy}	entries of the differential inductance matrix $\boldsymbol{L}_\Delta$ of a nonlinearly magnetized SM with $x \in \{\mathrm{d}, \mathrm{q}\}$ and $y \in \{\mathrm{d}, \mathrm{q}\}$
L_x	inductances of a linearly magnetized SM with $x \in \{\mathrm{d}, \mathrm{q}\}$
m	modulation index
$m_{\max}$	maximal modulation index
N_{bvp}	number of supporting points
n_{me}	mechanical speed
N_{opc}	number of iterations of the OPC
N_{mpc}	prediction horizon
N	number of iterations of the RPR
p	pole pair number
P	mechanical power
R_{s}	stator resistance
$s, \boldsymbol{s}$	switching states of the half bridges of a three-phase two-level VSI
$\boldsymbol{s}_{\mathrm{ccs}}$	switching commands calculated by a SVM before PC occurs in the overmodulation range
s_n	switching state of a three-phase two-level VSI numbered from 1 to 8
t	time
T	torque
$t_{1,\ldots,8}$	pulse durations of the elementary vectors calculated by the SVM
T_{c}	pulse clipping time of the PC strategy
T_{i}	inverter interlocking time
T_{r}	reset time of a PI controller or PI element
t_{rpr}	time duration estimate of the RPR to reach the reference
T_{s}	sampling time
t_{thresh}	RPR time threshold to distinguish between steady-state and transient operation
$u, \boldsymbol{u}$	voltage
$\boldsymbol{u}_{1,\ldots,8}$	elementary voltages of a three-phase two-level VSI
$\boldsymbol{u}_{\mathrm{ccs}}$	voltage command of the CCS-MPFC for schemes with PC
u_{DC}	DC-link voltage
$u_{\mathrm{f}}, \boldsymbol{u}_{\mathrm{f}}$	fundamental voltage

$u_{\max}$	maximum voltage of a circular approximation of the voltage hexagon
$\boldsymbol{u}_{\text{unc}}$	unconstrained solution voltage
$\boldsymbol{x}$	state variable

General Notations

x, X	scalar
$\boldsymbol{x}$	column vector
$\boldsymbol{x}^\intercal$	transpose of $\boldsymbol{x}$
$\boldsymbol{X}$	matrix
$\boldsymbol{X}^{-1}$	inverse of $\boldsymbol{X}$
$\hat{x}$	estimate of x
x^*	reference of x
$\overline{x(t)}$	(arithmetic) mean of $x(t)$
$\angle\boldsymbol{x}$	angle of $\boldsymbol{x}$ in the stator-fixed $\alpha\beta$ or rotor-fixed dq coordinate system
$\boldsymbol{x}_{\text{abc}}$	representation of $\boldsymbol{x}$ in the three-phase abc coordinate system (stator-fixed)
$\boldsymbol{x}_{\alpha\beta}$	representation of $\boldsymbol{x}$ in the $\alpha\beta$ coordinate system (stator-fixed)
$\boldsymbol{x}_{\text{dq}}$	representation of $\boldsymbol{x}$ in the dq coordinate system (rotor-fixed)
$\boldsymbol{T}_{rs}$	transformation matrix to transform $\boldsymbol{x}$ from coordinate system $s \in \{\text{abc}, \alpha\beta, \text{dq}\}$ to coordinate system $r \in \{\text{abc}, \alpha\beta, \text{dq}\}$
$\|\boldsymbol{x}\|$	2-norm or length of $\boldsymbol{x}$ (Euclidean norm).
$\frac{\mathrm{d}x}{\mathrm{d}t}$	time derivative of x
$\frac{\partial x}{\partial y}$	partial derivative of x with respect to y
$x \in \mathcal{Y}$	x belongs to set $\mathcal{Y}$

Contents

1 Introduction

Electric drives are an essential part of the modern industrial society. They are utilized to perform process engineering tasks in automated production lines, power plants, centrifuges, elevators, vehicles, etc. and are responsible for about 70 % of the electrical energy conversion in the European Union [1]. In many cases, the drives are subject to dynamic load profiles. Prominent examples are electric drives in vehicles, aircrafts and ships, or generators in renewable energy applications such as wind turbines. The power of these drives lies within the range of a few kW up to the MW class. Typically, these drives are realized as three-phase alternating current (AC) systems, consisting of a machine, a power electronic converter, and a control unit for closed-loop operation. Therefore, the requirements concerning control accuracy during steady-state operation and control dynamics during transient operation of torque, speed, or position of the drive are usually specified by the task and/or customer. As a result, contemporary control algorithms must be designed with attention to a wide range of application-specific demands.

1.1 Motivation

In order to maintain economic and ecological interests throughout the life cycle of an electric drive, the consumption of resources must be minimized under the condition that the drive task can still be fulfilled. Here, resources are needed in the following areas:

- The **development** of drives by experts ties up a considerable amount of human resources. This is due to the increasing complexity and variety of electric drives and their requirements in various engineering fields, such as thermodynamics, electrical engineering, mechanical engineering, and control engineering.

- Resources must also be conserved during the **production** of electric drives. High quality materials are used in the manufacturing process: typically large quantities of copper, electrical steel and, if necessary, permanent magnets, often based on rare earth materials. In addition, further resources are required for the inverter, e.g., semiconductor components.

- Another resource is the transferred energy during **operation**. Most of this energy is necessary to perform the drive task, such as the thrust of an electrically driven propeller of an airplane. However, a non-negligible part of the supplied energy is dissipated within the electrical drive (machine and inverter). In addition to the design of the machine and inverter, the applied controller has a significant influence on the power losses and drive efficiency.

A key factor in the resource consumption of electric drives during the product life cycle is the degree of utilization of the drive. Often, machines and inverters are over-dimensioned and only slightly utilized, because the control and also the strategies to protect the drive from thermal destruction are widely simplified. Thus, not only the design of the machine and the inverter, but also the employed torque control algorithm has significant impact on the utilization and resource consumption of the drive which is explained in the following.

Reduced electromagnetic utilization of the machine results in lower torque density. To still meet the torque requirements, a larger and heavier machine must be employed. This increases the installation space and the weight of the drive and, therefore, increases the resource consumption during the production process. In addition, if the drive system is used in a mobile application, such as electric locomotion, the additional weight of the drive due to the necessary over-dimensioning will cause further system losses during operation. In order to realize this savings potential by increasing the degree of utilization, the magnetic (cross-)saturation effects that occur must be taken into account by the employed drive controller.

In contrast to the maximum torque, the maximum power of the drive also depends on the maximum fundamental voltage that can be provided by the inverter. For this reason, it is crucial to utilize the given inverter's DC-link voltage to its maximum extent by increasing the range of the modulation index[1] towards overmodulation and six-step operation[2]. Fig. 1.1 shows exemplary achievable torque and power curves of a highly utilized permanent magnet synchronous machine (PMSM) with significant (cross-)saturation effects for linear modulation and overmodulation up to six-step operation. Since the fundamental of the voltage can be increased by approx. 10 % by exploiting the overmodulation range with the help of a suitable control scheme, the torque and power of the drive are increased by approx. 10 % during high-speed operation, where the maximum torque is limited by the applicable fundamental voltage. Only this way the power density of the drive system can be maximized without changing the hardware setup [2–4]. Therefore, a drive control scheme must be applied that fully utilizes the available DC-link voltage to increase the utilization of the electric drive.

Another important aspect of drive control schemes, besides the ability to handle highly utilized machines and the maximum voltage utilization of the drive during steady-state operation, is the control performance during transient operation. Here, the torque control dynamics directly affect the jerk and acceleration of the drive. Therefore, the torque response is another important performance criterion, whereby highest torque control dynamics without overcurrents and without torque overshoot or undershoot are desired.

Although increasing the degree of utilization of the drive during steady-state and transient operation offers the potential to save resources in the production and operation of the drive, it can be expected that the complexity of the control scheme will also increase. This increases the effort required to develop and commission the drive control algorithm, which ties up additional human resources. To minimize this application effort, control schemes that cover the entire operating range without switching between different control strategies, e.g., specifically tailored

[1]The modulation index m corresponds to the fundamental of the applied voltage, normalized to the maximum possible magnitude of the fundamental reached during six-step operation, cf. (2.16).

[2]In six-step mode, there is no modulation of the inverter, and the elementary voltage vectors (corners of the voltage hexagon) are switched counterclockwise every sixth of the fundamental time period for positive machine speeds and clockwise for negative speeds, resulting in the maximum possible magnitude of the fundamental voltage, cf. Sec. 2.4 and Fig. 2.2.

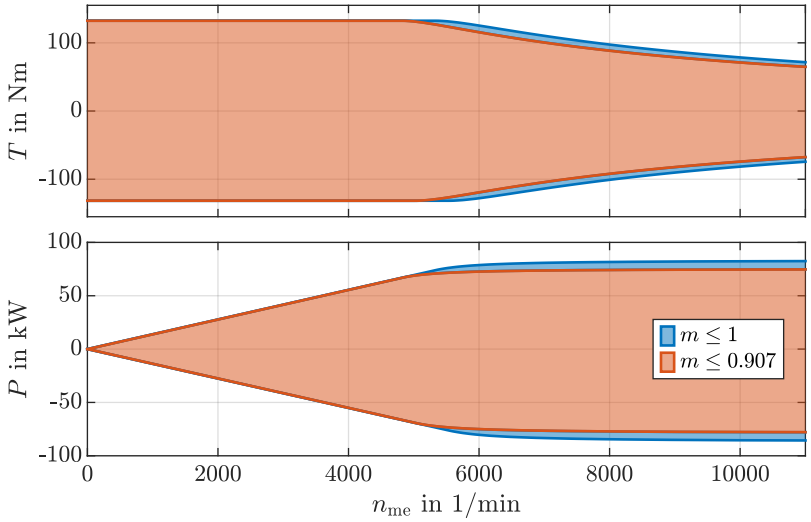

Fig. 1.1: Speed-dependent achievable torque and power of a highly utilized IPMSM (cf. App. A.2) for linear modulation ($m \leq 0.907$) and overmodulation up to six-step operation ($m \leq 1$)

schemes for low-speed and high-speed operation or transient and steady-state operation, are preferred. In addition, generalizable drive controllers with few tuning parameters that can be applied to different machine types, e.g., surface permanent magnet synchronous machine (SPMSM), interior permanent magnet synchronous machine (IPMSM), or synchronous reluctance machine (SynRM) , allow rapid implementation for series and sample-specific applications with minimal expert intervention.[3] Thus, the requirements for a torque control scheme to increase drive utilization and reduce resource consumption during development, production, and operation can be summarized as follows:

- Highest control accuracy of loss-optimal operating points during stationary operation.
- Capability to handle nonlinearly magnetized machines.
- Maximum utilization of the DC-link voltage of the inverter during stationary operation.
- Highest torque control dynamics without overcurrents and without torque overshoots or undershoots during transient operation.
- Applicability to different machine types with few tuning parameters in the whole operating range.

1.2 State-of-the-Art Methods

The following section is based on literature reviews of the own publications [5–8]. The author of this thesis contributed the main parts of [5–8]. He also prepared the publications independently, while the contributions of the other co-authors were limited to technical discussions during the investigation phase as well as proofreading of the manuscript. Therefore, parts of the following

[3]Since the control scheme proposed in this work is not directly applicable to the externally excited synchronous machine (EESM), this type of synchronous machine is not considered in the thesis.

text have been taken in modified or unmodified form from the mentioned publications. For the sake of readability, the underlying self-citations are not explicitly listed in the following.

For controlled electric drives, a certain torque (force for linear drives), speed or position of the drive is requested. In order to reach the specified reference, i.e., torque, speed or position, a cascaded control structure is usually implemented, with torque control as the innermost cascade [9, 10]. Here, the torque controller represents the interface between the electrical quantities (electromagnetic torque, current, flux linkage) and the mechanical quantities (mechanical torque, velocity, position) of the outer velocity and the position control cascades. Since the torque control directly affects the outer cascades, the performance of the torque control is of central importance.

The reference torque for synchronous machines (SM) can be achieved by various operating points, whereby each is specified by a combination of stator currents in steady-state operation. The operating point with the lowest losses is preferred. This loss-optimal operating point is calculated by an open-loop torque controller, also known as an operating point controller (OPC) [11]. The OPC utilizes a steady-state machine model and feeds the operating point to an underlying closed-loop controller. As control variables for the underlying controller, currents or flux linkages in the stator-fixed or rotor-fixed coordinate system can be considered. Alternatively, the tuple consisting of torque and flux linkage amplitude can be used equivalently [12, 13].

The proportional-integral field-oriented control (PI-FOC) [14] in its standard formulation still represents the most popular underlying closed-loop controller, despite the availability of various innovative control approaches. The main reason for this is probably its simple structure, which allows easy implementation on microprocessors. However, the PI-FOC does not allow overmodulation or optimal control dynamics. Numerous methods exist to improve the transient performance of SM drives compared to PI-FOC and/or to enable operation in the entire overmodulation range up to six-step operation. These methods are described in the following and are classified into torque control schemes that improve the utilization of the drive during transient operation (i.e., increase the control dynamics) and during steady-state operation (i.e., allow operation in the overmodulation range). The properties of those methods, which are most relevant for this work with respect to the utilization of the drive during transient and steady-state operation, are listed in Tab. 1.1.

1.2.1 Methods Improving Control Dynamics

Time-optimal controllers (TOC) [15–20] maximize control dynamics by reaching the operating point in the shortest possible time. To achieve this, the future transient state and input trajectories must be optimized. Consequently, all controller types that do not optimize the entire transient achieve time-suboptimal control performance, such as PI-FOC [21], deadbeat direct torque and flux control (DB-DTFC) [12, 13], and direct torque control (DTC) [22]. Especially for large reference torque variations, it may take several sampling periods to reach a new operating point. Similarly, model predictive controllers (MPC) [23–26] may only achieve time-suboptimal control performance during transients because their prediction horizon is always limited by the computational capacity of the embedded controller.

To maximize control dynamics, control methods must be applied that solve the TOC problem at each controller sampling instant [15–20]. Using optimal control theory methods, such as

Pontryagin's principle[4], the TOC solution for input and state trajectories during transients for SMs can be derived to reach the operating point in the shortest possible time. From previous publications in this field, two characteristics can be observed for the TOC solution of the stator voltages (input trajectories) during transients [15, 17]:

1. The stator voltages are constant in the stator-fixed coordinate system.
2. The stator voltages are saturated by the input constraint (voltage hexagon or a circular approximation of the voltage hexagon).

Constant voltages result in a linearly shaped trajectory of the SM's flux linkage in the stator-fixed frame by neglecting the ohmic voltage drop, since the ordinary differential equation (ODE) of the flux linkage (Faraday's law of induction) is equal to an integrator. In addition, the voltages saturated by the input constraints ensure the fastest possible movement of the flux linkages in the stator-fixed reference frame. To compute the time-optimal stator voltage during transients, a nonlinear system of equations must be solved iteratively in an online fashion. The publications [15–18, 20] solve the TOC problem at each sampling instant. Here, the bisection method can be applied as a numerical solver with a constant number of iterations per sampling instant [15]. For the rotating reference chase control (RRCC) method proposed in [19], one iteration to solve the TOC problem per sampling instant is performed based on the TOC solution of the previous sampling instant. Compared to the methods [15–18, 20], only the RRCC considers transient overcurrents as well as torque overshoots and undershoots and tries to prevent them heuristically. Nevertheless, these transient overcurrents as well as torque overshoots and undershoots can be reduced compared to the TOC methods [15–17, 20], but not prevented with the RRCC, as shown in Sec. 5.5.4.

1.2.2 Methods Improving Stationary Voltage Utilization

Current harmonics inevitably occur in the overmodulation range induced by the voltage constraints of the feeding inverter (hexagon). The harmonics and the voltage constraint itself are limiting control strategies, e.g., the PI-FOC [27–31], to the linear modulation range. However, there are control approaches that can exploit the overmodulation range.

In the context of PI-FOC, enhancements can be applied to reduce the degradation caused by current harmonics to enable the use of the overmodulation range [5, 32–36]. In [36], low-pass filters are used in the feedback path to suppress current harmonics. Obviously, adding low-pass filters to the control loop reduces its dynamic performance. Methods [5, 32–35] use model-based approaches to estimate the current harmonics and compensate for them in the control loop [5, 32–35]. In [32], the harmonics in the overmodulation range are estimated in an open-loop fashion using a harmonic machine model. Here, the estimator provides accurate observations during steady state conditions, but stability problems may occur during transient operation due to a difference of the system eigenvalues [34]. To overcome this problem, a feedback path was added to the estimator in [33–35]. However, six-step operation cannot be realized. In contrast, six-step operation combined with PI-FOC can be achieved in [5, 37]. In [37], a higher-level open-loop torque controller allows the rotation of the reference voltage vector for the modulator outside the voltage hexagon. Using Bolognani's overmodulation scheme [38], six-step operation is ensured because the reference voltage vector for the modulator rotates so far outside the voltage hexagon that the voltage corrections of the proportional-integral (PI) current controllers, which

[4] also known as Pontryagin's maximum or minimum principle

are induced by the current harmonics in the overmodulation range, do not affect the modulator. However, in between the linear modulation range and six-step operation, the PI controllers' actuating voltage vector intersects the voltage hexagon. The resulting excitation of the PI-FOC by the current harmonics therefore leads to deterioration and suboptimal control performance in this modulation range. In [5], a harmonic reference generator (HRG) is proposed that calculates the harmonic components of the current in the overmodulation range and adds them to the reference current by solving a computationally comprehensive boundary value problem (BVP) using Holtz's overmodulation scheme [39]. This provides high control performance in transient and steady-state operation in the entire overmodulation range. Compared to the PI-FOC, the dynamic control performance can be further increased by combining the HRG with a continuous control set model predictive current controller (CCS-MPCC) [5].

MPCs are characterized by increased control dynamics and can inherently handle input constraints [40]. Therefore, MPC is well suited for the control of electric drives, especially in the overmodulation range at the voltage limit [2, 5, 41–49]. MPC methods can be classified into continuous control set (CCS) algorithms combined with a modulator [5, 41, 46, 47] and finite control set (FCS) methods that directly determine the switching pulses for the inverter [2, 42–45, 48, 49]. Although the CCS-MPCC methods [41, 46, 47] and the FCS-MPCC methods [42, 43, 45, 48] increase the modulation index beyond the linear modulation range, they do not inherently achieve six-step operation. Nevertheless, the CCS-MPCC method [5] mentioned in the previous paragraph and the FCS-MPCC methods [2, 44, 49] are able to realize six-step operation. By sufficiently penalizing the inverter switching in the FCS-MPCC cost function, six-step operation can be enforced [44]. The method [2], on the other hand, ensures six-step operation by means of a rectangular control error boundary. Using a pulse clipping (PC) scheme, current control in the overmodulation range is enabled up to the six-step operation in [49].

A deadbeat flux control (DBFC) strategy is proposed in [50] that continuously transitions from the linear to the overmodulation region, including six-step operation. This is achieved by synthesizing a flux reference trajectory in the stator-fixed coordinate system that is circular in the linear modulation region, hexagonal during six-step operation, and a combination of both in the overmodulation region. The authors of [50] have extended the DBFC to achieve TOC in [16]. To the best of the author's knowledge, this is the only TOC method that can cover the entire overmodulation range. However, the DBFC [16] does not take current and torque limits into account, resulting in significant undesirable overcurrents as well as torque overshoots and undershoots.

In six-step operation, the DC-link voltage of the inverter is fully utilized and, therefore, the fundamental voltage is maximized. In addition, the switching frequency and switching losses of the inverter are minimized. For these reasons, extensive research has been conducted on six-step operation [4, 32, 37–39, 51–56]. The contributions [38, 39, 53, 54, 56, 57] propose schemes that synthesize voltage vector trajectories in the overmodulation range up to six-step operation under the assumption of steady-state operation without considering closed-loop control dynamics. Direct self controllers (DSC) [52, 58, 59] or voltage angle controllers (VAC) [4, 51, 55] are usually applied only in the constant-power region. Below the rated speed (in the constant-torque region), it is necessary to switch to another controller designed for the constant-torque region, such as PI-FOC. This switchover can cause transition issues, which are undesirable for highly dynamic applications such as servo or automotive traction drives.

Tab. 1.1: Properties of the most relevant state-of-the-art methods and the control scheme presented in this thesis

Method	Transient operation		Stationary operation		
	Current and torque limits	Time-optimal control	Linear modulation	Over-modulation	Six-step operation
PI-FOC [14, 27–31]			✓		
PI-FOC [33–36]			✓	✓	
PI-FOC [37]			✓		✓
PI-FOC [5, 32]			✓	✓	✓
DB-DTFC [12, 13]			✓		
DSC [52, 58, 59]					✓
VAC [4, 51, 55]					✓
CCS-MPCC [41, 46, 47]			✓	✓	✓
CCS-MPCC [5]			✓	✓	
FCS-MPCC [42, 43, 45, 48]			✓	✓	
FCS-MPCC [2, 44, 49]			✓	✓	✓
TOC [15, 17, 18, 20]		✓	✓		
RRCC [19]	✓	✓	✓		
DBFC [50]			✓	✓	✓
DBFC [16]		✓	✓	✓	✓
Presented control scheme	✓	✓	✓	✓	✓

1.3 Goal and Structure of the Thesis

The goal of this work is to develop and investigate a torque control method for three-phase SMs[5] that fulfills the requirements mentioned in Sec. 1.1 with special emphasis on maximizing the utilization of the electrical drive during transient and stationary operation, i.e., time-optimal control performance without torque overshoots and undershoots and without overcurrents in the entire modulation range up to six-step operation, cf. Tab. 1.1.

A state-of-the-art continuous control set model predictive flux controller (CCS-MPFC) combined with a well-established open-loop torque controller (operating point controller) [11] serves as the baseline for the control scheme extensions, which are the contributions of this thesis. These extensions can be split into three chapters: in Ch. 4, an HRG is presented that adds a harmonic component to the flux linkage reference of the CCS-MPFC to allow operation in the entire modulation range. Using a flux linkage reference pre-rotation (RPR) and incorporating state constraints within the CCS-MPFC, TOC performance can be achieved within the linear modulation range while respecting current and torque limits, cf. Ch. 5. Finally, the RPR and CCS-MPFC with state constraints presented in Ch. 5 are fused with the HRG in Ch. 6 to achieve TOC performance while respecting torque and current limits within the entire modulation range. A graphical representation of the structure of the thesis is shown in Fig. 1.2.

[5] SPMSM, IPMSM and SynRM

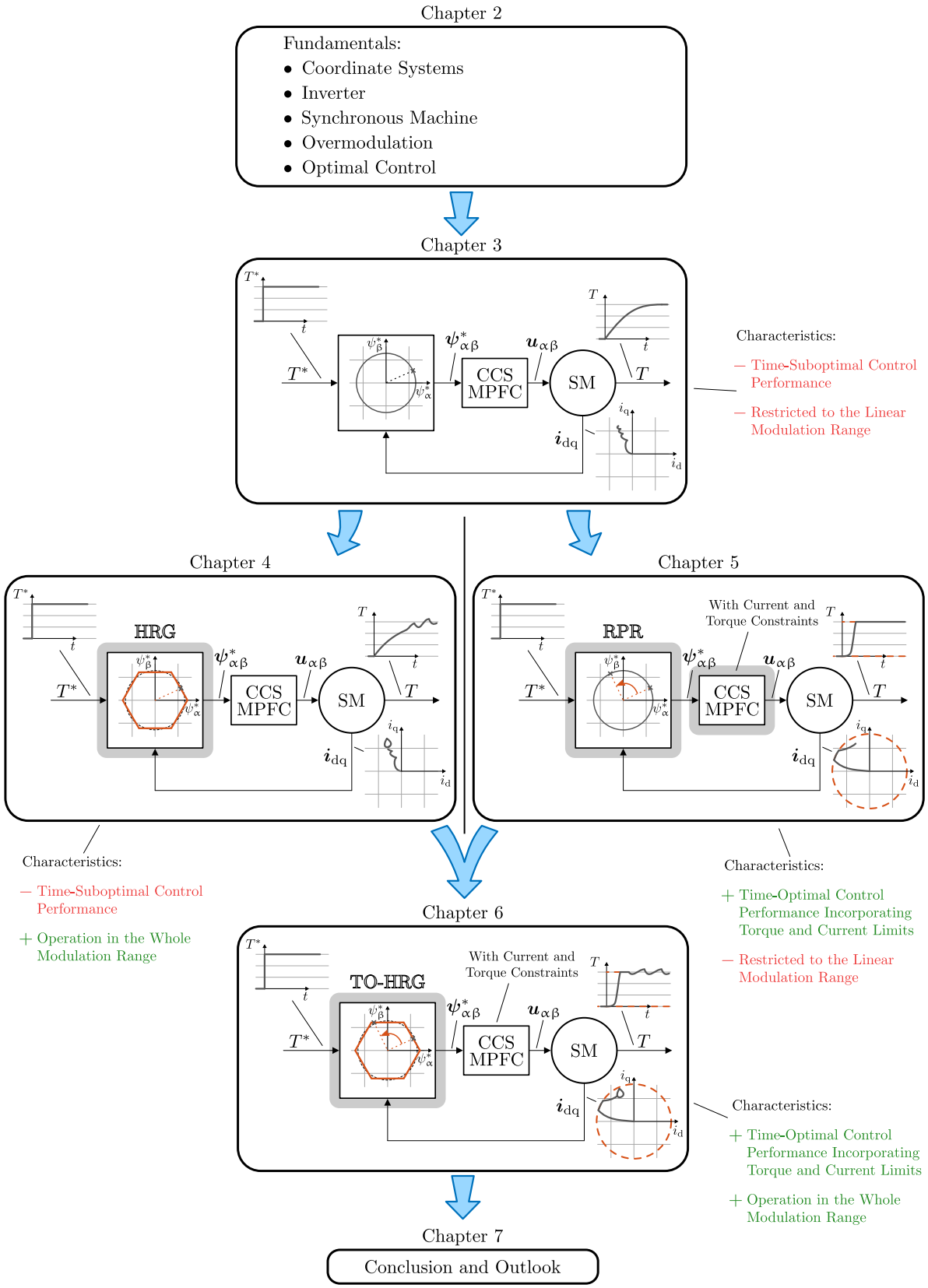

Fig. 1.2: Structure of the thesis with simplified control scheme diagrams (gray shaded parts are focused in the corresponding chapters)

2 Fundamentals

This chapter briefly summarizes the basic concepts required to follow the subsequent chapters. Readers who are already familiar with controlled three-phase drives can skip this chapter.

2.1 Coordinate Systems

A physical vector quantity $\boldsymbol{x}$, e.g., voltages $\boldsymbol{u}$, currents $\boldsymbol{i}$, and flux linkages $\boldsymbol{\psi}$, can be represented in the stator-fixed three-phase abc, in the stator-fixed $\alpha\beta$, or in the rotor-fixed dq coordinate system. Assuming a vanishing zero-sequence component ($x_\mathrm{a} + x_\mathrm{b} + x_\mathrm{c} = 0$), the required transformations can be formulated as

$$\underbrace{\begin{bmatrix} x_\mathrm{d}(t) \\ x_\mathrm{q}(t) \end{bmatrix}}_{\boldsymbol{x}_\mathrm{dq}(t)} = \underbrace{\begin{bmatrix} \cos(\varepsilon(t)) & \sin(\varepsilon(t)) \\ -\sin(\varepsilon(t)) & \cos(\varepsilon(t)) \end{bmatrix}}_{\boldsymbol{T}_\mathrm{dq\alpha\beta}(\varepsilon(t))=\boldsymbol{T}^{-1}_{\alpha\beta\mathrm{dq}}(\varepsilon(t))} \underbrace{\overbrace{\frac{2}{3}\begin{bmatrix} 1 & -\frac{1}{2} & -\frac{1}{2} \\ 0 & \frac{\sqrt{3}}{2} & -\frac{\sqrt{3}}{2} \end{bmatrix}}^{\boldsymbol{T}_{\alpha\beta\mathrm{abc}}} \overbrace{\begin{bmatrix} x_\mathrm{a}(t) \\ x_\mathrm{b}(t) \\ x_\mathrm{c}(t) \end{bmatrix}}^{\boldsymbol{x}_\mathrm{abc}(t)}}_{\boldsymbol{x}_{\alpha\beta}(t)=\begin{bmatrix} x_\alpha(t) & x_\beta(t) \end{bmatrix}^\mathsf{T}}, \tag{2.1}$$

where t denotes the continuous time, ε the electrical rotor angle of the SM and bold symbols represent matrices/vectors.

2.2 Inverter

To control three-phase AC machines, the state of the art is to apply an inverter fed by a DC voltage source. In this work, the commonly adopted three-phase two-level voltage source inverter (VSI) is considered to control a star-connected three-phase SM. The operating principle of this inverter is illustrated with ideal switches in Fig. 2.1. The star point of the SM is chosen as the reference potential for the inverter voltages such that $\boldsymbol{u}_\mathrm{abc}$ corresponds to the SM phase and inverter voltages. Assuming that the SM is a symmetrical load, the voltages $\boldsymbol{u}_\mathrm{abc}$ can be expressed as a function of the switching functions $s_\mathrm{a}(t), s_\mathrm{b}(t), s_\mathrm{c}(t)$:

$$\underbrace{\begin{bmatrix} u_\mathrm{a}(t) \\ u_\mathrm{b}(t) \\ u_\mathrm{c}(t) \end{bmatrix}}_{\boldsymbol{u}_\mathrm{abc}(t)} = u_\mathrm{DC}(t) \begin{bmatrix} \frac{2}{3} & -\frac{1}{3} & -\frac{1}{3} \\ -\frac{1}{3} & \frac{2}{3} & -\frac{1}{3} \\ -\frac{1}{3} & -\frac{1}{3} & \frac{2}{3} \end{bmatrix} \underbrace{\begin{bmatrix} s_\mathrm{a}(t) \\ s_\mathrm{b}(t) \\ s_\mathrm{c}(t) \end{bmatrix}}_{\boldsymbol{s}_\mathrm{abc}(t)}. \tag{2.2}$$

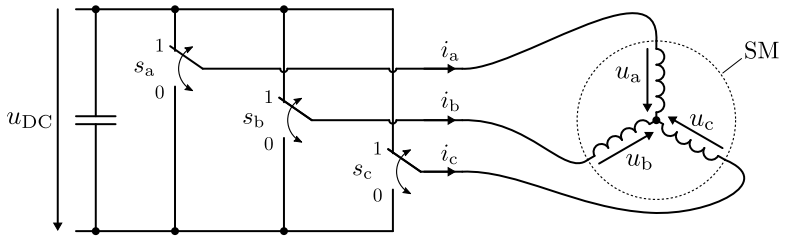

Fig. 2.1: Idealized two-level VSI controlling the voltages $\boldsymbol{u}_{\mathrm{abc}}$ of a three-phase SM

Tab. 2.1: Voltage values $\boldsymbol{u}_{\alpha\beta}$ of elementary vectors s_n for given switch positions $\boldsymbol{s}_{\mathrm{abc}}$ of the inverter

s_n	s_{a}	s_{b}	s_{c}	u_α	u_β
1	0	0	0	0	0
2	1	0	0	$+\frac{2}{3}u_{\mathrm{DC}}$	0
3	1	1	0	$+\frac{1}{3}u_{\mathrm{DC}}$	$+\frac{1}{\sqrt{3}}u_{\mathrm{DC}}$
4	0	1	0	$-\frac{1}{3}u_{\mathrm{DC}}$	$+\frac{1}{\sqrt{3}}u_{\mathrm{DC}}$
5	0	1	1	$-\frac{2}{3}u_{\mathrm{DC}}$	0
6	0	0	1	$-\frac{1}{3}u_{\mathrm{DC}}$	$-\frac{1}{\sqrt{3}}u_{\mathrm{DC}}$
7	1	0	1	$+\frac{1}{3}u_{\mathrm{DC}}$	$-\frac{1}{\sqrt{3}}u_{\mathrm{DC}}$
8	1	1	1	0	0

Here, $s_{\mathrm{a,b,c}} = 1$ connects the given phase to the upper potential of the DC-link, while $s_{\mathrm{a,b,c}} = 0$ connects it to the lower potential. With the help of the coordinate transformation (2.1), the stator voltages of the SM in the stator-fixed $\alpha\beta$ frame evaluate to

$$\boldsymbol{u}_{\alpha\beta}(t) = u_{\mathrm{DC}}(t)\boldsymbol{T}_{\alpha\beta\mathrm{abc}}\boldsymbol{s}_{\mathrm{abc}}(t). \tag{2.3}$$

Due to the possible combinations of switch positions, the inverter can realize $2^3 = 8$ switching states. The definition of the switching state s_n for given switch positions $s_{\mathrm{a,b,c}}$ of the inverter as well as the resulting voltages in the $\alpha\beta$ frame are listed in Tab. 2.1 and depicted in Fig. 2.2.

The actual realization of the inverter with insulated-gate bipolar transistors (IGBT), that is considered in this work, is shown in Fig. 2.3. When a switch is desired in a phase leg of the inverter, the switching of the IGBT that was not previously in conducting mode is delayed for a short time, also known as interlocking time, to avoid a hard short circuit in the associated half bridge of the inverter. On the one hand, this practice is necessary to prevent destruction of the inverter, but on the other hand, the interlocking time introduces a nonlinearity that can distort the average output voltages during a sampling period of modulator-based control schemes. Numerous methods [60–64] exist to compensate for this inverter nonlinearity. In Sec. 3.5 the distorting effect of the interlocking time on the inverter output voltage and the compensation strategy applied in this work are briefly described.

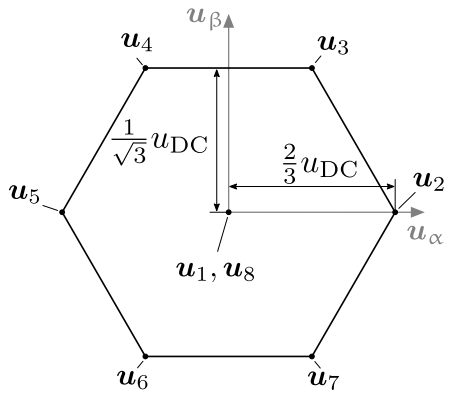

Fig. 2.2: Elementary voltage vectors in the stator-fixed αβ frame

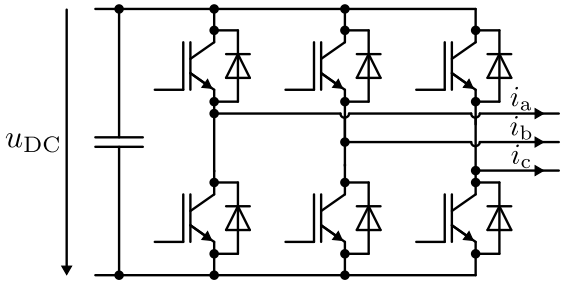

Fig. 2.3: Three-phase two-level IGBT inverter

2.3 Synchronous Machine Model

The proposed control scheme requires discrete-time SM model variants for predicting the flux linkage $\boldsymbol{\psi}_{\alpha\beta}$ in the αβ coordinate system (cf. (2.5)), the current $\boldsymbol{i}_{\mathrm{dq}}$ in the dq coordinate system (cf. (2.11)), as well as the airgap torque T (cf. (2.15)).

2.3.1 Flux Linkage Model in the Stator-Fixed Frame

According to Faraday's law of induction, the differential equation of the flux linkage $\boldsymbol{\psi}_{\alpha\beta}$ of an SM can be written as

$$\frac{\mathrm{d}}{\mathrm{d}t}\boldsymbol{\psi}_{\alpha\beta}(t) = \boldsymbol{u}_{\alpha\beta}(t) - R_{\mathrm{s}}\boldsymbol{i}_{\alpha\beta}(t) \tag{2.4}$$

with the ohmic stator resistance R_{s}. By applying the forward Euler method, the differential equation (2.4) can be approximated in discrete time with the sampling time T_{s}:

$$\boldsymbol{\psi}_{\alpha\beta}[k+1] = \underbrace{\boldsymbol{I}_2}_{\boldsymbol{A}_\psi}\boldsymbol{\psi}_{\alpha\beta}[k] + \underbrace{T_{\mathrm{s}}\boldsymbol{I}_2}_{\boldsymbol{B}_\psi}\boldsymbol{u}_{\alpha\beta}[k] \underbrace{-T_{\mathrm{s}}R_{\mathrm{s}}\boldsymbol{i}_{\alpha\beta}[k]}_{\boldsymbol{E}_\psi(\boldsymbol{i}_{\alpha\beta}[k])}. \tag{2.5}$$

Here, k denotes the discrete time step and I_2 the identity matrix. For a general nonlinearly magnetized SM with significant cross-saturation effects, the current-to-flux relationship is represented by a nonlinear function

$$\boldsymbol{\psi}_{\mathrm{dq}} = \boldsymbol{f}(\boldsymbol{i}_{\mathrm{dq}}). \tag{2.6}$$

in the rotor-fixed coordinate system. An exemplary nonlinear current-to-flux linkage coupling of a nonlinearly magnetized IPMSM is shown in Fig. A.2.

2.3.2 Current Model in the Rotor-Fixed Frame

To derive the difference equation of the current $\boldsymbol{i}_{\mathrm{dq}}$, the machine model (2.5) must be transformed into the dq coordinate system

$$\boldsymbol{\psi}_{\mathrm{dq}}[k{+}1] = \boldsymbol{T}_{\mathrm{\alpha\beta dq}}(-T_{\mathrm{s}}\omega[k])(\boldsymbol{\psi}_{\mathrm{dq}}[k] + T_{\mathrm{s}}(\boldsymbol{u}_{\mathrm{dq}}[k] - R_{\mathrm{s}}\boldsymbol{i}_{\mathrm{dq}}[k])), \tag{2.7}$$

with the identity

$$\boldsymbol{T}_{\mathrm{\alpha\beta dq}}(\varepsilon[k] - \varepsilon[k+1]) = \boldsymbol{T}_{\mathrm{dq\alpha\beta}}(\varepsilon[k+1])\boldsymbol{T}_{\mathrm{\alpha\beta dq}}(\varepsilon[k]) \tag{2.8}$$

and the approximation $\varepsilon[k+1] - \varepsilon[k] \approx T_{\mathrm{s}}\omega[k]$. The term $\boldsymbol{T}_{\mathrm{\alpha\beta dq}}\left(-T_{\mathrm{s}}\omega[k]\right)$ considers the rotation of the dq against the $\mathrm{\alpha\beta}$ coordinate system during a sampling period with the electrical angular velocity ω [30, 65, 66]. To relate the variation of the flux linkage $\boldsymbol{\psi}_{\mathrm{dq}}$ to the variation of the current $\boldsymbol{i}_{\mathrm{dq}}$, the differential inductance matrix

$$\boldsymbol{L}_{\mathrm{dq},\Delta}(\boldsymbol{i}_{\mathrm{dq}}) = \begin{bmatrix} L_{\mathrm{dd}}(\boldsymbol{i}_{\mathrm{dq}}) & L_{\mathrm{dq}}(\boldsymbol{i}_{\mathrm{dq}}) \\ L_{\mathrm{qd}}(\boldsymbol{i}_{\mathrm{dq}}) & L_{\mathrm{qq}}(\boldsymbol{i}_{\mathrm{dq}}) \end{bmatrix} = \begin{bmatrix} \frac{\partial \psi_{\mathrm{d}}}{\partial i_{\mathrm{d}}} & \frac{\partial \psi_{\mathrm{d}}}{\partial i_{\mathrm{q}}} \\ \frac{\partial \psi_{\mathrm{q}}}{\partial i_{\mathrm{d}}} & \frac{\partial \psi_{\mathrm{q}}}{\partial i_{\mathrm{q}}} \end{bmatrix} \tag{2.9}$$

is considered. Exemplary differential inductance and flux linkage maps of a nonlinearly magnetized IPMSM with significant (cross-)saturation effects are depicted in Fig. A.2 and Fig. A.3. By approximating (2.9) with

$$\underbrace{\Delta\boldsymbol{\psi}_{\mathrm{dq}}[k+1]}_{\boldsymbol{\psi}_{\mathrm{dq}}[k+1]-\boldsymbol{\psi}_{\mathrm{dq}}[k]} \approx \boldsymbol{L}_{\mathrm{dq},\Delta}\left(\boldsymbol{i}_{\mathrm{dq}}[k]\right) \underbrace{\Delta\boldsymbol{i}_{\mathrm{dq}}[k+1]}_{\boldsymbol{i}_{\mathrm{dq}}[k+1]-\boldsymbol{i}_{\mathrm{dq}}[k]} \tag{2.10}$$

and inserting (2.10) into (2.7), the discrete-time current difference equation of an SM considering (cross-)saturation effects in the dq coordinate system evaluates to

$$\begin{aligned} \boldsymbol{i}_{\mathrm{dq}}[k+1] =& \boldsymbol{A}_{\boldsymbol{i}}(\boldsymbol{i}_{\mathrm{dq}}[k])\boldsymbol{i}_{\mathrm{dq}}[k] + \boldsymbol{B}_{\boldsymbol{i}}(\boldsymbol{i}_{\mathrm{dq}}[k],\omega[k])\boldsymbol{u}_{\mathrm{dq}}[k] + \boldsymbol{E}_{\boldsymbol{i}}(\boldsymbol{i}_{\mathrm{dq}}[k],\omega[k]) \\ & \text{with:} \\ \boldsymbol{A}_{\boldsymbol{i}}(\boldsymbol{i}_{\mathrm{dq}}[k]) =& \boldsymbol{I}_2 - \boldsymbol{L}_{\mathrm{dq},\Delta}^{-1}(\boldsymbol{i}_{\mathrm{dq}}[k])R_{\mathrm{s}}T_{\mathrm{s}}, \\ \boldsymbol{B}_{\boldsymbol{i}}(\boldsymbol{i}_{\mathrm{dq}}[k],\omega[k]) =& \boldsymbol{L}_{\mathrm{dq},\Delta}^{-1}(\boldsymbol{i}_{\mathrm{dq}}[k])\boldsymbol{T}_{\mathrm{\alpha\beta dq}}(-T_{\mathrm{s}}\omega[k])T_{\mathrm{s}}, \\ \boldsymbol{E}_{\boldsymbol{i}}(\boldsymbol{i}_{\mathrm{dq}}[k],\omega[k]) =& \boldsymbol{L}_{\mathrm{dq},\Delta}^{-1}(\boldsymbol{i}_{\mathrm{dq}}[k])\left[\boldsymbol{T}_{\mathrm{\alpha\beta dq}}(-T_{\mathrm{s}}\omega[k]) - \boldsymbol{I}_2\right]\boldsymbol{\psi}_{\mathrm{dq}}(\boldsymbol{i}_{\mathrm{dq}}[k]). \end{aligned} \tag{2.11}$$

For the sake of compactness, the parameter-varying matrices $\boldsymbol{A}_{\boldsymbol{i}}(\boldsymbol{i}_{\mathrm{dq}}[k]), \boldsymbol{B}_{\boldsymbol{i}}(\boldsymbol{i}_{\mathrm{dq}}[k],\omega[k])$, $\boldsymbol{E}_{\boldsymbol{i}}(\boldsymbol{i}_{\mathrm{dq}}[k],\omega[k]), \boldsymbol{E}_{\boldsymbol{\psi}}\left(\boldsymbol{i}_{\mathrm{\alpha\beta}}[k]\right)$ are abbreviated with $\boldsymbol{A}_{\boldsymbol{i}}[k], \boldsymbol{B}_{\boldsymbol{i}}[k], \boldsymbol{E}_{\boldsymbol{i}}[k], \boldsymbol{E}_{\boldsymbol{\psi}}[k]$ in the following.

2.3.3 Torque Model

The airgap torque of an SM is given by

$$T[k] = \frac{3}{2}p\left(\psi_{\mathrm{d}}[k]i_{\mathrm{q}}[k] - \psi_{\mathrm{q}}[k]i_{\mathrm{d}}[k]\right) \tag{2.12}$$

with the pole pair number p. By linearizing (2.12) with respect to the current, the current-torque relationship can be approximated by

$$T[k+1] \approx T[k] + \left(\frac{\partial T[k]}{\partial \boldsymbol{i}_{\mathrm{dq}}}\right)^{\mathsf{T}} \Delta \boldsymbol{i}_{\mathrm{dq}}[k+1]. \tag{2.13}$$

Here, the partial derivative

$$\frac{\partial T[k]}{\partial \boldsymbol{i}_{\mathrm{dq}}} = \frac{3}{2} p \begin{bmatrix} L_{\mathrm{dd}}[k] i_{\mathrm{q}}[k] - L_{\mathrm{qd}}[k] i_{\mathrm{d}}[k] - \psi_{\mathrm{q}}[k] \\ L_{\mathrm{dq}}[k] i_{\mathrm{q}}[k] - L_{\mathrm{qq}}[k] i_{\mathrm{d}}[k] + \psi_{\mathrm{d}}[k] \end{bmatrix} \tag{2.14}$$

is calculated from (2.12) and (2.9). Inserting the current model (2.11) for the current difference $\Delta \boldsymbol{i}_{\mathrm{dq}}$ into (2.13) results in the torque model given by

$$T[k+1] = \underbrace{\boldsymbol{I}_2}_{\boldsymbol{A}_T} T[k] + \underbrace{\left(\frac{\partial T[k]}{\partial \boldsymbol{i}_{\mathrm{dq}}}\right)^{\mathsf{T}} \boldsymbol{B}_{\boldsymbol{i}}[k]}_{\boldsymbol{B}_T[k]} \boldsymbol{u}_{\mathrm{dq}}[k] + \underbrace{\left(\frac{\partial T[k]}{\partial \boldsymbol{i}_{\mathrm{dq}}}\right)^{\mathsf{T}} \left(\left(\boldsymbol{A}_{\boldsymbol{i}}[k] - \boldsymbol{I}_2\right) \boldsymbol{i}_{\mathrm{dq}}[k] + \boldsymbol{E}_{\boldsymbol{i}}[k]\right)}_{\boldsymbol{E}_T[k]}. \tag{2.15}$$

2.4 Overmodulation

To increase the output power of the drive during steady-state operation, the available DC-link voltage must be utilized to its maximum extent. This is achieved by entering the overmodulation range up to six-step operation. The following description of overmodulation assumes steady-state operation, a continuous control set of the voltage hexagon, and time-continuous quantities. During six-step operation there is no modulation and the elementary voltage vectors are switched counterclockwise every sixth of the fundamental time period for positive speeds and clockwise for negative speeds. This square-shaped curve results in a maximum possible magnitude of the fundamental voltage[1] $\|\boldsymbol{u}_{\alpha\beta,\mathrm{f}}\|$ of $2/\pi u_{\mathrm{DC}}$ [57] and to a minimum switching frequency f_{sw} that is equal to the fundamental frequency, i.e., $f_{\mathrm{sw}} = \omega/(2\pi)$. To characterize the magnitude of the fundamental voltage, the modulation index

$$m = \frac{\|\boldsymbol{u}_{\alpha\beta,\mathrm{f}}\|}{\frac{2}{\pi} u_{\mathrm{DC}}} \tag{2.16}$$

is used as a normalization.

Fig. 2.4 shows the ranges that can be covered by the fundamental voltage $\boldsymbol{u}_{\alpha\beta,\mathrm{f}}$ in the linear and overmodulation range. Neglecting the switching harmonics of the space vector modulation (SVM), cf. Sec. 3.4, sinusoidal output voltages $\boldsymbol{u}_{\alpha\beta}$ are generated within the linear modulation range, i.e., $\boldsymbol{u}_{\alpha\beta}(t) = \boldsymbol{u}_{\alpha\beta,\mathrm{f}}(t)$. If the magnitude of the fundamental voltage is to be increased beyond the linear modulation range, the overmodulation range, which ends with six-step operation, must be exploited. Operating in the overmodulation range leads to additional voltage harmonics, since the boundaries of the voltage hexagon of the inverter no longer allow the generation of sinusoidal voltages $\boldsymbol{u}_{\alpha\beta}(t)$. To synthesize the voltage trajectories $\boldsymbol{u}_{\alpha\beta}(t)$ that satisfy the voltage constraint (hexagon) for a given fundamental voltage $\boldsymbol{u}_{\alpha\beta,\mathrm{f}}(t)$, an overmodulation scheme must be applied. In Fig. 2.5 the inputs and outputs of a general overmodulation scheme are shown. Here, the applied overmodulation method has to calculate $\boldsymbol{u}_{\alpha\beta}(t)/u_{\mathrm{DC}}$ based on m and $\angle \boldsymbol{u}_{\alpha\beta,\mathrm{f}}$ in such a way that the fundamental of the resulting output voltage trajectory $\boldsymbol{u}_{\alpha\beta}(t)$ is equal to

[1] The fundamental voltage vector $\boldsymbol{u}_{\alpha\beta,\mathrm{f}}(t)$ with constant magnitude $\|\boldsymbol{u}_{\alpha\beta,\mathrm{f}}\|$ rotates with the rotor speed ω

the input $\boldsymbol{u}_{\alpha\beta,\mathrm{f}}(t)$. Since different trajectories $\boldsymbol{u}_{\alpha\beta}(t)$ result in the same fundamental $\boldsymbol{u}_{\alpha\beta,\mathrm{f}}(t)$, there is no unique solution to calculate $\boldsymbol{u}_{\alpha\beta}(t)/u_{\mathrm{DC}}$ for given $m, \angle\boldsymbol{u}_{\alpha\beta,\mathrm{f}}(t)$, and thus numerous overmodulation methods exist. Here, a few of them can be mentioned [38, 39, 54, 56]. In this thesis, method [39] is applied because of the low harmonic distortion of the resulting output voltage trajectories [57]. However, overmodulation method [39] is not used in this work to manipulate the output voltage of the closed-loop controller. Instead, the voltage trajectories of the overmodulation scheme are needed to calculate the reference flux linkage trajectories and to enable closed-loop control operation in the overmodulation range described in Ch. 4.

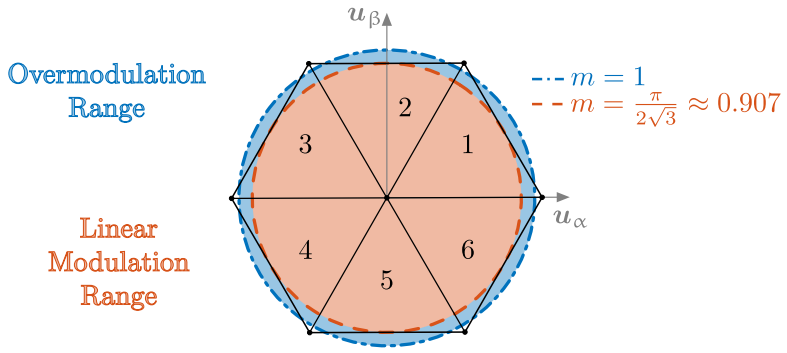

Fig. 2.4: Linear and overmodulation range, cf. (2.16), and the definitions of the inverter hexagon sectors

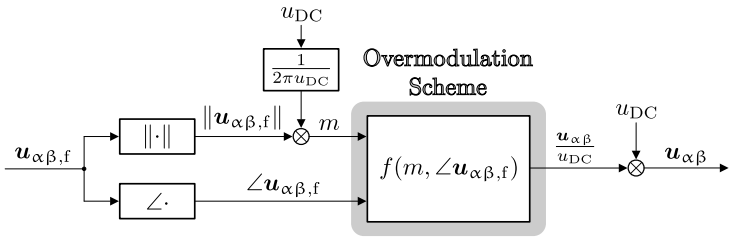

Fig. 2.5: Inputs $m, \angle\boldsymbol{u}_{\alpha\beta,\mathrm{f}}$ and normalized output $\boldsymbol{u}_{\alpha\beta}/u_{\mathrm{DC}}$ of a general overmodulation scheme

In the following, the applied overmodulation scheme [39] is briefly summarized. An insightful comparison of the overmodulation scheme [39] with the scheme proposed in [38] can be found in [57]. To calculate the output voltage $\boldsymbol{u}_{\alpha\beta}(t)$, the method [39] distinguishes the overmodulation range between mode I ($0.907 < m \leq 0.952$) and mode II ($0.952 < m \leq 1$).

In overmodulation mode I, the angle of the output voltage $\boldsymbol{u}_{\alpha\beta}(t)$ is equal to the angle of the input voltage $\boldsymbol{u}_{\alpha\beta,\mathrm{f}}(t)$, i.e., $\angle\boldsymbol{u}_{\alpha\beta}(t) = \angle\boldsymbol{u}_{\alpha\beta,\mathrm{f}}(t)$. The trajectory of the output voltage $\boldsymbol{u}_{\alpha\beta}(t)$ results from a circular trajectory rotating with radius r and rotor speed ω, whereby the infeasible voltage values of this circular trajectory are scaled such that they lie on the voltage hexagon boundary, see Fig. 2.6. To compensate for the reduction of the fundamental component $\boldsymbol{u}_{\alpha\beta}(t)$ by the voltage hexagon boundaries, the radius r must be increased compared to $\|\boldsymbol{u}_{\alpha\beta,\mathrm{f}}\|$. For a radius of $r = 2/3u_{\mathrm{DC}}$, the maximum possible modulation index of $m = 0.952$ is reached in mode I and the voltage trajectory lies entirely on the voltage hexagon boundaries.

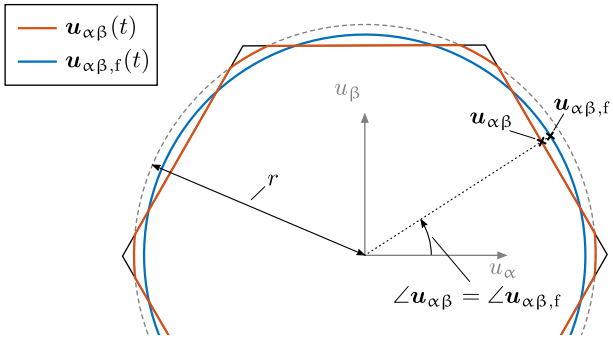

Fig. 2.6: Exemplary output voltage $\boldsymbol{u}_{\alpha\beta}(t)$ for a given input fundamental voltage $\boldsymbol{u}_{\alpha\beta,\mathrm{f}}(t)$ in overmodulation mode I (cf. [39])

In overmodulation mode II, the output voltage trajectory $\boldsymbol{u}_{\alpha\beta}(t)$ is located solely on the voltage hexagon boundaries, i.e., switching to zero voltage vectors for the SVM is no longer optimal. To increase the modulation index above $m = 0.952$ the angle condition $\angle\boldsymbol{u}_{\alpha\beta}(t) = \angle\boldsymbol{u}_{\alpha\beta,\mathrm{f}}(t)$ of overmodulation mode I must be violated. The construction of the output voltage vectors in overmodulation mode II is shown in Fig. 2.7 and explained in the following for the voltage hexagon sector 1. As long as the input fundamental voltage $\boldsymbol{u}_{\alpha\beta,\mathrm{f}}(t)$ is within the gray area defined by $\gamma \in]0, \pi/6]$, the output voltage $\boldsymbol{u}_{\alpha\beta}(t)$ is equal to the corresponding elementary voltage vector[2]. When $\boldsymbol{u}_{\alpha\beta,\mathrm{f}}(t)$ starting from $\angle\boldsymbol{u}_{\alpha\beta,\mathrm{f}} = 0$ passes the boundary of the gray area the output voltage $\boldsymbol{u}_{\alpha\beta}(t)$ moves with a constant angular velocity on the voltage hexagon boundary to the next elementary vector. The constant angular velocity is set in such a way that $\boldsymbol{u}_{\alpha\beta}(t)$ reaches the next elementary vector when $\boldsymbol{u}_{\alpha\beta,\mathrm{f}}(t)$ enters the next gray area. Since the output voltage $\boldsymbol{u}_{\alpha\beta}(t)$ is always on the hexagonal voltage boundary, it is uniquely defined by its angle $\angle\boldsymbol{u}_{\alpha\beta}(t)$. Therefore, the previous construction of $\boldsymbol{u}_{\alpha\beta}(t)$ can be represented in a compact form (in hexagon sector 1) by

$$\angle\boldsymbol{u}_{\alpha\beta} = \begin{cases} 0 & 0 \le \angle\boldsymbol{u}_{\alpha\beta,\mathrm{f}} \le \gamma, \\ \frac{\angle\boldsymbol{u}_{\alpha\beta,\mathrm{f}} - \gamma}{\pi/6 - \gamma} \cdot \frac{\pi}{6} & \gamma < \angle\boldsymbol{u}_{\alpha\beta,\mathrm{f}} < \frac{\pi}{3} - \gamma, \\ \frac{\pi}{3} & \frac{\pi}{3} - \gamma \le \angle\boldsymbol{u}_{\alpha\beta,\mathrm{f}} \le \frac{\pi}{3}. \end{cases} \tag{2.17}$$

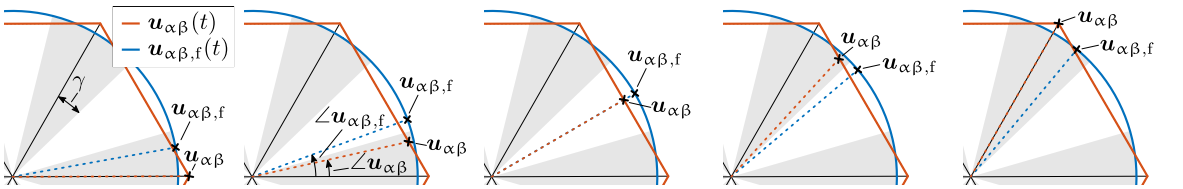

(a) $\angle\boldsymbol{u}_{\alpha\beta,\mathrm{f}} = \frac{\pi}{18}$ **(b)** $\angle\boldsymbol{u}_{\alpha\beta,\mathrm{f}} = 2\frac{\pi}{18}$ **(c)** $\angle\boldsymbol{u}_{\alpha\beta,\mathrm{f}} = 3\frac{\pi}{18}$ **(d)** $\angle\boldsymbol{u}_{\alpha\beta,\mathrm{f}} = 4\frac{\pi}{18}$ **(e)** $\angle\boldsymbol{u}_{\alpha\beta,\mathrm{f}} = 5\frac{\pi}{18}$

Fig. 2.7: Exemplary output voltage $\boldsymbol{u}_{\alpha\beta}(t)$ for a given input fundamental voltage $\boldsymbol{u}_{\alpha\beta,\mathrm{f}}(t)$ in overmodulation mode II (cf. [39])

[2]The angle γ represents the degree of freedom for overmodulation mode II to adjust the magnitude of the fundamental voltage.

The previous two paragraphs described the construction of the output voltage trajectories $\boldsymbol{u}_{\alpha\beta}(t)$ for $\angle\boldsymbol{u}_{\alpha\beta,\mathrm{f}}(t)$ in mode I and mode II. Here, the output $\boldsymbol{u}_{\alpha\beta}(t)$ depends on the radius r in mode I and on the angle γ in mode II. The values of r and γ must be chosen such that the fundamental of $\boldsymbol{u}_{\alpha\beta}(t)$ is equal to the input $\boldsymbol{u}_{\alpha\beta,\mathrm{f}}(t)$. To compute r and γ for a given reference input modulation index m, the nonlinear equations given in [39, 57] must be solved. In Fig. 2.8 the resulting output voltage trajectories $\boldsymbol{u}_{\alpha\beta}(t)$ for inputs m and $\angle\boldsymbol{u}_{\alpha\beta,\mathrm{f}}(t)$ are depicted.

Calculating $\boldsymbol{u}_{\alpha\beta}$ by solving nonlinear equations for given m and $\angle\boldsymbol{u}_{\alpha\beta,\mathrm{f}}(t)$ is computationally intensive during online operation. For this reason, it is more efficient to store the output voltage values as a function of m and $\angle\boldsymbol{u}_{\alpha\beta,\mathrm{f}}(t)$ in two-dimensional look-up tables (LUT), see Fig. 2.9. Here, the dual-mode property of the applied overmodulation scheme [39] can be seen in Fig. 2.9, because for a modulation index of $m > 0.952$ the voltage vector u_β in the voltage hexagon sector 2 lies exclusively on the voltage boundary, resulting in $u_\beta = 1/\sqrt{3}u_{\mathrm{DC}} \approx 0.5774u_{\mathrm{DC}}$. Note that this precalculation of the LUTs is completely independent of the specific drive design (machine and inverter rating) and, therefore, does not limit the scope of the overmodulation method.

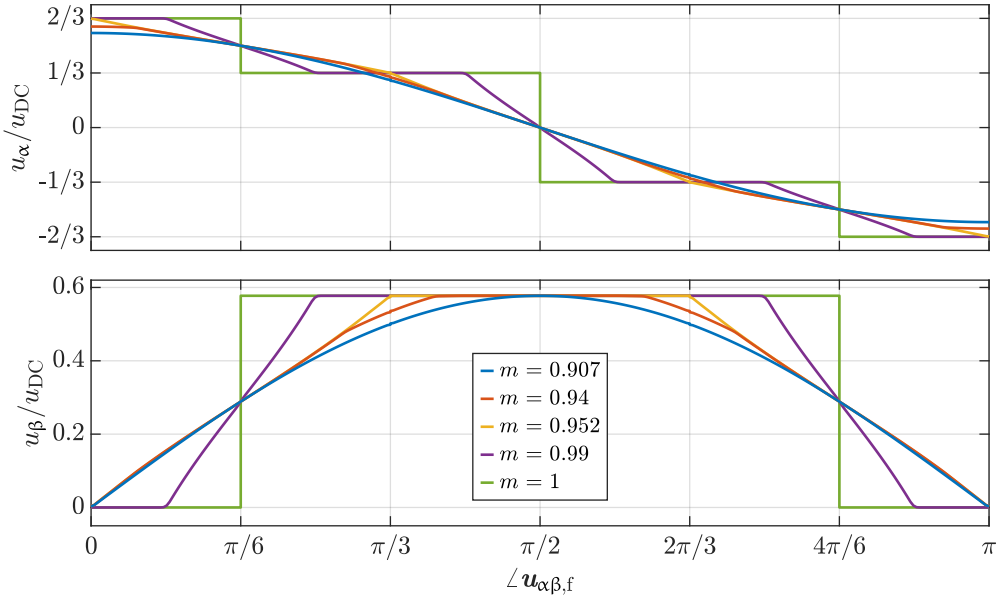

Fig. 2.8: Exemplary voltage trajectories for different modulation indices

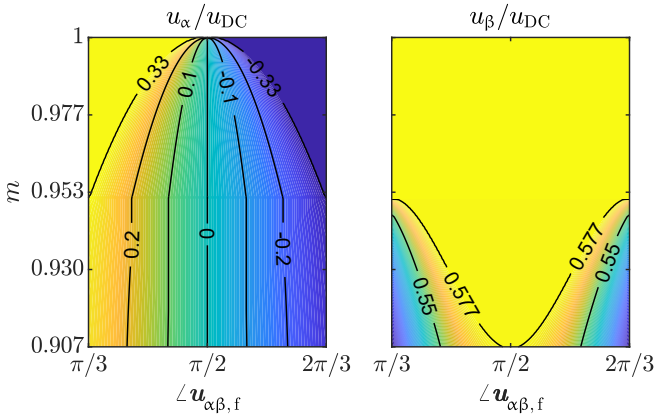

Fig. 2.9: Voltage values as a function of the modulation index m and the angle of the fundamental voltage $\angle \boldsymbol{u}_{\alpha\beta,\mathrm{f}}$ for voltage hexagon sector 2 [6, Fig. 7]

2.5 Optimal Control

Optimal control theory deals with the problem of finding a control input for a dynamical system over a period of time such that a certain objective function is optimized. In this thesis, as mentioned in Sec. 1.3, the solution of a TOC problem without considering state constraints is used to manipulate the flux linkage reference of an MPC with state and input constraints. MPC and TOC are both branches of optimal control. Therefore, the concept of optimal control is briefly summarized based on the optimization problem of a general optimal controller. Subsequently, the methods of MPC and TOC are described in Sec. 2.5.1 and Sec. 2.5.2.

For a continuous-time nonlinear dynamical system, a general optimal control problem is given by

$$\min_{\boldsymbol{u}(t)} \underbrace{\vartheta(\boldsymbol{x}(t_1), t_1) + \int_{t_0}^{t_1} \Phi(\boldsymbol{x}(t), \boldsymbol{u}(t), t)\mathrm{d}t}_{J(\boldsymbol{x}(t),\boldsymbol{u}(t),t_0,t_1)} \tag{2.18a}$$

$$\text{s.t. } \frac{\mathrm{d}}{\mathrm{d}t}\boldsymbol{x}(t) = \boldsymbol{f}_\mathrm{c}(\boldsymbol{x}(t), \boldsymbol{u}(t), t), \quad \boldsymbol{x}(t_0) = \boldsymbol{x}_0, \tag{2.18b}$$

$$\boldsymbol{h}(\boldsymbol{x}(t), \boldsymbol{u}(t), t) \leq \boldsymbol{0} \quad \forall t \in [t_0, t_1], \tag{2.18c}$$

$$\boldsymbol{g}(\boldsymbol{x}(t_1), t_1) = \boldsymbol{0}. \tag{2.18d}$$

Here, $\boldsymbol{x}(t)$ is the state trajectory and $\boldsymbol{u}(t)$ the input trajectory. The time t varies between an initial time t_0 and a terminal time t_1, which can be free or set to a predefined value. The ODE (2.18b) describes the evolution of the state $\boldsymbol{x}(t)$ as a function of the input trajectory $\boldsymbol{u}(t)$ starting from the initial state $\boldsymbol{x}_0$. The path constraints (2.18c) and the terminal condition (2.18d) are optional and can be used to incorporate state as well as input constraints (path constraints) and to force the terminal state $\boldsymbol{x}(t_1)$ to a certain value or to lie on a certain manifold (terminal condition). The resulting control characteristics, i.e., $\boldsymbol{x}(t)$ and $\boldsymbol{u}(t)$, depend on the cost functional J with its terminal costs ϑ and running costs Φ. Therefore, the requirements on the control characteristics, e.g., minimum fuel consumption of a rocket flight, minimum travel time of a car

on a hilly road, or maximum amount of a chemical produced in a given time, must be formulated as an appropriate cost functional.

To obtain optimal input $\boldsymbol{u}(t)$ and state trajectories $\boldsymbol{x}(t)$, the dynamic optimization problem (2.18) must be solved. Only small-dimensional optimal control problems with simplified assumptions, e.g., linear dynamical system, box constraints on inputs and/or states, etc., can be solved analytically. In general, numerical methods have to be applied. The solution methods can be categorized into direct and indirect methods. Indirect methods apply the calculus of variations to obtain first-order optimality conditions for the dynamic program. This results in a BVP, which must be discretized and solved with numerical methods. In contrast, direct methods transform the dynamic optimization problem into a static one by discretizing the control and state trajectories, the cost function, the dynamical system, and the (in)equality constraints. By applying static optimization solvers, such as active-set or interior-point methods, the solution of the discretized optimization problem can be calculated. For this reason, indirect methods are summarized as "first optimize, then discretize" strategy, while direct methods are summarized as "first discretize, then optimize" strategy [67]. Methods for solving optimal control problems can be found in [68–72], where [70, 71] provide an overview and a comparison of different methods.

2.5.1 Model Predictive Control

The simplest way to implement an optimal controller is to solve (2.18) with a direct or indirect method and apply the optimal input $\boldsymbol{u}(t)$ to the dynamical system as a function of time in an open-loop manner. However, in real applications, the use of open-loop optimal controllers can lead to distorted control performance, i.e., distorted control accuracy and distorted transient operation. The reason for this is that the open-loop optimal controller cannot account for the effects of disturbances, model mismatch, or other parasitic effects.

To increase robustness to the aforementioned distortions, it is recommended to implement optimal controllers in a closed-loop fashion. A popular and extensively studied closed-loop optimal control method is the MPC scheme. Here, an open-loop optimal control problem is solved with the direct method, i.e., the optimal control problem is transformed into a static optimization problem by means of discretization and is solved thereafter. The step size of the discretization of the optimization problem of the MPC usually coincides with the sampling period of the discrete-time operating controller. To close the control loop, the optimization problem of the MPC

$$\min_{\boldsymbol{u}[0|k],\ldots,\boldsymbol{u}[N_{\mathrm{mpc}}-1|k]} \vartheta(\boldsymbol{x}[N_{\mathrm{mpc}}|k],k) + \sum_{n=0}^{N_{\mathrm{mpc}}-1} \ell(\boldsymbol{x}[n+1|k],\boldsymbol{u}[n|k],k) \tag{2.19a}$$

$$\text{s.t. } \boldsymbol{x}[n+1|k] = \boldsymbol{f}_{\mathrm{d}}(\boldsymbol{x}[n|k]),\boldsymbol{u}[n|k],k), \quad \boldsymbol{x}[0|k] = \boldsymbol{x}[k] \tag{2.19b}$$

$$\boldsymbol{h}(\boldsymbol{x}[n+1|k],\boldsymbol{u}[n|k],k) \leq \boldsymbol{0}, \quad n = 0,\ldots,N_{\mathrm{mpc}}-1 \tag{2.19c}$$

is solved each controller sampling instant k, where $\boldsymbol{u}[n|k]$ and $\boldsymbol{x}[n|k]$ denote the predicted control input and state, respectively, for time index $k+n$ based on the information available at sampling instant k [73]. With the discrete-time model (2.19b) of the dynamical system, the discretized state trajectory $\boldsymbol{x}[n+1|k],\ n = 0,\ldots,N_{\mathrm{mpc}}-1$ is predicted starting from a measured or estimated initial state $\boldsymbol{x}[k]$ as a function of the input trajectory $\boldsymbol{u}[n|k]$ within the prediction horizon N_{mpc}. The control values $\boldsymbol{u}[0|k],\ldots,\boldsymbol{u}[N_{\mathrm{mpc}}-1|k]$ are varied by the applied static optimization method in such a way that the cost function (2.19a) consisting of terminal ϑ and stage costs ℓ is minimized, while the inequality constraint (2.19c) must be satisfied. A terminal state condition as in (2.18)

is usually not applied for MPCs, as the prediction horizon must be long enough to ensure that the final state satisfies the terminal condition, otherwise the optimization problem (2.19) would become infeasible.

Instead of actuating the entire predicted discrete control trajectory $\boldsymbol{u}[n|k],\ n = 0, ..., N_{\mathrm{mpc}} - 1$, only the first entry $\boldsymbol{u}[0|k]$ is applied to the system. The process of solving (2.19) and actuating $\boldsymbol{u}[0|k]$ is repeated at each sampling instant which is known as the receding horizon principle. Since state feedback is provided by (2.19b), the control loop is closed and the MPC can act against distortions and disturbances.

One of the major advantages of MPC compared to other modern advanced control methods, e.g., sliding mode control, linear quadratic regulator, backstepping control, gain-scheduled proportional-integral-derivative control, or reinforcement learning, is that input and state constraints can be directly incorporated via the inequality constraint (2.19c).

Detailed investigations, e.g., the influence of the length of the prediction horizon, the sampling time, or the choice of the tuning parameters of the cost function on the control performance, optimality, and stability, can be found in [40, 73–77].

2.5.2 Time-Optimal Control

In many control engineering problems, the control trajectory $\boldsymbol{u}(t)$ is of interest which steers the state $\boldsymbol{x}(t)$ of a system to a given reference trajectory $\boldsymbol{x}^*(t)$ in the shortest possible time. This control characteristic is referred to as TOC and its optimization problem

$$\min_{\boldsymbol{u}(t)} t_1 \tag{2.20a}$$

$$\text{s.t. } \frac{\mathrm{d}}{\mathrm{d}t}\boldsymbol{x}(t) = \boldsymbol{f}_{\mathrm{c}}(\boldsymbol{x}(t), \boldsymbol{u}(t), t), \quad \boldsymbol{x}(t_0) = \boldsymbol{x}_0, \tag{2.20b}$$

$$\boldsymbol{h}(\boldsymbol{x}(t), \boldsymbol{u}(t), t) \leq \boldsymbol{0} \quad \forall t \in [t_0, t_1], \tag{2.20c}$$

$$\boldsymbol{x}(t_1) = \boldsymbol{x}^*(t_1) \tag{2.20d}$$

represents a special case of the optimal control problem (2.18). Here, the time t_1 (2.20a) needed to steer the state $\boldsymbol{x}(t)$ to its reference $\boldsymbol{x}^*$ (2.20d) is minimized. In this work, a TOC with the flux linkage in the $\alpha\beta$ frame as state variable without state constraints and circular input constraints is employed and solved in Sec. 5.1.2. Here, the indirect method of Pontryagin's principle [78] is used to derive the necessary first-order optimality conditions. The resulting BVP is solved with an efficient numerical method described in Sec. 5.1.2.

3 General Control Framework

The contributions presented in this thesis can be considered as extensions of a conventional CCS-MPFC scheme. This control scheme serves as a baseline and includes a well-known OPC [11], a conceptually simple CCS-MPFC, an SVM [79], and a Gopinath-style flux observer (GFO) [80, 81], cf. Fig. 3.1. The elements of this general control framework, i.e., OPC, CCS-MPFC, SVM, and GFO, are briefly summarized in this chapter. Compared to the extensions described in the following chapters, the general control framework achieves only time-suboptimal control performance during transients and is limited to the linear modulation range during steady-state operation.

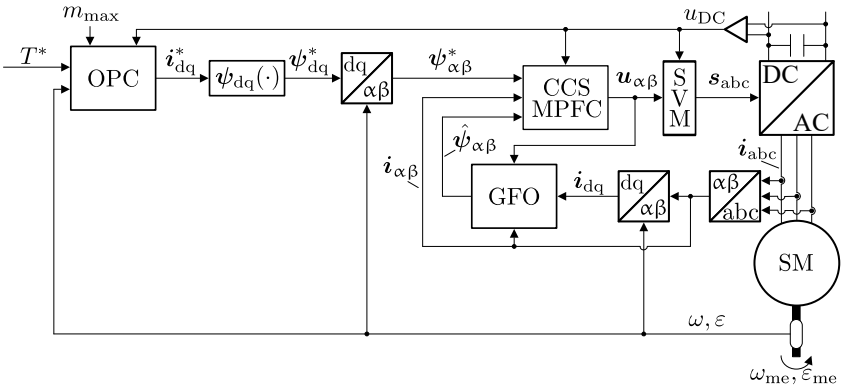

Fig. 3.1: General control framework serving as baseline for the extensions presented in the subsequent chapters

3.1 Operating Point Controller

The schemes studied in this thesis contain closed-loop flux linkage controllers. Therefore, an OPC (higher-level open-loop torque controller) must be applied to convert the reference torque T^* into an appropriate reference state of the SM, i.e., reference currents or flux linkages. A reference torque T^* can be realized by various state combinations, cf. (2.12). This additional degree of freedom is usually exploited by the OPC to select the operating point $\boldsymbol{i}^*_{\mathrm{dq}}$ with the shortest length to minimize losses, e.g., ohmic losses. In addition, the OPC must consider voltage and current limits to ensure safe operation and prevent thermal overload of the drive system.

For linearly magnetized SMs, the operating point $\boldsymbol{i}^*_{\mathrm{dq}}$ with the shortest length that satisfies voltage and current limits can be calculated analytically. Here, intersections between machine

characteristic maximum torque per current (MTPC)[1], maximum torque per voltage (MTPV), current limit, voltage limit, and iso-torque loci must be calculated. Since these loci can be represented by quadrics

$$\boldsymbol{i}_{\mathrm{dq}}^{\mathsf{T}}\boldsymbol{H}_x\boldsymbol{i}_{\mathrm{dq}} + \boldsymbol{h}_x\boldsymbol{i}_{\mathrm{dq}} + \eta_x = 0 \tag{3.1}$$

for $x \in \{\boldsymbol{I}_{\max},$ iso-torque, iso-voltage, MTPC, MTPV$\}$ due to the linear magnetization of the machine, the intersections can be calculated analytically by finding the roots of quartic equations (fourth order polynomials). With the help of a decision tree, the intersection with the smallest magnitude that respect current and voltage constraints is chosen as operating point [82].

Machine characteristic loci of nonlinearly magnetized SMs cannot be represented by quadrics due to significant magnetic (cross-)saturation effects. Therefore, OPC methods exist that calculate the operating point numerically using static machine characteristic loci based on LUTs [21]. Instead, the OPC method proposed in [11, 82] is applied in this work. Here, the nonlinear magnetization is taken into account iteratively by a successive linearization

$$\boldsymbol{\psi}_{\mathrm{dq}}(\boldsymbol{i}_{\mathrm{dq}}) = \boldsymbol{\psi}_{\mathrm{dq}}(\boldsymbol{i}_{\mathrm{dq,lin}}) + \boldsymbol{L}_{\mathrm{dq},\Delta}(\boldsymbol{i}_{\mathrm{dq,lin}})(\boldsymbol{i}_{\mathrm{dq}} - \boldsymbol{i}_{\mathrm{dq,lin}}) \tag{3.2}$$

with flux linkage and differential inductance LUTs around the linearization current $\boldsymbol{i}_{\mathrm{dq,lin}}$ and a subsequent analytical calculation of the optimal operating point $\boldsymbol{i}_{\mathrm{dq}}^*$ as described in the previous paragraph for linearly magnetized SMs. After one iteration, the linearization current $\boldsymbol{i}_{\mathrm{dq,lin}}$ for the next iteration is given by the optimal operating point $\boldsymbol{i}_{\mathrm{dq}}^*$ of the previous iteration:

$$\boldsymbol{i}_{\mathrm{dq,lin}} \leftarrow \boldsymbol{i}_{\mathrm{dq}}^* \tag{3.3}$$

A flowchart of the OPC method is shown in Fig. 3.2. Machine characteristic loci of the nonlinearly magnetized IPMSM, cf. App. A.2, approximated with quadrics (3.1) and linearized magnetization (3.2) as well as the resulting optimal operating point $\boldsymbol{i}_{\mathrm{dq}}^*$ for different numbers of iterations N_{opc} for an exemplary torque reference of $T^* = 100\,\mathrm{Nm}$ at a speed of $5350\,\mathrm{min}^{-1}$ is shown in Fig. 3.3. In Fig. 3.4, the reference current $\boldsymbol{i}_{\mathrm{dq}}^*$ and the corresponding torque $T(\boldsymbol{i}_{\mathrm{dq}}^*)$ are calculated as a function of the iteration number and compared to the operating point $\boldsymbol{i}_{\mathrm{dq}}^*$ with the shortest length that achieves the desired torque satisfying voltage and current limits which acts as reference solution. The operating point without additional damping is calculated by the OPC proposed in [11, 82] and converges to the reference solution, see Fig. 3.4. Due to the significant magnetic (cross-)saturation effects, the reference current is only slightly damped, i.e., an increased number of iterations is required to calculate $\boldsymbol{i}_{\mathrm{dq}}^*$. To increase the damping to reduce the number of iterations required, the update rule (3.3) is adjusted in this work:

$$\boldsymbol{i}_{\mathrm{dq,lin}} \leftarrow \boldsymbol{i}_{\mathrm{dq,lin}} + 0.8\left(\boldsymbol{i}_{\mathrm{dq}}^* - \boldsymbol{i}_{\mathrm{dq,lin}}\right). \tag{3.4}$$

This update rule reduces the step size of (3.3) to 80 % and, therefore, increases the damping of the reference current calculation, see Fig. 3.4. For the actual implementation, the OPC performs only one iteration to calculate the optimal operating point per controller cycle (sampling instant) to reduce computation time. As a result, the OPC requires few sampling instants for the reference current to converge to its steady-state value after a torque transient, cf. Fig. Fig. 3.4. It should be noted that this does not pose a problem because the OPC converges much faster than the subsequent closed-loop controller, see Fig. 4.14.

[1]The term maximum torque per ampere (MTPA) is more commonly used than MTPC for historical reasons. Since MTPA mixes physical quantities (torque) with SI units (amperes), the physically and formally more consistent abbreviation MTPC is used in this thesis for the sake of scientific correctness.

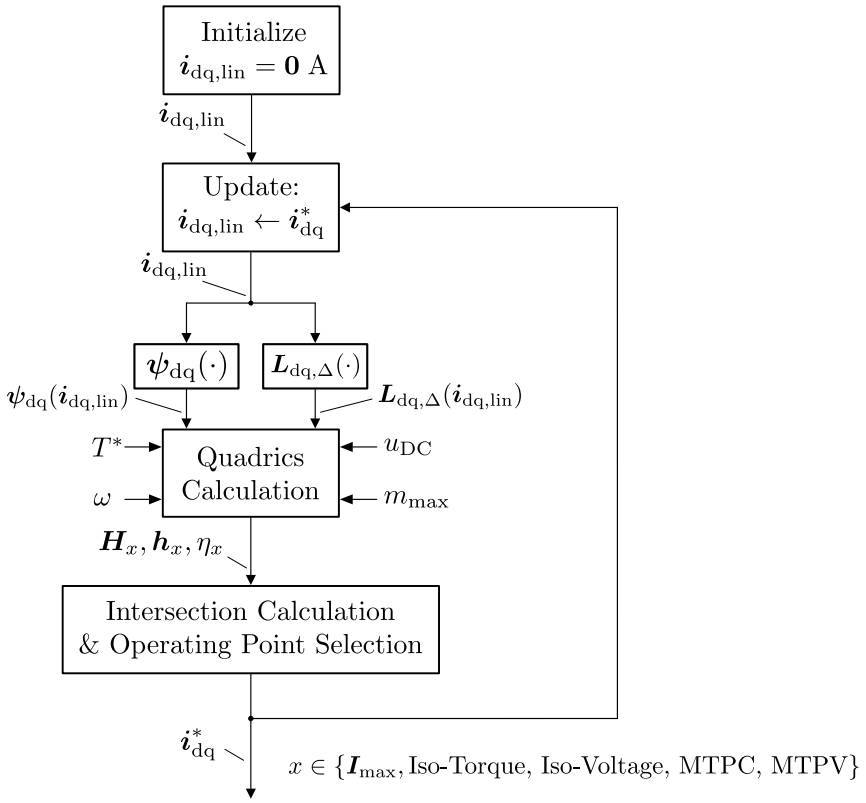

Fig. 3.2: Operating point controller scheme

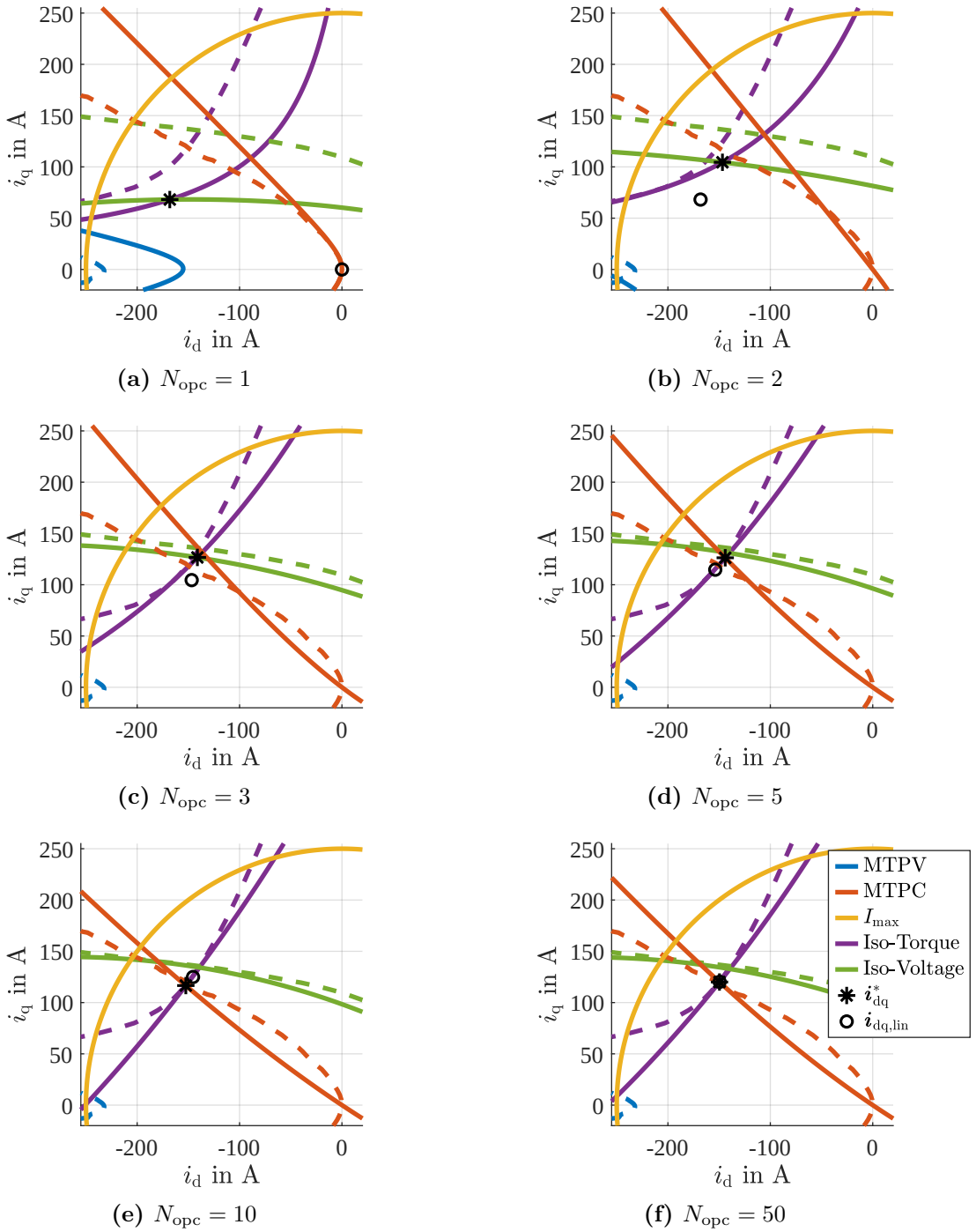

(a) $N_\mathrm{opc} = 1$ **(b)** $N_\mathrm{opc} = 2$

(c) $N_\mathrm{opc} = 3$ **(d)** $N_\mathrm{opc} = 5$

(e) $N_\mathrm{opc} = 10$ **(f)** $N_\mathrm{opc} = 50$

Fig. 3.3: Reference current $\boldsymbol{i}^*_\mathrm{dq}$, machine characteristic loci (dashed lines) of the nonlinearly magnetized IPMSM (cf. App. A.2), and analytically calculated loci (solid lines) based on linearized flux linkages around $\boldsymbol{i}_\mathrm{dq,lin}$ for different iterations N_opc with $T^* = 100\,\mathrm{Nm}$, $n_\mathrm{me} = 5350\,\mathrm{min}^{-1}$, $u_\mathrm{DC} = 360\,\mathrm{V}$, $m_\mathrm{max} = 1$

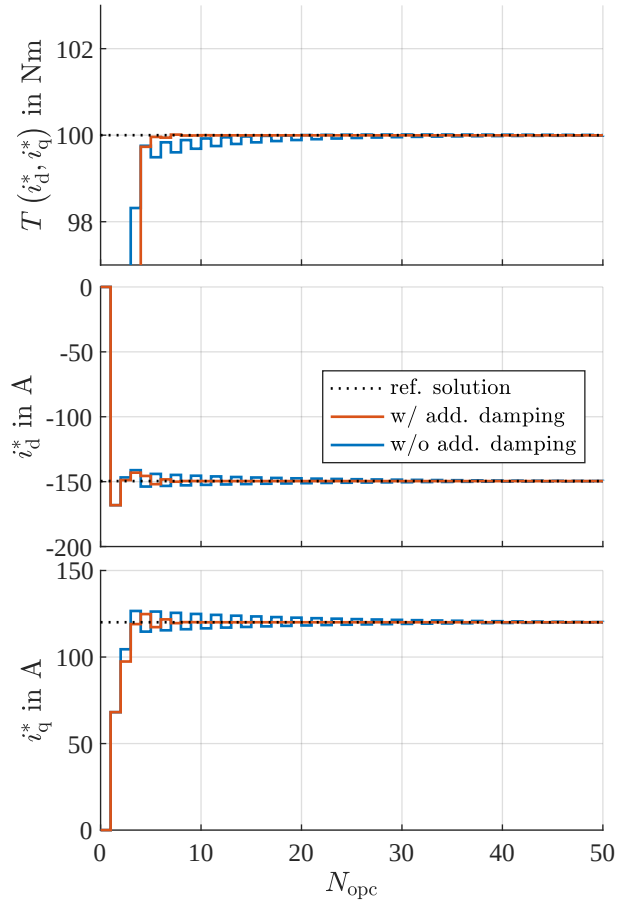

Fig. 3.4: Reference current $\boldsymbol{i}_\mathrm{dq}^*$ and corresponding torque $T(\boldsymbol{i}_\mathrm{dq}^*)$ with (cf. (3.4)) and without additional damping (cf. (3.3)) compared to the operating point $\boldsymbol{i}_\mathrm{dq}^*$ with the shortest length (reference solution) that achieves the desired torque ($T^* = 100\,\mathrm{Nm}$)

3.2 Continuous Control Set Model Predictive Flux Control

In this work, closed-loop flux linkage controllers in the stator-fixed frame are employed. As a state-of-the-art baseline, a conceptually simple CCS-MPFC with a one-step prediction horizon is applied to penalize the squared Euclidean distance from the predicted flux $\hat{\boldsymbol{\psi}}_{\alpha\beta}[k+1]$ to the reference flux at the next time step $\boldsymbol{\psi}_{\alpha\beta}^*[k+1]$. The optimization problem can thus be formulated as

$$\min_{\boldsymbol{u}_{\alpha\beta}[k]} J = \|\hat{\boldsymbol{\psi}}_{\alpha\beta}[k+1] - \boldsymbol{\psi}_{\alpha\beta}^*[k+1]\|^2 \tag{3.5a}$$

$$\text{s.t. } \hat{\boldsymbol{\psi}}_{\alpha\beta}[k+1] = \boldsymbol{A}_\psi \hat{\boldsymbol{\psi}}_{\alpha\beta}[k] + \boldsymbol{B}_\psi \boldsymbol{u}_{\alpha\beta}[k] + \boldsymbol{E}_\psi[k], \tag{3.5b}$$

$$\boldsymbol{\mathcal{A}}_\mathcal{U} \boldsymbol{u}_{\alpha\beta}[k] \leq \boldsymbol{b}_\mathcal{U}[k] \tag{3.5c}$$

with the hexagonal input constraints (3.5c) defined by

$$\boldsymbol{\mathcal{A}}_{\mathcal{U}} = \begin{bmatrix} \sqrt{3} & 1 \\ 0 & 1 \\ -\sqrt{3} & 1 \\ -\sqrt{3} & -1 \\ 0 & -1 \\ -\sqrt{3} & -1 \end{bmatrix} ; \; \boldsymbol{b}_{\mathcal{U}}[k] = \begin{bmatrix} 2 \\ 1 \\ 2 \\ 2 \\ 1 \\ 2 \end{bmatrix} \frac{u_{\mathrm{DC}}[k]}{\sqrt{3}} \tag{3.6}$$

and the discrete-time flux linkage difference equation (2.5) as prediction model (3.5b). The quadratic problem (QP) with linear inequality and equality constraints (3.5) can be reduced to a QP without equality constraints by inserting (3.5b) into (3.5a):

$$\min_{\boldsymbol{u}_{\alpha\beta}[k]} \boldsymbol{u}_{\alpha\beta}[k]^{\intercal} \boldsymbol{u}_{\alpha\beta}[k] T_{\mathrm{s}}^2 - 2T_{\mathrm{s}} \boldsymbol{u}_{\alpha\beta}[k]^{\intercal} \left(T_{\mathrm{s}} R_{\mathrm{s}} \boldsymbol{i}_{\alpha\beta}[k] + \hat{\boldsymbol{\psi}}_{\alpha\beta}[k] - \boldsymbol{\psi}^*_{\alpha\beta}[k+1] \right) \tag{3.7a}$$

$$\text{s.t. } \boldsymbol{\mathcal{A}}_{\mathcal{U}} \boldsymbol{u}_{\alpha\beta}[k] \leq \boldsymbol{b}_{\mathcal{U}}[k]. \tag{3.7b}$$

Since it is not the value of the cost function J that is of interest to be optimized but the variable $\boldsymbol{u}_{\alpha\beta}$, the constant part of J in (3.5), which is independent of $\boldsymbol{u}_{\alpha\beta}$ and, therefore, has no influence on the optimal choice of $\boldsymbol{u}_{\alpha\beta}$, is omitted in (3.7). Due to the one-step prediction horizon without penalizing the control input $\boldsymbol{u}_{\alpha\beta}$, the unconstrained solution of (3.5) corresponds to the DBFC law:

$$\boldsymbol{u}_{\alpha\beta,\mathrm{unc}}[k] = \frac{\boldsymbol{\psi}^*_{\alpha\beta}[k+1] - \hat{\boldsymbol{\psi}}_{\alpha\beta}[k]}{T_{\mathrm{s}}} + R_{\mathrm{s}} \boldsymbol{i}_{\alpha\beta}[k]. \tag{3.8}$$

Fig. 3.5 shows exemplary isocost loci of J with the voltage hexagon as input constraints, the unconstrained solution $\boldsymbol{u}_{\alpha\beta,\mathrm{unc}}$, and the constrained solution $\boldsymbol{u}_{\alpha\beta,\mathrm{con}}$. Here, the unconstrained voltage is outside the feasible input space (voltage hexagon) and can therefore not be actuated. Instead, the optimal (constrained) solution $\boldsymbol{u}_{\alpha\beta,\mathrm{con}}$ lies at the boundaries of the input constraints. Because of the quadratic term $\boldsymbol{u}_{\alpha\beta}[k]^{\intercal} \boldsymbol{u}_{\alpha\beta}[k] T_{\mathrm{s}}^2$ in (3.7a), the isocost loci are of circular shape. Thus, the constrained solution $\boldsymbol{u}_{\alpha\beta,\mathrm{con}}$ corresponds to the feasible voltage with the shortest distance to the unconstrained DBFC solution $\boldsymbol{u}_{\alpha\beta,\mathrm{unc}}$. Therefore, the application of the CCS-MPFC (3.5) leads to identical optimal voltages and control behavior as the DBFC law (3.8) combined with the minimum distance error dynamic overmodulation scheme [83].

At first glance, it seems unreasonable to introduce the CCS-MPFC (3.5) because of the increased implementation time and computational demand compared to the conceptually simple DBFC combined with dynamic overmodulation scheme [83]. However, compared to the DBFC, the CCS-MPFC can be extended with torque and current limits, which can be implemented straightforwardly as state constraints. The corresponding extension will be discussed in Sec. 5.4 and, hence, the standard CCS-MPFC has been introduced without state constraints in this section.

Any standard QP solver can be used to solve the linearly constrained QP of the CCS-MPFC (3.5) as well as its extension with state constraints reported in Sec. 5.4. For the practical implementation, the embedded solver of the Matlab MPC toolbox [84] was chosen in this work. To compensate for the control delay due to the digital implementation, a one-step state prediction is applied before the QP solver is called.

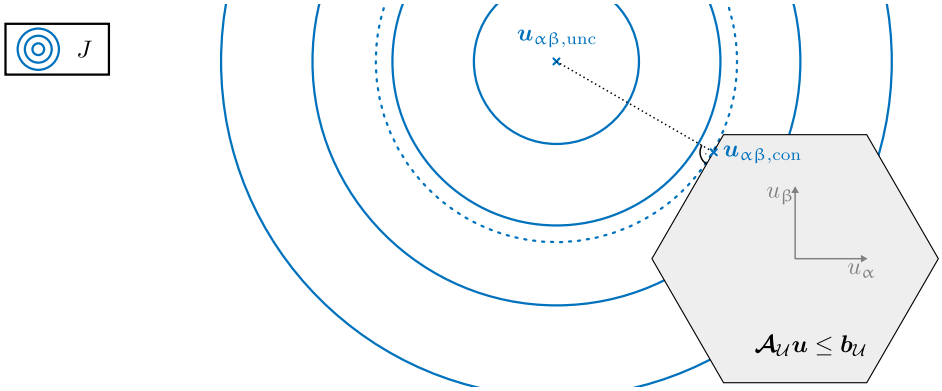

Fig. 3.5: Exemplary isocost loci and hexagonal input constraints (3.5c) with unconstrained $\boldsymbol{u}_{\alpha\beta,\mathrm{unc}}$ and constrained solution $\boldsymbol{u}_{\alpha\beta,\mathrm{con}}$ of the QP (3.5)

3.3 Gopinath-Style Flux Observer

The CCS-MPFC requires the value of the SM's instantaneous flux linkage $\boldsymbol{\psi}_{\alpha\beta}[k]$. To estimate the flux linkage, a Gopinath-style flux observer (GFO) is used [80, 81]. Here, the flux linkage estimate of a current model $\hat{\boldsymbol{\psi}}_{\alpha\beta,\mathrm{cm}}$ and the flux linkage estimate of a voltage model $\hat{\boldsymbol{\psi}}_{\alpha\beta,\mathrm{vm}}$ are fused with a PI element. A block diagram of the GFO with its tuning parameters K_p and T_r of the PI element is shown in Fig. 3.6. Due to the structure of the GFO, $\hat{\boldsymbol{\psi}}_{\alpha\beta,\mathrm{cm}}$ dominates at low frequencies and the voltage model estimate dominates at high frequencies.

Assuming $\hat{\boldsymbol{\psi}}_{\alpha\beta,\mathrm{cm}}$, $\hat{\boldsymbol{\psi}}_{\alpha\beta,\mathrm{vm}}$, and $\hat{\boldsymbol{\psi}}_{\alpha\beta}$ are available in continuous time, the GFO can be described by means of a transfer function with the Laplace transform variable λ. Instead of the unintuitive choice of the proportional gain K_p and the reset time T_r, the damping ratio D and the characteristic frequency ω_0 of the GFO can be used as tuning parameters. By choosing

$$T_\mathrm{r} = 2\frac{D}{\omega_0}, \tag{3.9}$$

$$K_\mathrm{p} = 2D\omega_0, \tag{3.10}$$

the transfer function from $\hat{\psi}_{\alpha,\mathrm{cm}}$ to $\hat{\psi}_\alpha$ and $\hat{\psi}_{\beta,\mathrm{cm}}$ to $\hat{\psi}_\beta$ evaluates to

$$G_\mathrm{CM}(\lambda) = \frac{\hat{\psi}_\alpha(\lambda)}{\hat{\psi}_{\alpha,\mathrm{cm}}(\lambda)} = \frac{\hat{\psi}_\beta(\lambda)}{\hat{\psi}_{\beta,\mathrm{cm}}(\lambda)} = \frac{2\frac{D}{\omega_0}\lambda + 1}{\frac{1}{\omega_0^2}\lambda^2 + 2\frac{D}{\omega_0}\lambda + 1} \tag{3.11}$$

and the transfer function from $\hat{\psi}_{\alpha,\mathrm{vm}}$ to $\hat{\psi}_\alpha$ and $\hat{\psi}_{\beta,\mathrm{vm}}$ to $\hat{\psi}_\beta$ is given by

$$G_\mathrm{VM}(\lambda) = \frac{\hat{\psi}_\alpha(\lambda)}{\hat{\psi}_{\alpha,\mathrm{vm}}(\lambda)} = \frac{\hat{\psi}_\beta(\lambda)}{\hat{\psi}_{\beta,\mathrm{vm}}(\lambda)} = \frac{\frac{1}{\omega_0^2}\lambda^2}{\frac{1}{\omega_0^2}\lambda^2 + 2\frac{D}{\omega_0}\lambda + 1}. \tag{3.12}$$

Both transfer functions (3.11) and (3.12) are shown in Fig. 3.7 for different damping ratios D. To ensure a dominant portion of the flux linkage estimate of the current model below ω_0 and a dominant voltage model above ω_0 without amplifications of (3.11) and (3.12) near the

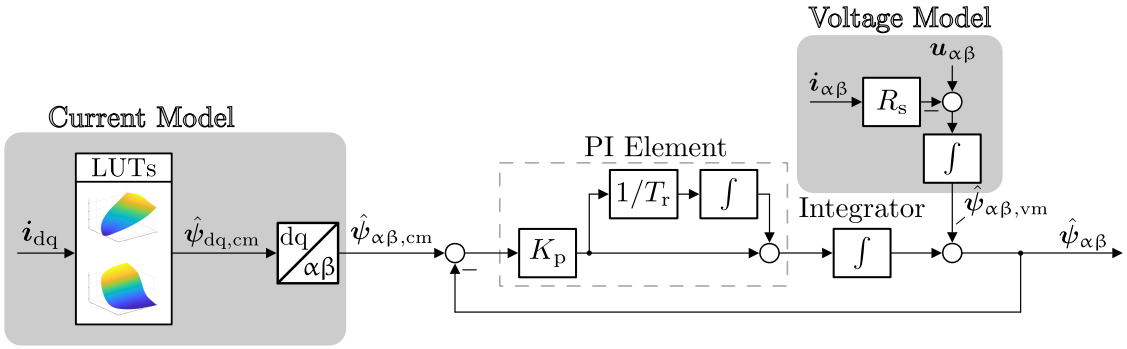

Fig. 3.6: Block diagram of the GFO (cf. [81])

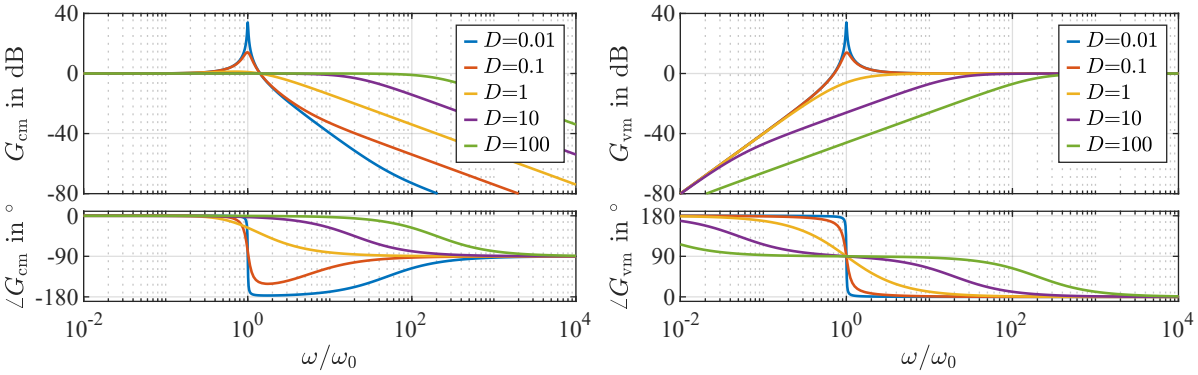

(a) Current model **(b)** Voltage model

Fig. 3.7: Bode plots of the transfer functions from the flux linkage estimate of the current and voltage model to the output of the GFO

characteristic frequency, a damping ratio of $D = 1$ is recommended. The characteristic frequency is usually set to values smaller than the rated frequency of the SM.

For the digital implementation of the GFO, however, it must be noted that $\hat{\boldsymbol{\psi}}_{\alpha\beta,\mathrm{cm}}$, $\hat{\boldsymbol{\psi}}_{\alpha\beta,\mathrm{cm}}$, and $\hat{\boldsymbol{\psi}}_{\alpha\beta}$ are sampled signals and, therefore, the GFO must be implemented in a discrete-time fashion, e.g., by mapping the block diagram of the GFO in Fig. 3.6 to its discrete-time equivalent.

3.4 Space Vector Modulation

Since the inverter can only realize discrete voltage values, i.e., seven different elementary vectors $\boldsymbol{u}_n$ (cf. Sec. 2.2), a modulation scheme must be applied that generates switching commands for the half bridges of the inverter in such a way that the resulting average voltage within a sampling period T_s represents the desired output voltage $\boldsymbol{u}_{\alpha\beta}$ of the controller, cf. Fig. 3.1. In this work, the SVM proposed in [79] is used which is summarized in the following.

A sequence of two linearly independent nonzero elementary voltage vectors, e.g., $\boldsymbol{u}_2$ and $\boldsymbol{u}_3$, and a zero elementary voltage vector $\boldsymbol{u}_1$ or $\boldsymbol{u}_8$ is sufficient to generate the desired mean voltage $\boldsymbol{u}_{\alpha\beta}$. To reduce the harmonic content of the applied voltage sequence, the two nonzero voltage vectors closest to the reference voltage are applied. Therefore, the nonzero vectors to be selected depend on the sector of the voltage hexagon in which the desired average voltage $\boldsymbol{u}_{\alpha\beta}$ is located. The calculation of the time durations t_n of the corresponding elementary vectors $\boldsymbol{u}_n$ is explained in the following using an exemplary mean voltage $\boldsymbol{u}_{\alpha\beta}$ located in sector 1, cf. Fig. 3.8. Here, the time durations $t_2[k]$ and $t_3[k]$ for the elementary vectors $\boldsymbol{u}_2$ and $\boldsymbol{u}_3$ must be chosen in such a way that the mean voltage of the applied sequence of elementary vectors corresponds to the desired voltage

$$\boldsymbol{u}_{\alpha\beta}[k] = \frac{1}{T_\mathrm{s}}(\boldsymbol{u}_2 t_2[k] + \boldsymbol{u}_3 t_3[k] + \underbrace{\boldsymbol{u}_1}_{=\boldsymbol{0}} t_1 + \underbrace{\boldsymbol{u}_8}_{=\boldsymbol{0}} t_8[k]) \tag{3.13}$$

considering the constraint

$$T_\mathrm{s} = \sum_{i=1,2,3,8} t_i[k] \text{ with } t_i[k] \geq 0. \tag{3.14}$$

By inserting $\boldsymbol{u}_2 = \left[\frac{2}{3} \quad 0\right]^\intercal u_\mathrm{DC}$ and $\boldsymbol{u}_3 = \left[\frac{1}{3} \quad \frac{1}{\sqrt{3}}\right]^\intercal u_\mathrm{DC}$ into the linear equation system (3.13), the time durations $t_2[k]$ and $t_3[k]$ become

$$\begin{bmatrix} t_2[k] \\ t_3[k] \end{bmatrix} = \frac{T_\mathrm{s}}{u_\mathrm{DC}} \begin{bmatrix} \frac{3}{2} & -\frac{\sqrt{3}}{2} \\ 0 & \sqrt{3} \end{bmatrix} \boldsymbol{u}_{\alpha\beta}[k]. \tag{3.15}$$

The time duration of the zero voltage vectors $t_1[k] + t_8[k]$ is calculated with (3.14) for given $t_2[k]$ and $t_3[k]$:

$$t_1[k] + t_8[k] = T_\mathrm{s} - (t_2[k] + t_3[k]). \tag{3.16}$$

The equations for calculating the time durations t_n of the elementary vectors for other voltage hexagon sectors are listed in Tab. 3.1. An efficient way to determine the sector for a given desired average voltage $\boldsymbol{u}_{\alpha\beta}$ is to compare the signs of u_β, $\sqrt{3}u_\alpha + u_\beta$, and $\sqrt{3}u_\alpha - u_\beta$ with the sector entries of Tab. 3.2.

The sequence (order) of voltage vectors as well as the splitting of the zero voltage vector time duration $t_1[k] + t_8[k]$ between $t_1[k]$ and $t_8[k]$ within the sampling period T_s introduce degrees of freedom that can be exploited to achieve reduced switching operations and harmonic current distortion. To minimize the number of switching operations, the sequence of elementary vectors must be arranged in such a way that only one inverter phase needs to be switched when the elementary vector changes. Due to this restriction, three different SVM pulse patterns, known as

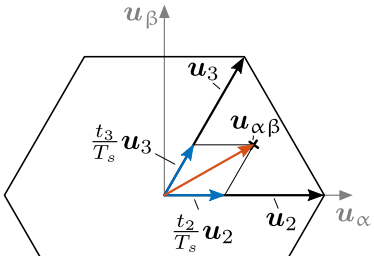

Fig. 3.8: Exemplary mean voltage $\boldsymbol{u}_{\alpha\beta}$ in voltage hexagon sector 1

Tab. 3.1: SVM time durations t_n of elementary vectors $\boldsymbol{u}_n$ for given mean voltage $\boldsymbol{u}_{\alpha\beta}$ [85]

Sector	Times for nonzero vectors	Times for zero vectors
1	$\begin{bmatrix} t_2 \\ t_3 \end{bmatrix} = \frac{T_\mathrm{s}}{u_\mathrm{DC}} \begin{bmatrix} \frac{3}{2} & -\frac{\sqrt{3}}{2} \\ 0 & \sqrt{3} \end{bmatrix} \boldsymbol{u}_{\alpha\beta}$	$t_1 + t_8 = T_\mathrm{s} - (t_2 + t_3)$
2	$\begin{bmatrix} t_3 \\ t_4 \end{bmatrix} = \frac{T_\mathrm{s}}{u_\mathrm{DC}} \begin{bmatrix} \frac{3}{2} & \frac{\sqrt{3}}{2} \\ -\frac{3}{2} & \frac{\sqrt{3}}{2} \end{bmatrix} \boldsymbol{u}_{\alpha\beta}$	$t_1 + t_8 = T_\mathrm{s} - (t_3 + t_4)$
3	$\begin{bmatrix} t_4 \\ t_5 \end{bmatrix} = \frac{T_\mathrm{s}}{u_\mathrm{DC}} \begin{bmatrix} -\frac{3}{2} & -\frac{\sqrt{3}}{2} \\ 0 & \sqrt{3} \end{bmatrix} \boldsymbol{u}_{\alpha\beta}$	$t_1 + t_8 = T_\mathrm{s} - (t_4 + t_5)$
4	$\begin{bmatrix} t_5 \\ t_6 \end{bmatrix} = \frac{T_\mathrm{s}}{u_\mathrm{DC}} \begin{bmatrix} -\frac{3}{2} & \frac{\sqrt{3}}{2} \\ 0 & -\sqrt{3} \end{bmatrix} \boldsymbol{u}_{\alpha\beta}$	$t_1 + t_8 = T_\mathrm{s} - (t_5 + t_6)$
5	$\begin{bmatrix} t_6 \\ t_7 \end{bmatrix} = \frac{T_\mathrm{s}}{u_\mathrm{DC}} \begin{bmatrix} \frac{3}{2} & -\frac{\sqrt{3}}{2} \\ -\frac{3}{2} & -\frac{\sqrt{3}}{2} \end{bmatrix} \boldsymbol{u}_{\alpha\beta}$	$t_1 + t_8 = T_\mathrm{s} - (t_6 + t_7)$
6	$\begin{bmatrix} t_7 \\ t_2 \end{bmatrix} = \frac{T_\mathrm{s}}{u_\mathrm{DC}} \begin{bmatrix} \frac{3}{2} & \frac{\sqrt{3}}{2} \\ 0 & -\sqrt{3} \end{bmatrix} \boldsymbol{u}_{\alpha\beta}$	$t_1 + t_8 = T_\mathrm{s} - (t_7 + t_2)$

type I, II, and III, can be realized. These three SVM pulse patterns are depicted in Fig. 3.9 for an exemplary voltage in sector 1. For all SVM types the sequence of elementary vectors alternates after each sampling period such that no switching occurs at the sampling instants. For SVM type II and III, only one of the zero voltage elementary vectors is selected during the sampling period. As a result, switching in one phase leg can be avoided. Compared to type II and type III, the type I switching pattern provides the additional degree of splitting the zero voltage vector time duration $t_1[k] + t_8[k]$ between $t_1[k]$ and $t_8[k]$. An exemplary voltage trajectory synthesized by the applied SVM type I scheme is shown in Fig. 3.10. Since only small improvements regarding the phase current distortion can be achieved by adjusting the proportions of $t_1[k]$ and $t_8[k]$ during online operation (cf. [86]), the zero vector pulse duration time is usually divided equally ($t_1 = t_8$) for SVM type I. Thus, SVM type I results in exactly the same pulse pattern as PWM with zero point shift and the application of the regular sampling principle [85].

For small modulation indices, SVM type I achieves lower harmonic current distortion than SVM type II and SVM type III for a given average switching frequency. However, as the modulation

Tab. 3.2: Determination of the voltage hexagon sector for given desired voltage $\boldsymbol{u}_{\alpha\beta}$ [85]

Sector	$\text{sign}(u_\beta)$	$\text{sign}(\sqrt{3}u_\alpha + u_\beta)$	$\text{sign}(\sqrt{3}u_\alpha - u_\beta)$
1	+	+	+
2	+	+	-
3	+	-	-
4	-	-	-
5	-	-	+
6	-	+	+

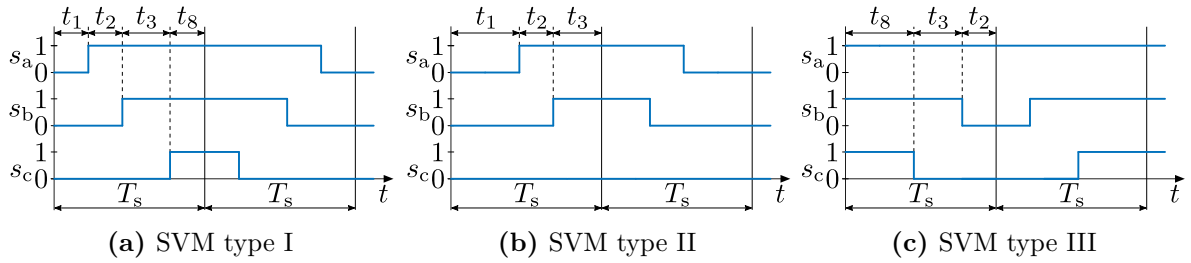

(a) SVM type I **(b)** SVM type II **(c)** SVM type III

Fig. 3.9: SVM pulse patterns in voltage hexagon sector 1

index increases, SVM type II and SVM type III are superior to SVM type I in terms of harmonic current distortion for a given average switching frequency. A detailed analysis of the different SVM types and the resulting current distortion can be found in [86]. In addition, an SVM method is proposed in [86] that adaptively selects the SVM type during online operation that produces the least harmonic current distortion within the next sampling period. Holtz and Beyer extended the method [86] in [87] with variable sampling periods $T_s[k]$. By appropriately varying the sampling period during a fundamental, optimal pulse patterns can be synthesized that result in minimal current distortion for a given average switching frequency.

Since the harmonic currents and voltages induced by the inverter due to its switching operation are not the scope of this thesis, the widely employed SVM type I is applied to generate the pulse patterns for the proposed control schemes. Nevertheless, the other SVM types and their extension [86] can be easily combined with the control algorithms presented in this work.

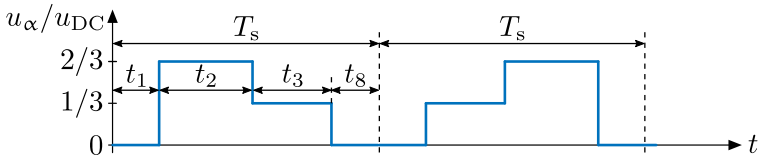

Fig. 3.10: Exemplary voltage trajectory u_α synthesized by the applied SVM type I scheme for a mean voltage $\boldsymbol{u}_{\alpha\beta}$ that is located in sector 1 of the voltage hexagon with pulse durations t_n for the corresponding vectors $\boldsymbol{u}_n$ and equally shared zero vector pulse duration ($t_1 = t_8$)

3.5 Interlocking Time Compensation

To prevent a hard short circuit in the inverter's phase legs, both transistors of a phase are not conducting for a short time (interlocking time T_i) after a switch in that phase leg is commanded by the SVM. This can cause differences (voltage errors) between the desired average voltages of the SVM and the resulting average voltages at the SM terminals. Discontinuous conduction mode is neglected in the following. The voltage error that occurs in one phase due to the interlocking time depends only on the switching operation in that phase leg and the phase current polarity. Therefore, the voltage error of one phase leg is independent of the other phases. For this reason, the cause of the voltage errors is explained with the help of an inductive load fed by a half bridge, see Fig. 3.11. Here $s(t) \in \{0, 1\}$ is the switching command of a pulse width modulator, while a switching operation from the lower DC-link potential ($s = 0$) to the upper DC-link potential ($s = 1$) is denoted by $\uparrow s$. The opposite switching from $s = 1$ to $s = 0$ is denoted by $\downarrow s$. During the interlocking time, the current i flows through one of the two diodes since both transistors are isolating. Depending on the sign of the current, the inductive load is connected to the upper or lower DC-link potential via the conducting diode. If the freewheeling diode is conducting and belongs to the transistor that will conduct after the switching operation, no voltage error will occur. This is the case for $\uparrow s \wedge i < 0$ and $\downarrow s \wedge i > 0$, see Fig. 3.11. For $\uparrow s \wedge i > 0$ the mean voltage is reduced and for $\downarrow s \wedge i < 0$ increased by $u_\mathrm{DC} T_\mathrm{i}/T_\mathrm{s}$ compared to the intended voltage.

In this work, the switching operation ($\uparrow s$ or $\downarrow s$) to be performed in the next sampling period as well as the sign of the current for each phase are compared with the 4 cases previously described, cf. Fig. 3.11. If the case $\uparrow s \wedge i > 0$ or $\downarrow s \wedge i > 0$ is detected in a phase, the time of the switching operation in this phase is performed earlier by T_i in order to compensate the voltage error.

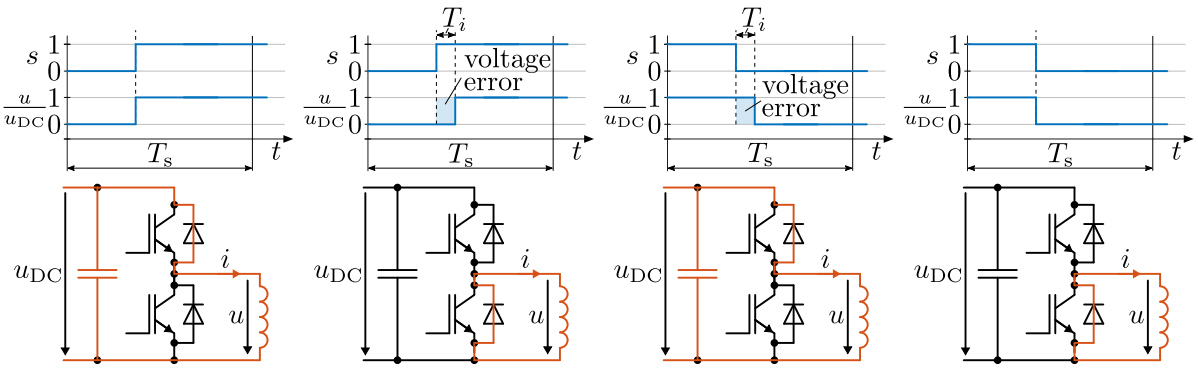

(a) $\uparrow s \wedge i < 0$ **(b)** $\uparrow s \wedge i > 0$ **(c)** $\downarrow s \wedge i < 0$ **(d)** $\downarrow s \wedge i > 0$

Fig. 3.11: Voltage error caused by the interlocking time as well as commutation paths during the interlocking time period for an inductive load fed by a half bridge

4 Extension to the Overmodulation Range

The following chapter is based on the own publications [5, 6, 8]. The author of this thesis contributed the main parts of [5, 6, 8], in particular, the proposed control method concepts as well as the simulative and experimental investigations. He also prepared the publications independently, while the contributions of the other co-authors were limited to technical discussions during the investigation phase as well as proofreading of the manuscripts. Therefore, parts of the following text have been taken in modified or unmodified form from the mentioned publications. For the sake of readability, the underlying self-citations are not explicitly listed in the following.

In this chapter the HRG, PC, and flux map correction (FMC) schemes are presented. The model-based HRG calculates the reference flux linkage that contains the harmonic component, which is induced by the voltage constraints of the feeding inverter (voltage hexagon) in the overmodulation range, and the PC scheme ensures the desired switching behavior of the inverter, e.g., six-step operation. This flux reference is calculated by solving an initial value problem (IVP) with voltage trajectories synthesized by Holtz's overmodulation scheme [39] for the desired modulation index, which is calculated based on a machine model and a given mean fundamental reference current[1] $\overline{\boldsymbol{i}_{\mathrm{dq}}^{*}}$ calculated by the OPC. The FMC is applied to correct the current-to-flux LUTs during online operation of the OPC, GFO, and HRG to compensate for flux linkage variations due to temperature [88], manufacturing deviations [89], and aging processes [90]. As a result of the proposed flux-based HRG, PC, and FMC, the following advantageous properties are achieved:

- The control scheme can seamlessly utilize the entire speed and modulation range, including six-step operation, without any control scheme reconfiguration.
- The presented flux-based HRG approach is conceptually simpler, more accurate, and significantly reduces the computational burden compared to the current-based HRG proposed in [5].
- Control and flux linkage estimation accuracy is improved by the FMC.

The integration of the presented HRG, PC, and FMC strategies into the baseline control scheme (see Fig. 3.1) is shown in Fig. 4.1.

[1] For Ch. 4 and Ch. 6, the reference current calculated by the OPC is denoted by $\overline{\boldsymbol{i}_{\mathrm{dq}}^{*}}$ instead of $\boldsymbol{i}_{\mathrm{dq}}^{*}$ to indicate that this current contains no harmonic component compared to the quantities $\boldsymbol{\psi}_{\alpha\beta}^{*}$ and $\boldsymbol{u}_{\alpha\beta}^{*}$ calculated by the HRG in the overmodulation range.

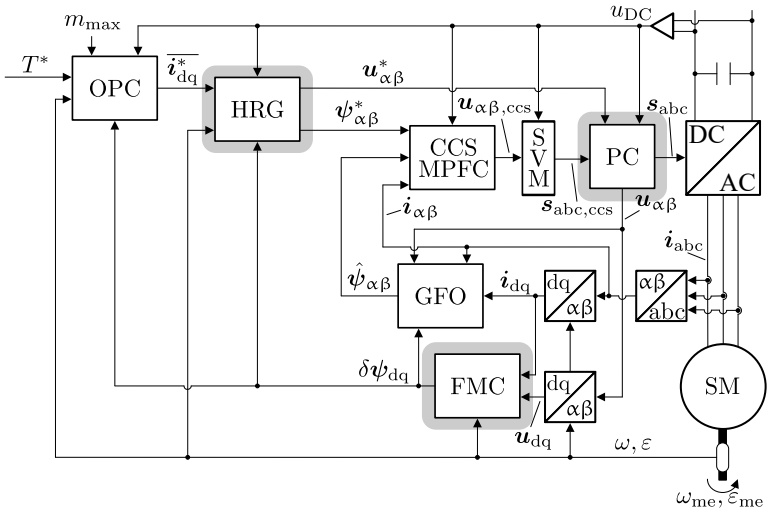

Fig. 4.1: Control scheme (gray shaded part is focused within Ch. 4) [6, derivate of Fig. 2]

4.1 Flux Linkage Map Correction

Static current-to-flux LUTs are employed for the OPC (cf. Sec. 3.1), the GFO (cf. Sec. 3.3), and for calculating the reference flux $\boldsymbol{\psi}^*_{\mathrm{dq}}(\overline{\boldsymbol{i}^*_{\mathrm{dq}}})$ (cf. Fig. 3.1). These static LUTs are identified offline and suffer from the fact that they cannot represent unseen operating conditions of the drive. As a result, the flux linkage estimated by the static LUTs may be inaccurate. Reasons for these errors are aging processes [90], dynamic temperature variations [88] as well as manufacturing deviations [89].

For the open-loop OPC, a flux linkage estimation error introduced by static flux linkage LUTs leads to a biased estimation of the machine characteristic loci (MTPC, MTPV, iso-torque, and iso-voltage) and, therefore, an unsatisfactory operating point $\overline{\boldsymbol{i}^*_{\mathrm{dq}}}$ is calculated. Especially during steady-state operation at the voltage limit, it is essential to estimate the iso-voltage loci accurately to enable six-step operation without additional outer-loop voltage controllers.

For the closed-loop CCS-MPFC, distorted flux linkage LUTs introduce a steady-state current control error $\overline{\boldsymbol{i}^*_{\mathrm{dq}}} - \boldsymbol{i}_{\mathrm{dq}}$. At first glance, this sounds surprising, since assuming that the CCS-MPFC operates without steady-state flux control error, the error introduced by static current-to-flux LUTs for calculating the flux linkage reference based on $\overline{\boldsymbol{i}^*_{\mathrm{dq}}}$ compensates for the error introduced by estimating the instantaneous flux linkage $\hat{\boldsymbol{\psi}}_{\alpha\beta}$ with the GFO, which relies on the same flux linkage LUTs, cf. Sec. 3.3. However, only at standstill the flux linkage estimate of the SM is based solely on static flux linkage LUTs. For increasing speeds ω, the GFO decreases the contribution of the static current model (flux linkage LUTs) and increases the contribution of a voltage model on the flux linkage estimate, cf. Sec. 3.3. Therefore, an increased steady-state current control error is introduced at speeds where the voltage model dominates the flux linkage estimate, i.e., $\omega \geq \omega_0$, because the current-to-flux mapping differs for the reference and control variable.

To overcome the disadvantages of a static current-to-flux mapping described in the previous paragraphs for the open-loop OPC, GFO, and the reference flux linkage calculation for the

closed-loop CCS-MPFC, an flux linkage portion $\delta\boldsymbol{\psi}_{\mathrm{dq}}$ is added to the flux linkage estimate of the static LUTs that is adjusted during online operation, see Fig. 4.2.

(a) Without correction **(b)** With correction

Fig. 4.2: Current-to-flux mapping with and without flux linkage map correction

The block diagram of the proposed FMC for calculating the correction flux $\delta\boldsymbol{\psi}_{\mathrm{dq}}$ is shown in Fig. 4.3. Here, the flux correction

$$\delta\boldsymbol{\psi}_{\mathrm{dq}}[k] = \mathrm{LPF}\left(\hat{\boldsymbol{\psi}}_{\mathrm{dq}}[k] - \hat{\boldsymbol{\psi}}_{\mathrm{dq,cm}}[k]\right) \tag{4.1}$$

corresponds to the difference between the flux linkage estimate of the static LUTs (current model) $\hat{\boldsymbol{\psi}}_{\mathrm{dq,cm}}$ and an online flux linkage estimate

$$\hat{\boldsymbol{\psi}}_{\mathrm{dq}}[k] = \left(\boldsymbol{T}_{\alpha\beta\mathrm{dq}}(-T_{\mathrm{s}}\omega[k]) - \boldsymbol{I}_2\right)^{-1}\left(\hat{\boldsymbol{L}}_{\mathrm{dq},\Delta}[k]\Delta\boldsymbol{i}_{\mathrm{dq}}[k] + R_{\mathrm{s}}T_{\mathrm{s}}\boldsymbol{i}_{\mathrm{dq}}[k] - \boldsymbol{T}_{\alpha\beta\mathrm{dq}}(-T_{\mathrm{s}}\omega[k])T_{\mathrm{s}}\boldsymbol{u}_{\mathrm{dq}}[k]\right) \tag{4.2}$$

filtered by a standard first-order low-pass filter (LPF) with a time constant τ as tuning parameter to reduce the high-frequency noise content and to provide a smoothed value of $\delta\boldsymbol{\psi}_{\mathrm{dq}}$. The estimate (4.2) corresponds to the discrete-time current difference equation (2.11) solved for $\boldsymbol{\psi}_{\mathrm{dq}}$. The commonly applied continuous-time equivalent of (4.2) is given by

$$\hat{\boldsymbol{\psi}}_{\mathrm{dq}}(t) = \begin{bmatrix} 0 & 1 \\ -1 & 0 \end{bmatrix} \frac{\boldsymbol{u}_{\mathrm{dq}}(t) - R_{\mathrm{s}}\boldsymbol{i}_{\mathrm{dq}}(t) - \hat{\boldsymbol{L}}_{\mathrm{dq},\Delta}(\boldsymbol{i}_{\mathrm{dq}}(t))\frac{\mathrm{d}\boldsymbol{i}_{\mathrm{dq}}(t)}{\mathrm{d}t}}{\omega(t)}. \tag{4.3}$$

However, (4.2) is applied in this work to estimate $\hat{\boldsymbol{\psi}}_{\mathrm{dq}}$ for the calculation of $\delta\boldsymbol{\psi}_{\mathrm{dq}}$, instead of using the more common discretized version of (4.3) by approximating $\mathrm{d}\boldsymbol{i}_{\mathrm{dq}}(t)/\mathrm{d}t \approx \left(\boldsymbol{i}_{\mathrm{dq}}[k+1] - \boldsymbol{i}_{\mathrm{dq}}[k]\right)/T_{\mathrm{s}}$. The reason for this is that the discretized version of (4.3) does not take into account the rotation of the dq frame against the αβ frame during one sampling period, and thus would introduce estimation errors that increase as the ratio of speed ω to sampling frequency $\frac{1}{T_{\mathrm{s}}}$ increases [65].

Since (4.2) identifies the magnetization based on the applied voltages $\boldsymbol{u}_{\mathrm{dq}}$ and currents $\boldsymbol{i}_{\mathrm{dq}}$, effects not modeled by static flux linkage LUTs, such as temperature variations, aging, and manufacturing deviations, are considered by the proposed FMC. However, the estimate (4.2) also depends on machine parameters: During stationary operation, i.e., $\Delta\boldsymbol{i}_{\mathrm{dq}} = 0\,\mathrm{A}$, the ohmic stator resistance, which is small and often neglected especially for high-power drives, is the only machine parameter affecting the estimate $\hat{\boldsymbol{\psi}}_{\mathrm{dq}}$. The differential inductances $\hat{\boldsymbol{L}}_{\mathrm{dq},\Delta}(\boldsymbol{i}_{\mathrm{dq}})$ are only required during transient operation to account for the voltage drop due to a change in the current $\Delta\boldsymbol{i}_{\mathrm{dq}}$. Therefore, the sensitivity of the estimate (4.2) to machine parameter variations can be considered as low.

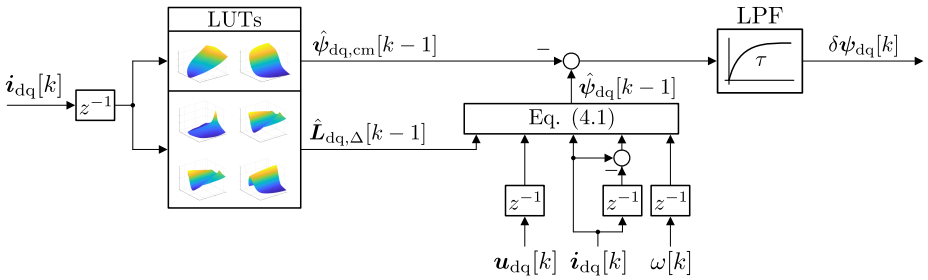

Fig. 4.3: Flux linkage map correction scheme

Since the estimation of (4.2) is based on the induced voltages, it is not possible to estimate the flux linkage via (4.2) at standstill. Even at low speeds near standstill, it is reasonable to disable the update of the correction $\delta\boldsymbol{\psi}_{\mathrm{dq}}$ because at low speeds the flux linkage estimation is sensitive to parasitic effects and variations in the ohmic stator resistance [91]. Therefore, a speed threshold ω_{fmc} is introduced as an additional tuning parameter. For absolute speeds below this threshold, i.e., $|\omega| < \omega_{\mathrm{fmc}}$, the update of $\delta\boldsymbol{\psi}_{\mathrm{dq}}$ is paused.

To demonstrate the advantages of the proposed FMC, the steady-state current control accuracy was experimentally investigated with and without compensation for errors introduced by static flux linkage LUTs. The experimental setup regarding the applied nonlinearly magnetized IPMSM and the testbench is described in App. A.2 and App. B. For the experiment, 80 equispaced reference currents $\overline{\boldsymbol{i}^*_{\mathrm{dq}}}$ (operating points) covering the left i_{d}-i_{q} half-plane were commanded directly to the closed-loop controller without the open-loop OPC at standstill and at a speed of $n_{\mathrm{me}} = 3000\,\mathrm{min}^{-1}$. The block diagram of the control scheme for the experimental investigation of the FMC is depicted in Fig. 4.4. Here, the static flux linkage LUTs of the GFO and the reference flux calculation are corrected by the FMC with $\delta\boldsymbol{\psi}_{\mathrm{dq}}$. The parameters of the GFO and the FMC are listed in Tab. 4.1.

Fig. 4.5 shows the length of the current control error $\|\boldsymbol{i}^*_{\mathrm{dq}} - \overline{\boldsymbol{i}_{\mathrm{dq}}}\|$ with and without FMC for a speed of $n_{\mathrm{me}} = 3000\,\mathrm{min}^{-1}$. Since this speed is above the characteristic frequency ω_0 of the GFO, the voltage model dominates the estimation of the instantaneous flux linkage of the SM and, therefore, different current-to-flux mappings are used for the reference and control variables, resulting in significant steady-state current control errors, see Fig. 4.5a. Activating the FMC significantly reduces the current control error, cf. Fig. 4.5b. To obtain a scalar metric of the steady-state current control accuracy, the effective values $\mathrm{RMS}(\|\boldsymbol{i}^*_{\mathrm{dq}} - \overline{\boldsymbol{i}_{\mathrm{dq}}}\|)$ over the left i_{d}-i_{q} half-plane are calculated and given in Tab. 4.2. For speeds below the speed threshold ω_{fmc}, the FMC is deactivated. However, accurate steady-state current control accuracy is achieved because the current-to-flux linkage mappings for control and reference variable rely on the same static flux linkage LUTs. Compared to the maximum current of 250 A of the test IPMSM, the remaining steady-state current control error for the CCS-MPFC and GFO equipped with the FMC can be considered as minor or negligible.

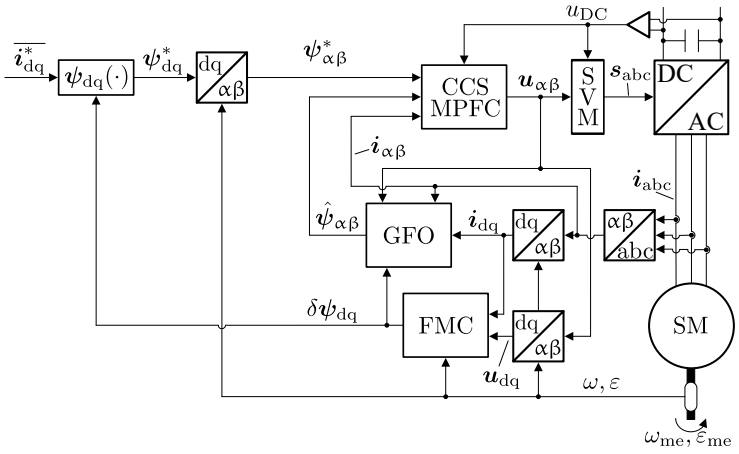

Fig. 4.4: Control scheme of the experimental current control accuracy investigation of Sec. 4.1

Tab. 4.1: GFO and FMC parameters

GFO		
Damping ratio	D	1
Characteristic frequency	ω_0	$675\,\mathrm{s}^{-1}$
FMC		
Low-pass filter time constant	τ	20 ms
Speed threshold	ω_{fmc}	$270\,\mathrm{s}^{-1}$

Tab. 4.2: Steady-state current control accuracy comparison

FMC	n_{me} in min^{-1}	RMS($\|\boldsymbol{i}^*_{\mathrm{dq}} - \overline{\boldsymbol{i}_{\mathrm{dq}}}\|$) in A
✗	0	0.4
✗	3000	8.1
✓	3000	0.3

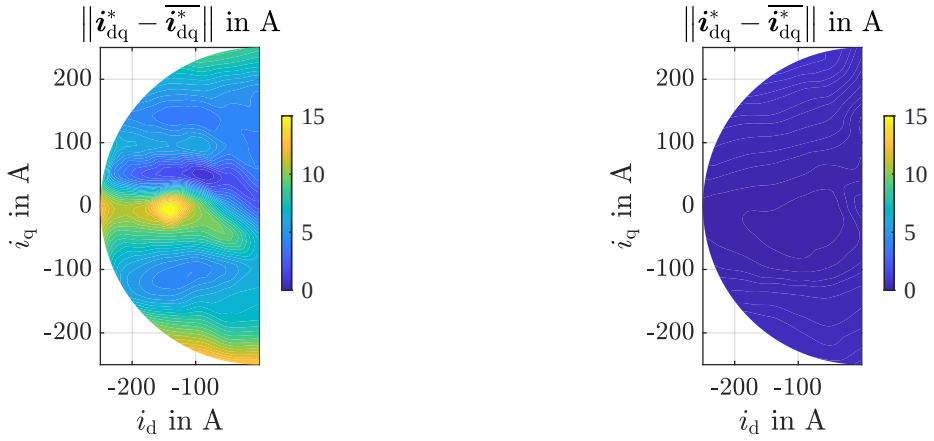

(a) Without FMC **(b)** With FMC

Fig. 4.5: Experimental current control accuracy investigation with and without flux linkage map correction scheme at $n_{\mathrm{me}} = 3000\,\mathrm{min}^{-1}$

4.2 Harmonic Reference Generator

In the overmodulation range, inevitable current and flux harmonics induced by the voltage constraints, i.e., voltage hexagon, deteriorate the performance of closed-loop drive controllers, e.g., PI-FOC, CCS-MPFC, etc., see [5, Fig. 17 and Fig. 18]. To prevent this performance degradation during steady-state operation, the HRG calculates these flux harmonics using a machine model and voltage trajectories. These calculated flux harmonics are added to the mean reference flux $\overline{\boldsymbol{\psi}^*_{\mathrm{dq}}}\left(\overline{\boldsymbol{i}^*_{\mathrm{dq}}}\right)$. Therefore, assuming an accurate machine model to calculate the flux harmonics, the harmonic content of the flux during steady-state operation in the overmodulation range is included in both the reference flux and the actual flux of the SM. This results in a vanishing steady-state control error without a harmonic component. Consequently, the controller is no longer degraded in the overmodulation range by applying the HRG. A simplified block diagram of an HRG is depicted in Fig. 4.6 applied to a general control system for steady-state control conditions to illustrate the concept.

The calculation steps and methodology of the HRG are described in more detail in the following for the general case of a nonlinearly magnetized SM with significant (cross-)saturation. A flowchart of the HRG algorithm is shown in Fig. 4.7.

4.2.1 Modulation Index Calculation

The flux linkage reference $\boldsymbol{\psi}^*_{\alpha\beta}$ of the HRG in the overmodulation range depends on the rotor angle ε, the modulation index m, and the mean current reference $\overline{\boldsymbol{i}^*_{\mathrm{dq}}}$ given by the OPC. To compute the modulation index, the required mean voltage $\overline{\boldsymbol{u}_{\mathrm{dq}}}$ must be calculated:

$$\overline{\boldsymbol{u}_{\mathrm{dq}}}[k] = R_{\mathrm{s}}\overline{\boldsymbol{i}^*_{\mathrm{dq}}}[k] + \frac{\boldsymbol{T}_{\alpha\beta\mathrm{dq}}(T_{\mathrm{s}}\omega[k]) - \boldsymbol{I}_2}{T_{\mathrm{s}}}\overline{\boldsymbol{\psi}^*_{\mathrm{dq}}}[k]. \tag{4.4}$$

Here, (4.4) corresponds to the current difference equation (2.11) assuming stationary operation and the mean flux linkage reference $\overline{\boldsymbol{\psi}^*_{\mathrm{dq}}}(\overline{\boldsymbol{i}^*_{\mathrm{dq}}})$ is given by current-to-flux LUTs with $\overline{\boldsymbol{i}^*_{\mathrm{dq}}}$ as input. Then, the modulation index evaluates to

$$m[k] = \frac{\|\overline{\boldsymbol{u}_{\mathrm{dq}}}[k]\|}{\frac{2}{\pi}u_{\mathrm{DC}}[k]}. \tag{4.5}$$

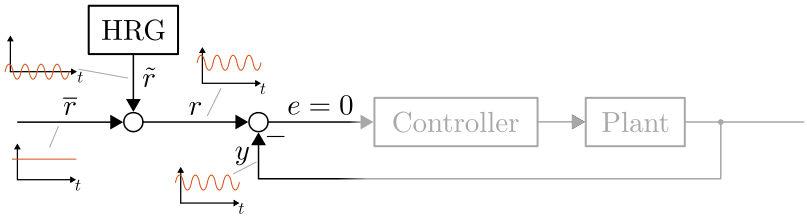

Fig. 4.6: Simplified HRG conceptual scheme applied to a general closed-loop control system with the mean reference $\overline{r}$, harmonic content of the reference $\tilde{r}$, reference r, system output y, and control error e [6, Fig. 4]

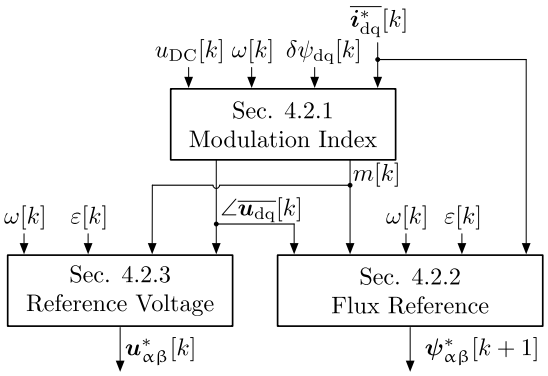

Fig. 4.7: Flowchart of the HRG [6, derivate of Fig. 5]

4.2.2 Flux Linkage Reference

If the modulation index is in the linear modulation range $\|\overline{\boldsymbol{u}_{\mathrm{dq}}}\| \leq u_{\mathrm{DC}}/\sqrt{3}$, no further calculations have to be performed by the HRG and the flux linkage reference for the CCS-MPFC is set to

$$\boldsymbol{\psi}^*_{\alpha\beta}[k+1] = \boldsymbol{T}_{\alpha\beta\mathrm{dq}}(\varepsilon[k] + T_{\mathrm{s}}\omega[k])\overline{\boldsymbol{\psi}^*_{\mathrm{dq}}}[k]. \tag{4.6}$$

However, when the modulation index is in the overmodulation range, the HRG must calculate the flux linkage reference, using voltage trajectories generated by an overmodulation scheme. In this work, the overmodulation scheme proposed in [39] and summarized in Sec. 2.4 is utilized to generate voltage trajectories as a function of the modulation index. In Fig. 2.9, the voltage values are shown as a function of the modulation index m and the angle of the fundamental voltage

$$\angle\boldsymbol{u}_{\alpha\beta,\mathrm{f}}[k] = \varepsilon[k] + \angle\overline{\boldsymbol{u}_{\mathrm{dq}}}[k]. \tag{4.7}$$

The flux linkage reference is calculated by applying Faraday's law of induction

$$\boldsymbol{\psi}^*_{\alpha\beta}(t) = \int_0^t \boldsymbol{u}_{\alpha\beta}(\tilde{t})\mathrm{d}\tilde{t} + C. \tag{4.8}$$

Here, the integration constant C must be chosen such that the mean value of the flux linkage reference vanishes for one electrical revolution. In addition, the ohmic voltage drop is neglected and later taken into account by scaling and rotating the flux reference. By substituting the integration variable of (4.8)

$$\mathrm{d}\tilde{t} = \frac{\mathrm{d}\tilde{\varepsilon}}{\omega}, \tag{4.9}$$

the flux linkage reference with omitted ohmic stator resistance can be calculated:

$$\boldsymbol{\psi}^*_{\alpha\beta}(\varepsilon[k]) = \frac{1}{\omega[k]} \int_0^{\angle\boldsymbol{u}_{\alpha\beta,\mathrm{f}}[k]} \boldsymbol{u}_{\alpha\beta}(\tilde{\varepsilon}, m[k])\mathrm{d}\tilde{\varepsilon} \underbrace{- \frac{0.5}{\omega[k]} \int_0^{\pi} \boldsymbol{u}_{\alpha\beta}(\tilde{\varepsilon}, m[k])\mathrm{d}\tilde{\varepsilon}}_{C}. \tag{4.10}$$

An illustration of (4.10) is shown in Fig. 4.8. For the actual implementation, the integral terms of (4.10) are stored as two-dimensional LUTs with the upper integration limit $\angle\boldsymbol{u}_{\alpha\beta,\mathrm{f}}$ and the

modulation index m as inputs, cf. Fig. 4.9. Additionally, the symmetry of the voltage hexagon can be exploited such that the integral terms of the voltage trajectories only need to be stored for one hexagon sector to further reduce the computational load. This implementation is described in more detail in [6].

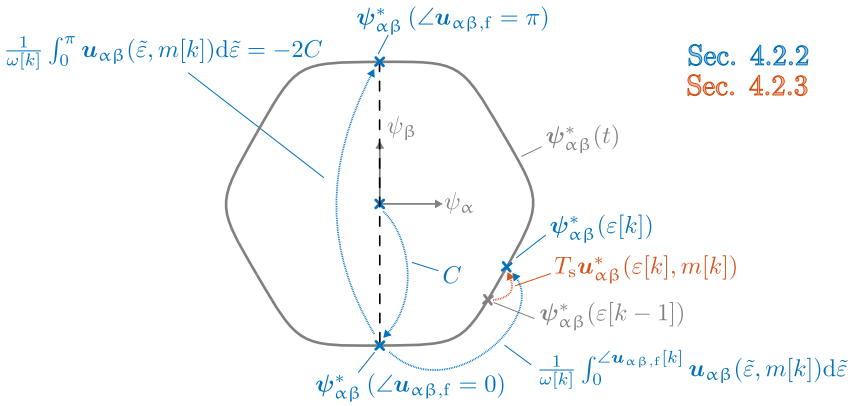

Fig. 4.8: Illustration of the HRG method for calculating the flux linkage reference $\boldsymbol{\psi}^*_{\alpha\beta}$ [8, derivate of Fig. 8]

The ohmic voltage drop of the stator resistance is incorporated by scaling and rotating the flux linkage reference (4.10) calculated with a neglected ohmic voltage drop:

$$\boldsymbol{\psi}^*_{\alpha\beta}(\varepsilon[k]) \leftarrow \underbrace{\boldsymbol{T}_{\alpha\beta\mathrm{dq}}\left(\angle(\overline{\boldsymbol{u}_{\mathrm{dq}}}[k] - R_\mathrm{s}\overline{\boldsymbol{i}^*_{\mathrm{dq}}}[k]) - \angle\overline{\boldsymbol{u}_{\mathrm{dq}}}[k]\right)}_{\text{Rotation}} \underbrace{\frac{\|\overline{\boldsymbol{u}_{\mathrm{dq}}}[k] - R_\mathrm{s}\overline{\boldsymbol{i}^*_{\mathrm{dq}}}[k]\|}{\|\overline{\boldsymbol{u}_{\mathrm{dq}}}[k]\|}}_{\text{Scaling}} \boldsymbol{\psi}^*_{\alpha\beta}(\varepsilon[k]). \tag{4.11}$$

This approach is motivated in the following by rewriting Faraday's induction law (2.4) with general voltages $\boldsymbol{u}$, currents $\boldsymbol{i}$, an ohmic resistance R, and flux linkages $\boldsymbol{\psi}$:

$$\begin{aligned}
&\frac{\mathrm{d}}{\mathrm{d}t}\boldsymbol{\psi}_{\alpha\beta} = \boldsymbol{u}_{\alpha\beta} - R\boldsymbol{i}_{\alpha\beta},\\
\Leftrightarrow\ &\frac{\mathrm{d}}{\mathrm{d}t}\boldsymbol{\psi}_{\alpha\beta} = \|\boldsymbol{u}_{\alpha\beta} - R\boldsymbol{i}_{\alpha\beta}\|\boldsymbol{T}_{\alpha\beta\mathrm{dq}}\left(\angle\left(\boldsymbol{u}_{\alpha\beta} - R\boldsymbol{i}_{\alpha\beta}\right)\right)\begin{bmatrix}1\\0\end{bmatrix},\\
\Leftrightarrow\ &\frac{\mathrm{d}}{\mathrm{d}t}\boldsymbol{\psi}_{\alpha\beta} = \|\boldsymbol{u}_{\alpha\beta} - R\boldsymbol{i}_{\alpha\beta}\|\boldsymbol{T}_{\alpha\beta\mathrm{dq}}\left(\angle\left(\boldsymbol{u}_{\alpha\beta} - R\boldsymbol{i}_{\alpha\beta}\right)\right)\underbrace{\frac{\boldsymbol{T}_{\alpha\beta\mathrm{dq}}\left(-\angle\boldsymbol{u}_{\alpha\beta}\right)\boldsymbol{u}_{\alpha\beta}}{\|\boldsymbol{u}_{\alpha\beta}\|}}_{\begin{bmatrix}1 & 0\end{bmatrix}^\intercal},\\
\Leftrightarrow\ &\frac{\mathrm{d}}{\mathrm{d}t}\boldsymbol{\psi}_{\alpha\beta} = \underbrace{\frac{\|\boldsymbol{u}_{\mathrm{dq}} - R\boldsymbol{i}_{\mathrm{dq}}\|}{\|\boldsymbol{u}_{\mathrm{dq}}\|}}_{\text{Scaling}}\underbrace{\boldsymbol{T}_{\alpha\beta\mathrm{dq}}\left(\angle\left(\boldsymbol{u}_{\mathrm{dq}} - R\boldsymbol{i}_{\mathrm{dq}}\right) - \angle\boldsymbol{u}_{\mathrm{dq}}\right)}_{\text{Rotation}}\underbrace{\frac{\mathrm{d}}{\mathrm{d}t}\boldsymbol{\psi}_{\alpha\beta,R=0}}_{\boldsymbol{u}_{\alpha\beta}}.
\end{aligned} \tag{4.12}$$

Here, $\boldsymbol{\psi}_{\alpha\beta,R=0}$ denotes a flux linkage for which $\frac{\mathrm{d}}{\mathrm{d}t}\boldsymbol{\psi}_{\alpha\beta,R=0} = \boldsymbol{u}_{\alpha\beta}$ holds, i.e., $R = 0\,\Omega$. To apply the scaling and rotating of $\frac{\mathrm{d}}{\mathrm{d}t}\boldsymbol{\psi}_{\alpha\beta,R=0}$ in the same way to the flux linkage

$$\boldsymbol{\psi}_{\alpha\beta} = \frac{\|\boldsymbol{u}_{\mathrm{dq}} - R\boldsymbol{i}_{\mathrm{dq}}\|}{\|\boldsymbol{u}_{\mathrm{dq}}\|}\boldsymbol{T}_{\alpha\beta\mathrm{dq}}\left(\angle(\boldsymbol{u}_{\mathrm{dq}} - R\boldsymbol{i}_{\mathrm{dq}}) - \angle\boldsymbol{u}_{\mathrm{dq}}\right)\boldsymbol{\psi}_{\alpha\beta,R=0}, \tag{4.13}$$

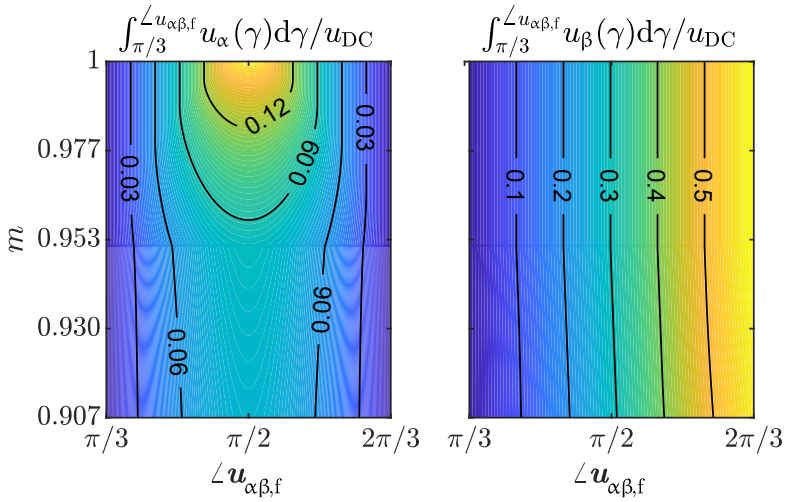

Fig. 4.9: Integral of the modulation index-dependent voltage trajectories of Fig. 2.9 over the angle of the fundamental voltage $\angle \boldsymbol{u}_{\alpha\beta,\mathrm{f}}$ for sector 2 of the voltage hexagon [6, Fig. 9]

the voltage $\boldsymbol{u}_{\mathrm{dq}}$ and the current $\boldsymbol{i}_{\mathrm{dq}}$ must be constant, i.e., $\boldsymbol{u}_{\alpha\beta}$ and $\boldsymbol{i}_{\alpha\beta}$ must be sinusoidal, such that the scaling and rotation appear as integration constants. Since the voltages $\boldsymbol{u}_{\alpha\beta}$ and currents $\boldsymbol{i}_{\alpha\beta}$ contain harmonic components in the overmodulation range, the method of scaling and rotating the flux linkage reference to account for the ohmic stator resistance is only an approximation. However, the ohmic voltage drop is minor compared to the induced voltages during steady-state operation in the overmodulation range. Therefore, the resulting error for the flux linkage calculation based on scaling and rotating the flux linkage reference to incorporate the ohmic voltage drop can be classified as small, cf. Sec. 4.2.4.

4.2.3 Voltage Reference

The reference voltage $\boldsymbol{u}^*_{\alpha\beta}$ required for the PC strategy corresponds to the mean voltage that would be actuated by the overmodulation scheme [39] during the next sampling instant. This reference voltage is given by

$$\begin{aligned}\boldsymbol{u}^*_{\alpha\beta}[k] &= \frac{1}{T_\mathrm{s}\omega[k]} \int_{\angle \boldsymbol{u}_{\alpha\beta,\mathrm{f}}[k]}^{\angle \boldsymbol{u}_{\alpha\beta,\mathrm{f}}[k+1]} \boldsymbol{u}_{\alpha\beta}(\gamma, m[k])\mathrm{d}\gamma \\ &= \frac{1}{T_\mathrm{s}\omega[k]} \left(\int_{0}^{\angle \boldsymbol{u}_{\alpha\beta,\mathrm{f}}[k+1]} \boldsymbol{u}_{\alpha\beta}(\gamma, m[k])\mathrm{d}\gamma - \int_{0}^{\angle \boldsymbol{u}_{\alpha\beta,\mathrm{f}}[k]} \boldsymbol{u}_{\alpha\beta}(\gamma, m[k])\mathrm{d}\gamma \right)\end{aligned} \tag{4.14}$$

and is calculated by using the two-dimensional LUTs shown in Fig. 4.9. Here, each LUT only needs to be evaluated twice to calculate $\boldsymbol{u}^*_{\alpha\beta}$.

4.2.4 Simulative Accuracy and Computation Time Investigation

In order to investigate the accuracy of the calculated reference trajectories and the computational load of the proposed HRG, simulative investigations are performed for a nonlinearly magnetized

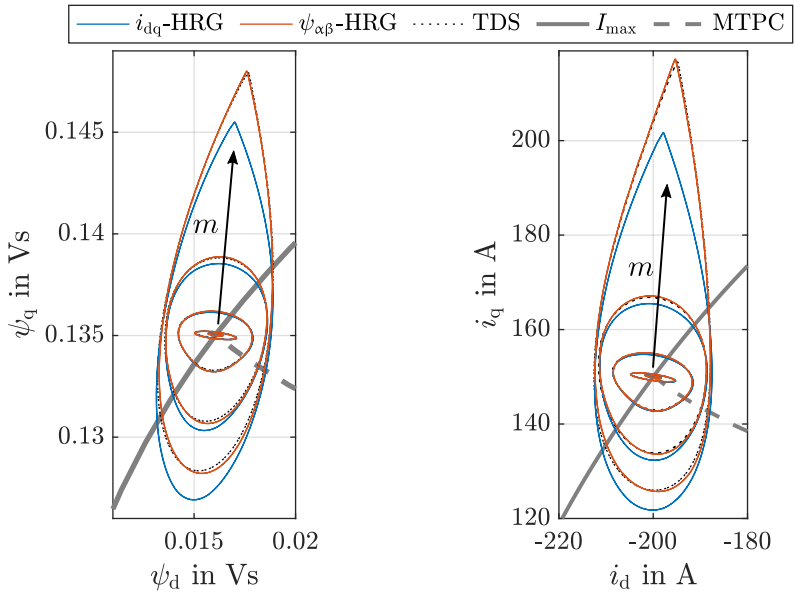

Fig. 4.10: Exemplary reference flux and current trajectories calculated by the proposed $\boldsymbol{\psi}_{\alpha\beta}$-HRG and the $\boldsymbol{i}_{dq}$-HRG [5] with $N_{bvp} = 9$ compared to a time-domain simulation (TDS) in the overmodulation range for different modulation indices [6, derivate of Fig. 12]

IPMSM, cf. App. A.2, and are shown in the following. The harmonic content of the flux reference can be visualized more clearly in the dq coordinate system, since its fundamental is constant. For this reason, the reference trajectory $\boldsymbol{\psi}^*_{\alpha\beta}$ is transformed to the dq coordinate system. Note that this transformation is only done for visualization and not for the actual implementation of the controller. Furthermore, the results are compared with the HRG presented in [5]. To avoid confusion, the HRG presented in this work is referred to in this section as $\boldsymbol{\psi}_{\alpha\beta}$-HRG, while the HRG of [5] is referred to as $\boldsymbol{i}_{dq}$-HRG. In [5], different variants of the $\boldsymbol{i}_{dq}$-HRG were presented. For the following comparisons, the most accurate $\boldsymbol{i}_{dq}$-HRG with the variable supporting point method and exact discretization is chosen. Compared to the $\boldsymbol{\psi}_{\alpha\beta}$-HRG, an additional tuning parameter N_{bvp} has to be chosen for the $\boldsymbol{i}_{dq}$-HRG. This tuning parameter corresponds to the number of supporting or grid points that are used to solve the BVP of the $\boldsymbol{i}_{dq}$-HRG.

To investigate the accuracy of the $\boldsymbol{\psi}_{\alpha\beta}$-HRG, the mean error

$$\overline{\|\boldsymbol{e}_{dq}\|} = \frac{3}{\pi} \int_0^{\pi/3} \sqrt{{e_d}^2(\varepsilon) + {e_q}^2(\varepsilon)} \mathrm{d}\varepsilon \tag{4.15}$$

is depicted in Fig. 4.11. Here, the error $\boldsymbol{e}_{dq}$ is defined as the difference between the current trajectory calculated by the corresponding HRG and the trajectory obtained by a time-domain simulation (TDS), see Fig. 4.10. For this simulative investigation, the current trajectory of the $\boldsymbol{\psi}_{\alpha\beta}$-HRG is determined with the help of flux linkage-to-current LUTs. The TDS solution is obtained by applying Holtz's overmodulation scheme [39] in an open-loop fashion with a sufficiently long simulation time such that the natural damping of the IPMSM leads to steady-state harmonic trajectories. Here, the resulting ODE of the quasi-continuous TDS was solved with the adaptive Runge-Kutta method ode45 [92]. Although the mean error $\boldsymbol{e}_{dq}$ of the $\boldsymbol{i}_{dq}$-HRG

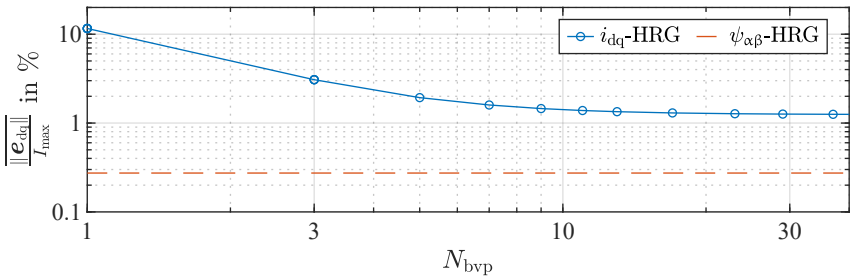

Fig. 4.11: Normalized mean error of the current trajectories for six-step operation calculated by the proposed $\boldsymbol{\psi}_{\alpha\beta}$-HRG and the $\boldsymbol{i}_{dq}$-HRG [5] for the rated operating point (cf. Fig. 4.10) [6, derivate of Fig. 11]

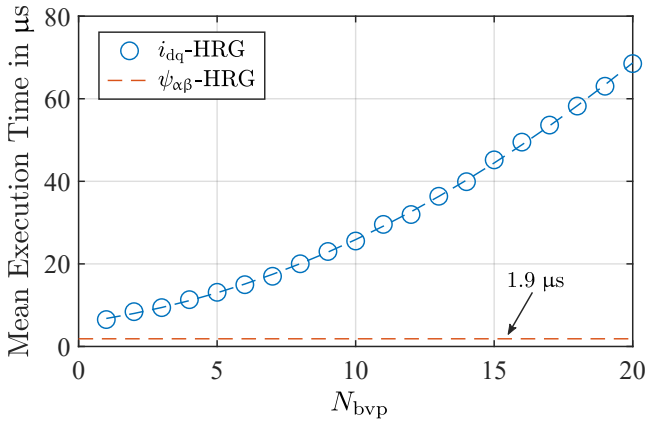

Fig. 4.12: Required execution times for the proposed $\boldsymbol{\psi}_{\alpha\beta}$-HRG and the $\boldsymbol{i}_{dq}$-HRG [5] utilizing a Lenovo T14s with an AMD Ryzen 7 1.9 GHz processor and 32 GB of RAM [6, Fig. 13]

decreases as the number of supporting points N_{bvp} increases [5], a significant mean error remains during six-step operation ($m = 1$) for the applied nonlinearly magnetized IPMSM because the $\boldsymbol{i}_{dq}$-HRG linearizes the magnetization of the machine around the operating point $\overline{\boldsymbol{i}_{dq}^*}$, resulting in a systematic error. Faraday's law of induction (2.4) used by the $\boldsymbol{\psi}_{\alpha\beta}$-HRG is equally valid for linearly and nonlinearly magnetized SMs, resulting in a reduced error for six-step operation compared to the $\boldsymbol{i}_{dq}$-HRG. Due to the omission of the harmonic component of the ohmic voltage drop in the flux linkage difference equation (4.10), caused by the voltage constraint in the overmodulation range, the $\boldsymbol{\psi}_{\alpha\beta}$-HRG also introduces a systematic error, which is, however, smaller than with the $\boldsymbol{i}_{dq}$-HRG. Moreover, the error of the $\boldsymbol{\psi}_{\alpha\beta}$-HRG can be considered small compared to the rated current (cf. Tab. A.3) and non-ideal effects in the actual application, e.g., measurement noise. For these reasons the $\boldsymbol{\psi}_{\alpha\beta}$-HRG should be preferred for nonlinearly magnetized SMs in terms of accuracy.

Fig. 4.12 shows the required execution time of the $\boldsymbol{\psi}_{\alpha\beta}$-HRG and the $\boldsymbol{i}_{dq}$-HRG, implemented in C running on a Lenovo T14s with an AMD Ryzen 7 1.9 GHz processor and 32 GB of RAM. It should be noted that only one processor core was used. Since a square matrix with a dimension proportional to N_{bvp} must be inverted for the $\boldsymbol{i}_{dq}$-HRG, the required execution time increases quadratically with the number of supporting points. The mean execution time for the $\boldsymbol{\psi}_{\alpha\beta}$-HRG

of 1.9 µs is significantly smaller than for the $\boldsymbol{i}_{\mathrm{dq}}$-HRG (cf. Fig. 4.12). For this reason, the $\boldsymbol{\psi}_{\alpha\beta}$-HRG is preferable in terms of computational load.

4.3 Pulse Clipping Scheme

As seen in Sec. 4.2, even with accurate knowledge of the machine parameters and flux linkages, errors exist in the flux linkage reference calculation of the HRG. In addition to these systematic errors, the solution of the HRG would also deviate from the flux linkage and current trajectories of the SM due to inaccurate machine parameters based on various influences like unmodeled parasitic effects such as slot harmonics or non-ideal inverter switching behavior.

If the steady-state flux linkage reference trajectory of the HRG differs from the flux linkage trajectory of the SM, the CCS-MPFC attempts to follow the HRG reference trajectory with voltage commands that would deviate from the overmodulation scheme reference voltage $\boldsymbol{u}^*_{\alpha\beta}[k]$ (cf. Sec. 4.2.3). Due to these voltage commands, six-step operation cannot be guaranteed because additional switching commands are introduced. In addition, the desired switching behavior, e.g., that only non-zero switching vectors should be active when the reference voltage $\boldsymbol{u}^*_{\alpha\beta}[k]$ of the HRG is on the hexagon boundary, cannot be realized. To achieve the desired switching behavior in the overmodulation range including six-step operation despite deviations between the reference and actual flux linkage trajectories, a PC method is proposed and described in the following.

The pulses $\boldsymbol{s}_{\mathrm{abc,ccs}}$ of the SVM calculated on the basis of $\boldsymbol{u}_{\alpha\beta,\mathrm{ccs}}$ (cf. Fig. 4.1) are clipped if the length of the pulses falls below certain thresholds, which depend on the reference voltage $\boldsymbol{u}^*_{\alpha\beta}[k]$ of the HRG. There are three different scenarios, see Fig. 4.13, defined below (sector 2 of the voltage hexagon is assumed):

1. $u^*_\beta < \frac{u_{\mathrm{DC}}}{\sqrt{3}}$:
   The reference voltage $\boldsymbol{u}^*_{\alpha\beta}[k]$ does not intersect the voltage hexagon boundaries, and zero and non-zero switching vectors are desired. Hence, only pulses smaller than the inverter interlocking time T_{i} are clipped.

2. $u^*_\beta = \frac{u_{\mathrm{DC}}}{\sqrt{3}} \wedge |u^*_\alpha| < \frac{u_{\mathrm{DC}}}{3}$:
   The reference voltage $\boldsymbol{u}^*_{\alpha\beta}[k]$ is located on the boundaries without being in a corner of the voltage hexagon. Therefore, only non-zero active switching vectors are desired. For this reason, the threshold for clipping non-zero active switching vectors remains the interlocking time T_{i}. For the zero vectors, an additional threshold $T_{\mathrm{c}} > T_{\mathrm{i}}$ is introduced as tuning parameter to prevent undesired switching behavior.

3. $\|\boldsymbol{u}^*_{\alpha\beta}\| = \frac{2u_{\mathrm{DC}}}{3}$:
   The reference voltage $\boldsymbol{u}^*_{\alpha\beta}[k]$ is located in the corner of the voltage hexagon. Here, no switching is desired during the sampling period. Thus, the threshold T_{c} is active for zero and non-zero switching vectors.

The threshold T_{c} should be set as low as possible, but high enough to ensure six-step operation without additional switching pulses. The tuning of T_{c} is done on a test bench at the rated operating point. Starting from $T_{\mathrm{i}} = T_{\mathrm{c}}$, T_{c} is increased until six-step operation is achieved without additional switching pulses.

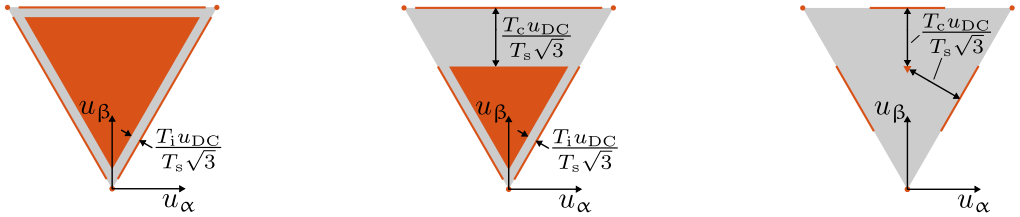

(a) $u^*_\beta < \frac{u_\mathrm{DC}}{\sqrt{3}}$ **(b)** $u^*_\beta = \frac{u_\mathrm{DC}}{\sqrt{3}} \wedge |u^*_\alpha| < \frac{u_\mathrm{DC}}{3}$ **(c)** $\|\boldsymbol{u}^*_{\alpha\beta}\| = \frac{2u_\mathrm{DC}}{3}$

Fig. 4.13: PC strategy and resulting sets (orange) of applied voltages formed by the pulses $\boldsymbol{s}_\mathrm{abc}$ (cf. Fig. 4.1) for $T_\mathrm{s} = 62.5\,\mu\mathrm{s}$, $T_\mathrm{c} = 20\,\mu\mathrm{s}$, and $T_\mathrm{i} = 3.3\,\mu\mathrm{s}$ (sector 2 of the voltage hexagon is shown) [6, Fig. 14]

In Fig. 4.14, a simulative step response for the nonlinearly magnetized IPMSM model defined in App. A.2 to the rated operating point at $n_\mathrm{me} = 5350\,\mathrm{min}^{-1}$ is shown. The elementary vectors $s_n = \{1, 8\}$ are defined as in Tab. 2.1. For $t < 0\,\mathrm{s}$ a modulation index within the linear modulation range is required and, therefore, the switching behavior of the inverter with and without PC is the same. By applying the step response to rated operation, the full DC-link voltage ($m = 1$) is required. Due to model and numerical inaccuracies of the CCS-MPFC and the HRG, the inverter without PC inserts short switching pulses, resulting in slightly reduced fundamental voltages and currents. On the other hand, with the PC scheme active, these short pulses can be suppressed and the desired switching behavior (six-step operation) and maximum power conversion of the drive system can be ensured.

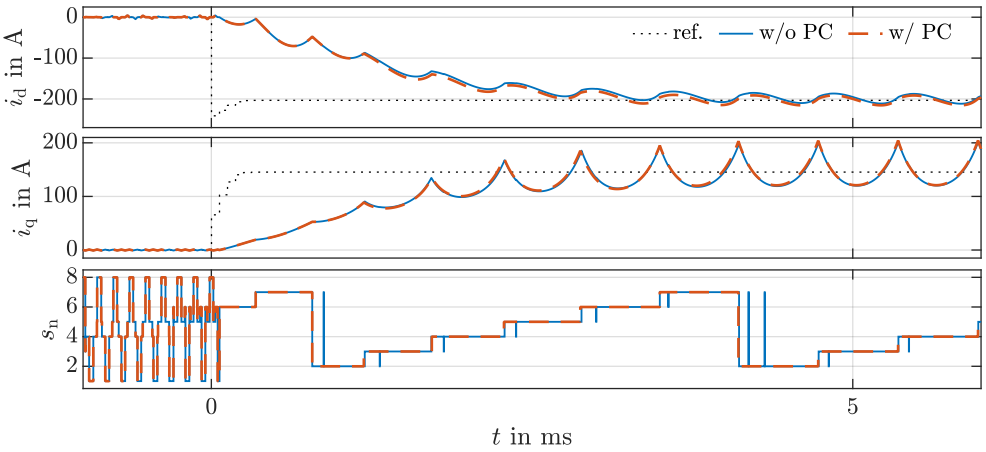

Fig. 4.14: Simulative step response for the nonlinearly magnetized IPMSM, cf. App. A.2, to rated operation at $n_\mathrm{me} = 5350\,\mathrm{min}^{-1}$ for $T_\mathrm{s} = 62.5\,\mu\mathrm{s}$ with ($T_\mathrm{c} = 15\,\mu\mathrm{s}$) and without activated PC scheme [6, Fig. 15]

4.4 Experimental Investigation

In order to prove the effectiveness and performance of the control strategy with the presented HRG and PC, several representative experiments in the constant-torque and constant-power

Tab. 4.3: Controller parameters

PC		
Pulse clipping time	T_c	$15\,\mu\mathrm{s}$
GFO		
Damping ratio	ξ	1
Characteristic frequency	ω_0	$675\,\mathrm{s}^{-1}$
FMC		
Low-pass filter time constant	τ	$20\,\mathrm{ms}$
Speed threshold	ω_fmc	$270\,\mathrm{s}^{-1}$

region have been carried out which are shown in the following. The description of the experimental setup is given in App. B. The controller parameters of the overall control scheme are listed in Tab. 4.3.

The turnaround times of OPC, FMC, GFO, HRG, CCS-MPFC, auxiliary functions, and the overall control strategy are listed in Tab. 4.4. Here, the low computational load of the HRG and FMC can be seen. The auxiliary functions item summarizes the turnaround times of all calculations, e.g., PC, SVM, coordinate transformations, analog-digital conversion, and processor and host communication, that must be executed in addition to OPC, FMC, GFO, HRG, and CCS-MPFC.

Tab. 4.4: Turnaround times of the proposed control strategy with HRG

	Mean turnaround time in µs
OPC	8.4
FMC	1.3
GFO	2.3
HRG	1.7
CCS-MPFC	3.6
Auxiliary functions	29.3
Overall control strategy	46.6

4.4.1 Torque Transient

To investigate the transient torque control performance, a step response from zero reference torque to rated torque (maximum torque) is shown in Fig. 4.15 at $n_\mathrm{me} = 5350\,\mathrm{min}^{-1}$, which is slightly above the nominal speed of $n_\mathrm{me} = 5330\,\mathrm{min}^{-1}$, requiring six-step operation during steady-state operation. Here, the CCS-MPFC reaches the flux linkage reference trajectory calculated by the HRG within approx. 3 ms and seamlessly switches to six-step operation thanks to the PC scheme, see Fig. 4.15b. Moreover, in Fig. 4.15a the robustness of the strategy is demonstrated as it overcomes external disturbances:

- Due to the limited capacity of the DC-link capacitor and the finite settling time of the DC-link voltage controller, the rapidly increasing current amplitude causes the DC-link voltage to drop for a short time.
- The rapidly increasing torque leads to an acceleration of the rotor shaft and, therefore, to a short-time increase of the rotor speed due to the limited moment of inertia of the coupled rotor shaft (load and test machine) and the finite settling time of the speed controller of the load machine.

Both effects lead to a short-time contraction of the voltage limit. Therefore, the OPC selects an operating point $\overline{\boldsymbol{i}_{\mathrm{dq}}^{*}}$ with less flux linkage amplitude and less torque. Nevertheless, the controller is able to maintain six-step operation and provides maximum torque in this challenging scenario. The ability to operate under transiently varying DC-link voltages and speeds is an important feature of the presented methodology, as this problem is encountered in many industrial applications (e.g., automation and traction drives).

4.4.2 Speed Transient

To analyze the control performance during transient speed changes, the speed was increased from $4500\,\mathrm{min}^{-1}$ to $11\,000\,\mathrm{min}^{-1}$ by the speed-controlled load induction machine (IM) while maximum torque operation was attained by the test IPMSM, see Fig. 4.16 and Fig. 4.17. During maximum torque operation the desired torque T^{*} is saturated. Therefore, the saturated value of the torque reference denoted as $T\left(\overline{\boldsymbol{i}_{\mathrm{dq}}^{*}}\right)$ instead of T^{*} is shown in Fig. 4.16. Below the nominal speed of $5330\,\mathrm{min}^{-1}$, the operating point chosen by the OPC corresponds to the intersection of the MTPC trajectory and the current limit. Above the nominal speed, the intersection of the current and voltage limits is selected. Since the short-circuit point of the test IPMSM is at the current limit, no MTPV operation is required to achieve maximum torque.

Due to increasing speed, operation at the voltage limit is inevitable, covering the entire overmodulation range. To reach the mean current operating points $\overline{\boldsymbol{i}_{\mathrm{dq}}^{*}}$ specified by the OPC, the HRG adds a harmonic component to the mean flux linkage reference in the overmodulation range, see Fig. 4.16. Only minor deviations exist between the estimated flux linkage $\hat{\boldsymbol{\psi}}_{\alpha\beta}$ and the reference flux linkage $\boldsymbol{\psi}_{\alpha\beta}^{*}$. For further analysis of the IPMSM's torque, current, and flux trajectories as well as switching pattern, enlarged snapshots from Fig. 4.16 for the constant-torque and constant-power region are shown in Fig. 4.18 and Fig. 4.19.

In the linear modulation range ($m < 0.907$), as expected, the flux reference contains no additional harmonic components added by the HRG, and no additional torque, current, and flux linkage harmonics exist due to the hexagonal voltage constraints, see Fig. 4.16 and Fig. 4.18a.

In the overmodulation range mode I ($0.907 < m \leq 0.952$) zero voltage vectors are selected, cf. Fig. 4.18a, and in overmodulation range II ($0.952 < m \leq 1$) the actuated mean voltage vectors are located solely on the boundary of the voltage hexagon, i.e., the zero voltage vectors are no longer selected. By reaching the nominal speed ($n_{\mathrm{me}} = 5330\,\mathrm{min}^{-1}$), six-step operation has to be applied which leads to inevitable high torque, current, and flux linkage harmonics, see Fig. 4.19. Since six-step operation is used continuously at speeds above the nominal speed ($n_{\mathrm{me}} = 5330\,\mathrm{min}^{-1}$) during maximum torque generation, the DC-link voltage is utilized to its maximum extend and maximum power generation is ensured. Here, decreasing phase current

harmonics for increasing machine speed exist, cf. Fig. 4.19. Two reasons are responsible for that:

- The voltage harmonics of six-step operation have a decreasing effect on currents and fluxes as frequencies increase due to the low-pass characteristics of the stator winding system.
- The degree of saturation of the nonlinearly magnetized IPMSM is lower at high speed operating points, resulting in larger differential inductance values, see Fig. A.2 and Fig. A.3, and thus lower current harmonics.

Thanks to the presented HRG and PC, overmodulation including six-step operation can be ensured which successfully enables the maximum power conversion of the drive system.

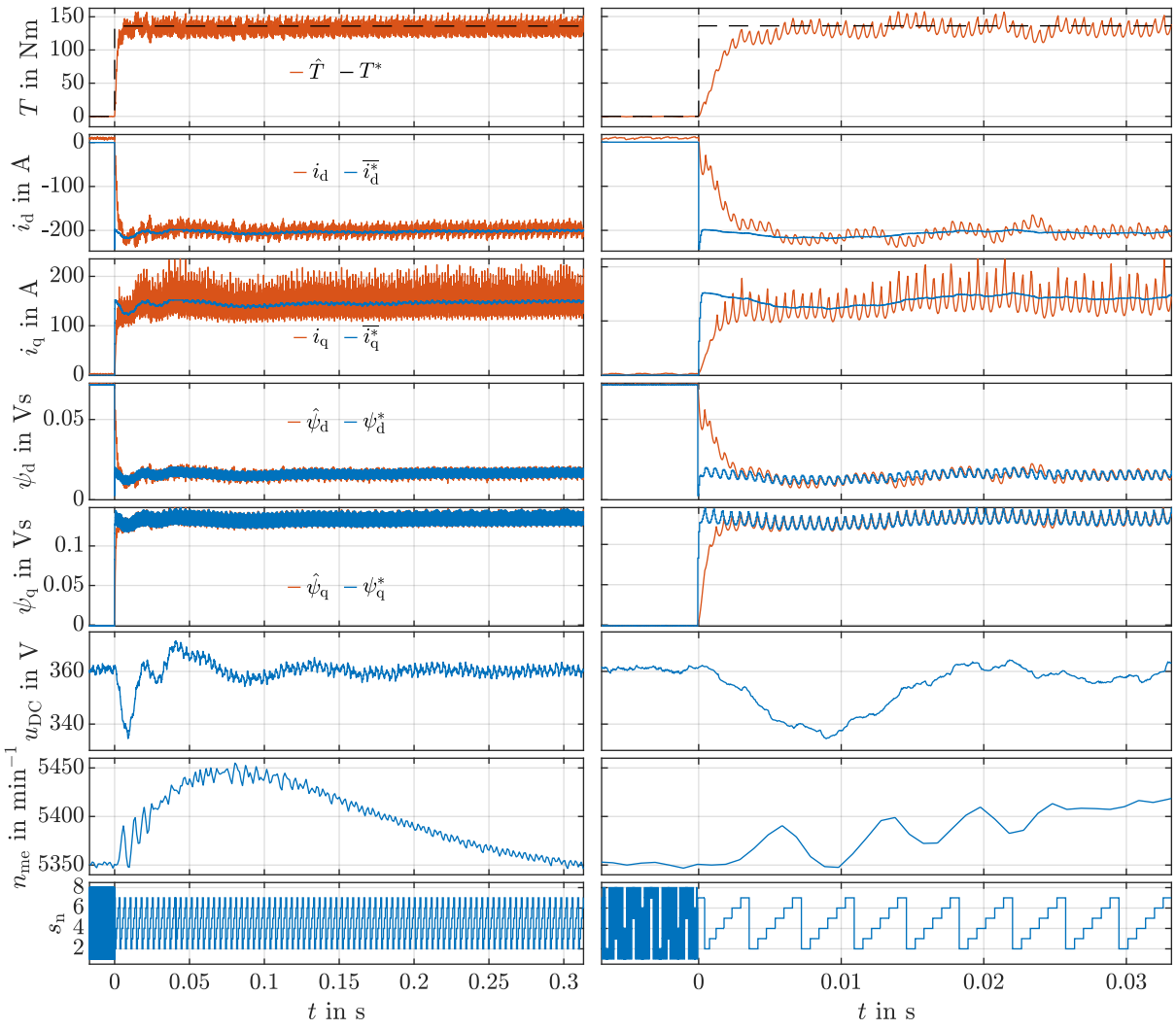

(a) Full view **(b)** Zoom in

Fig. 4.15: Torque step response to the rated torque following the MTPC strategy at $n_{me} = 5350\,\mathrm{min}^{-1}$ [6, Fig. 17]

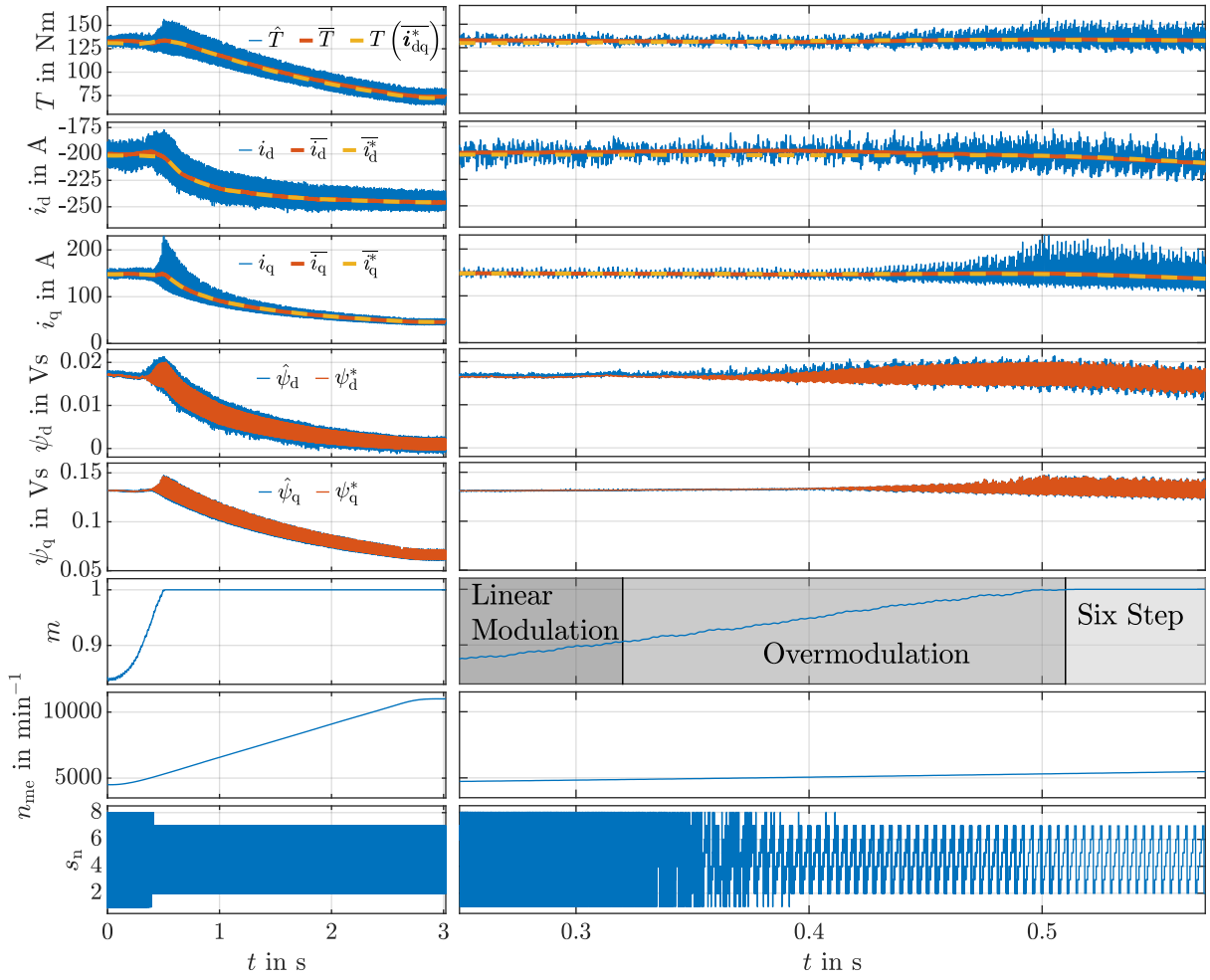

(a) Full view **(b)** Zoom in

Fig. 4.16: Speed transient from $n_{\mathrm{me}} = 4500\,\mathrm{min}^{-1}$ to maximum speed ($n_{\mathrm{me}} = 11\,000\,\mathrm{min}^{-1}$) while maximum torque operation is achieved

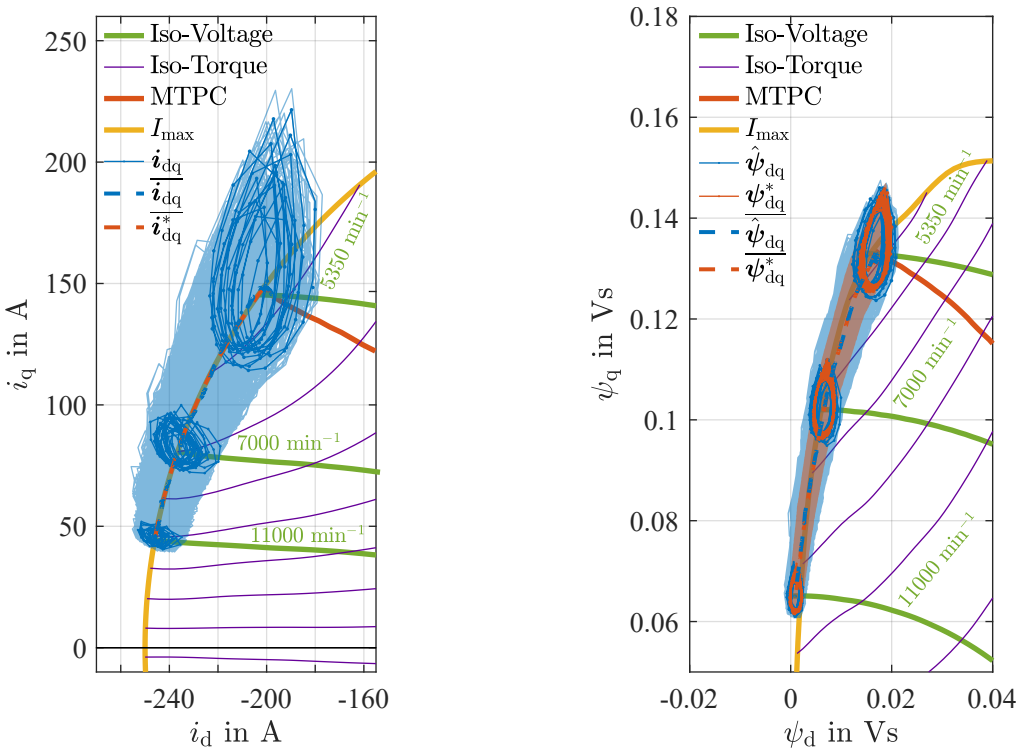

(a) Current domain

(b) Flux domain

Fig. 4.17: State and reference trajectories as well as machine-characteristic loci during the speed transient from Fig. 4.16

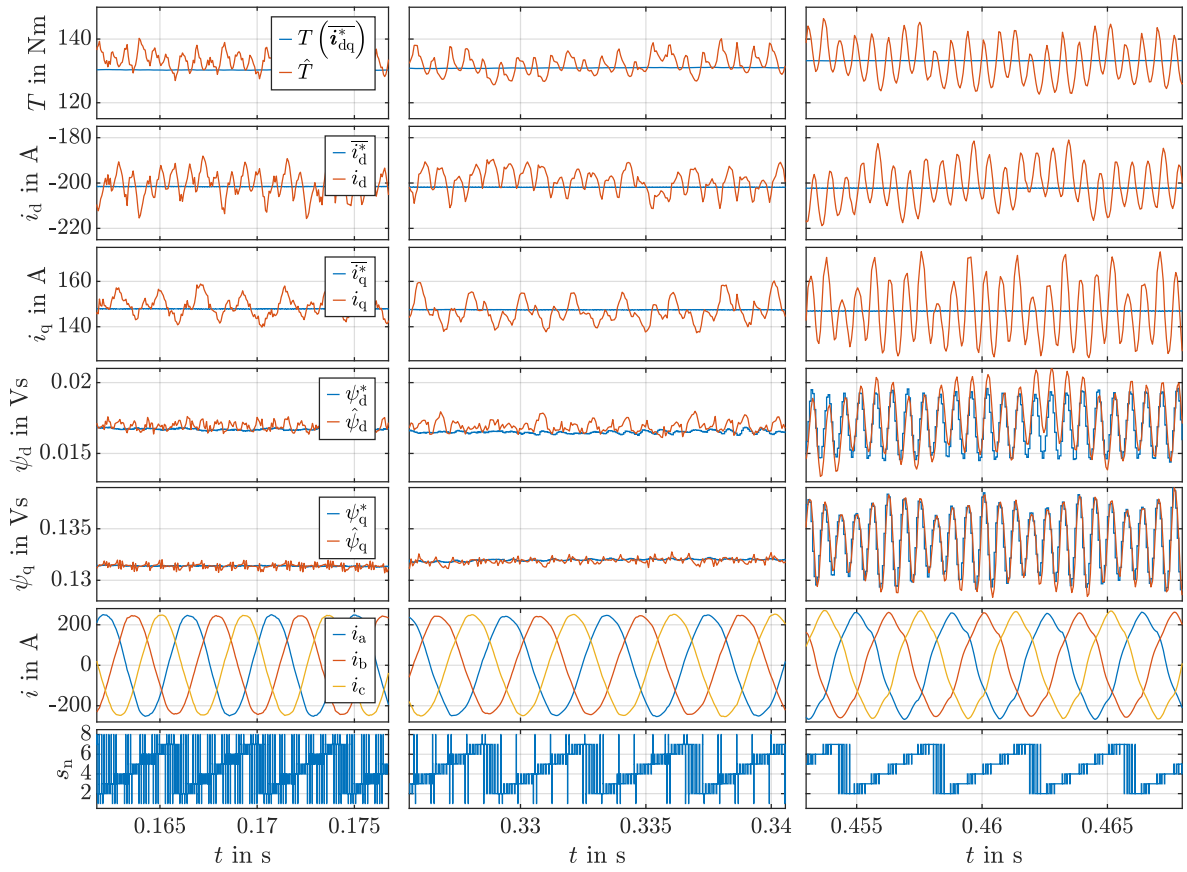

(a) $n_{\mathrm{me}} = 4600\,\mathrm{min}^{-1}, m = 0.85$ **(b)** $n_{\mathrm{me}} = 4900\,\mathrm{min}^{-1}, m = 0.91$ **(c)** $n_{\mathrm{me}} = 5200\,\mathrm{min}^{-1}, m = 0.98$

Fig. 4.18: Torque, current, flux, and switching trajectories for different speeds from Fig. 4.16 in the linear and overmodulation region

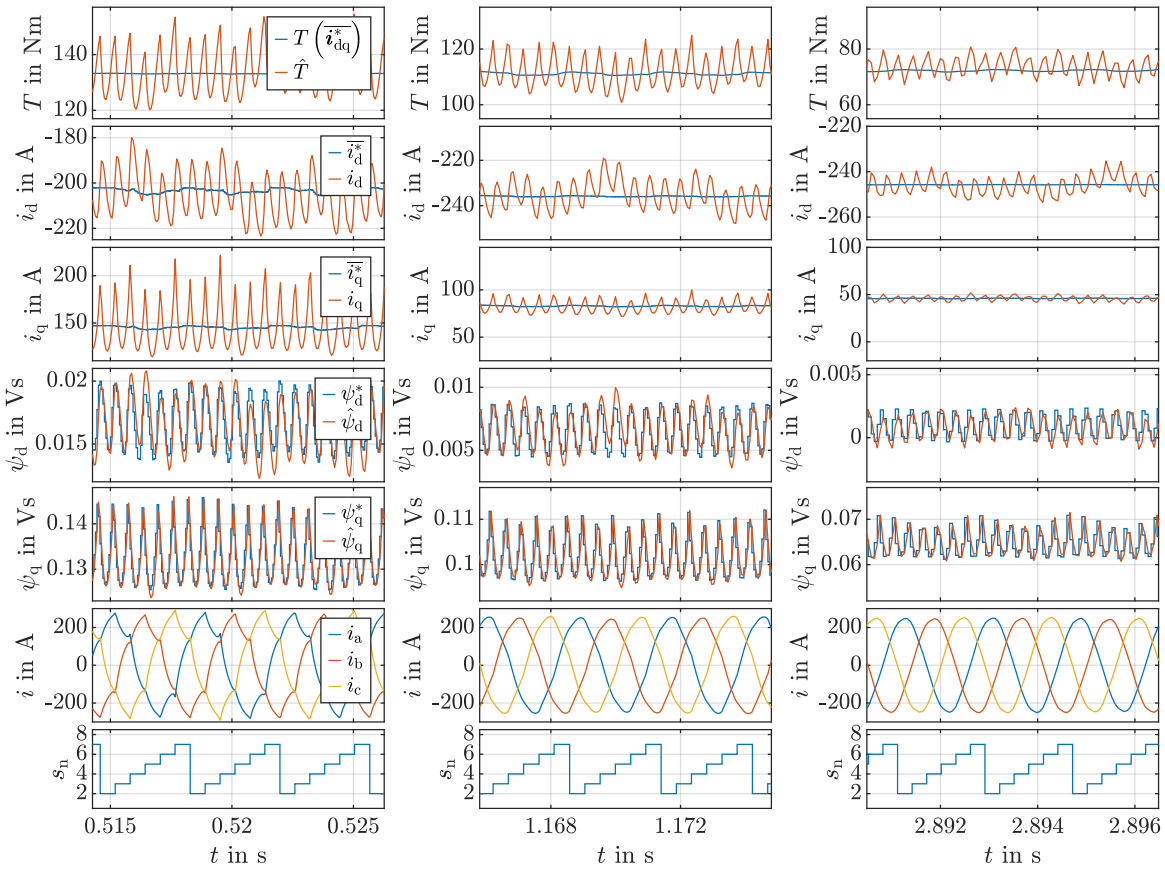

(a) $n_{\mathrm{me}} = 5350\,\mathrm{min}^{-1}, m = 1$ **(b)** $n_{\mathrm{me}} = 7000\,\mathrm{min}^{-1}, m = 1$ **(c)** $n_{\mathrm{me}} = 11\,000\,\mathrm{min}^{-1}, m = 1$

Fig. 4.19: Torque, current, flux, and switching trajectories for different speeds from Fig. 4.16 during six-step operation

5 Time-Optimal Control Considering Current and Torque Constraints

The following chapter is based on the own publications [7, 8]. The author of this thesis contributed the main parts of [7, 8], in particular, the proposed control method concepts as well as the simulative and experimental investigations. He also prepared the publications independently, while the contributions of the other co-authors were limited to technical discussions during the investigation phase as well as proofreading of the manuscripts. Therefore, parts of the following text have been taken in modified or unmodified form from the mentioned publications. For the sake of readability, the underlying self-citations are not explicitly listed in the following.

In this chapter, the RPR scheme and the CCS-MPFC (3.5) extended with state constraints are presented. Here, the RPR solves the TOC problem numerically in every sampling instant without considering torque and current limits by applying Pontryagin's principle. The TOC solution is incorporated by manipulating the reference flux linkage $\boldsymbol{\psi}^*_{\alpha\beta}$ of the CCS-MPFC. Here, the flux linkage reference $\boldsymbol{\psi}_{\mathrm{dq}}(\boldsymbol{i}^*_{\mathrm{dq}})$ in the dq coordinate system, which is transformed to the $\alpha\beta$ coordinate system with the instantaneous electrical rotor angle ε, is pre-rotated by a certain angle calculated by the RPR. To steer the flux linkage of the SM to the flux linkage reference of the RPR, the CCS-MPFC including torque and current limits as softened state constraints is applied. Thanks to the RPR and the state constraints of the CCS-MPFC, the following beneficial properties can be achieved for the overall control scheme shown in Fig. 5.1:

- The overall control scheme is able to achieve minimum settling times during transient operation in the entire speed and torque range thanks to the reference flux linkage manipulation of the CCS-MPFC by the RPR.
- Compared to the TOC methods proposed in [15–20], overcurrents as well as torque overshoots and undershoots during transient operation are prevented by time-varying torque and current limits implemented as linear state constraints for the QP of the CCS-MPFC.

Nevertheless, the overall control scheme is limited to the linear modulation range because the RPR assumes that the flux linkage reference rotates circularly with constant angular velocity and amplitude during steady-state operation which is only the case in the linear modulation range. Therefore, the modulation index of the OPC is limited to $m_{\max} = 0.907$, see Fig. 5.1.

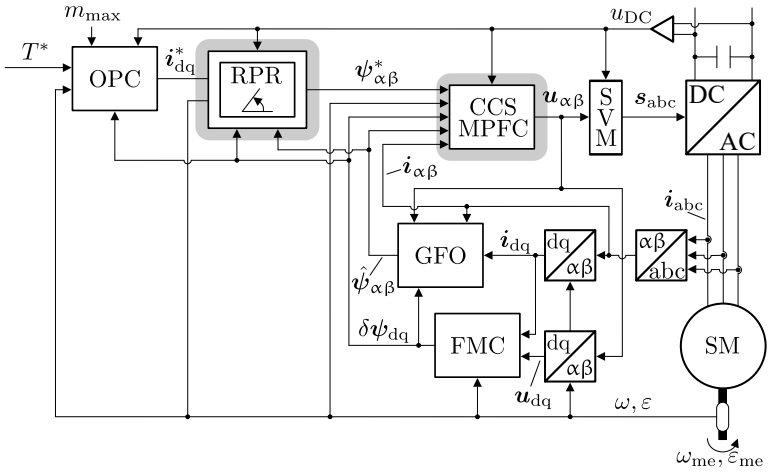

Fig. 5.1: Overall control scheme (gray shaded part is the focus of Ch. 5) [7, derivate of Fig. 1]

5.1 Reference Pre-Rotation

The task of the RPR is to calculate a reference flux linkage $\boldsymbol{\psi}^*_{\alpha\beta}[k+1]$ for the CCS-MPFC without respect to overcurrents as well as torque overshoots and undershoots such that the time required to reach the operating point $\boldsymbol{i}^*_{\mathrm{dq}}$ during transient operation is minimized. Thus, the RPR inherently solves the TOC problem. The inputs and outputs of the RPR are shown in Fig. 5.2. In Fig. 5.3 exemplary simulative flux linkage trajectories with and without the RPR are depicted to show the transient control performance improvement by utilizing an RPR. Here, the time to reach the reference is decreased from 21 to 8 sampling periods.

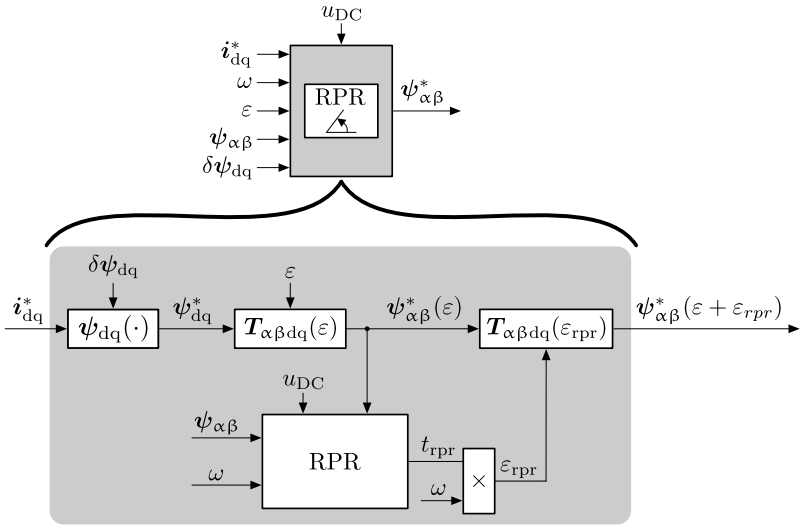

Fig. 5.2: Block diagram of the RPR

5.1.1 Steady-State Control Conditions

During steady-state control conditions $\boldsymbol{i}^*_{\mathrm{dq}}[k] = \boldsymbol{i}_{\mathrm{dq}}[k]$, the reference flux linkage is given by

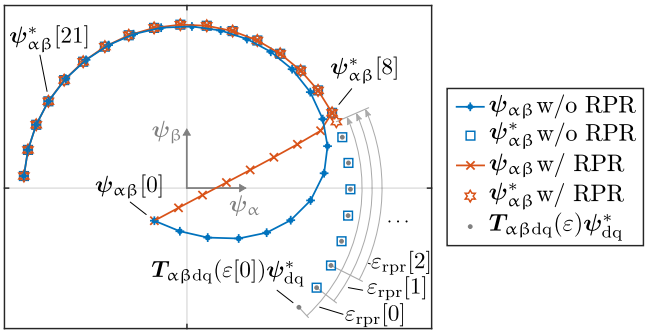

Fig. 5.3: Exemplary transient flux linkage trajectories with and without the pre-rotation of the flux linkage reference [8, Fig. 10]

$$\boldsymbol{\psi}^*_{\alpha\beta}[k+1] = \boldsymbol{T}_{\alpha\beta dq}\left(\omega[k]T_s\right) \underbrace{\boldsymbol{T}_{\alpha\beta dq}\left(\varepsilon[k]\right) \boldsymbol{\psi}_{dq}\left(\boldsymbol{i}^*_{dq}[k]\right)}_{\boldsymbol{\psi}_{\alpha\beta}\left(\boldsymbol{i}^*_{dq},\varepsilon\right)}. \tag{5.1}$$

The flux linkage reference $\boldsymbol{\psi}_{dq}(\boldsymbol{i}^*_{dq}[k])$ in (5.1) is derived with a current-to-flux linkage LUT, see Fig. A.2, for the operating point $\boldsymbol{i}^*_{dq}$, which is calculated by the OPC, to take (cross-)saturation effects into account. For a constant operating point $\boldsymbol{i}^*_{dq}$ and speed ω in the linear modulation range, the operating point in the $\alpha\beta$ flux linkage coordinate system $\boldsymbol{\psi}_{\alpha\beta}(\boldsymbol{i}^*_{dq}, \varepsilon)$ rotates with a constant magnitude and angular velocity ω, see (5.1) and Fig. 5.5c.

5.1.2 Transient Control Conditions

To find the time-optimal stator voltages $\boldsymbol{u}_{\alpha\beta}(t)$ during transients to steer the SM's flux $\boldsymbol{\psi}_{\alpha\beta}$ to its reference $\boldsymbol{\psi}^*_{\alpha\beta}$ for neglected state constraints, e.g., overcurrents as well as torque overshoots and undershoots, the RPR must solve the following TOC problem:

$$\min_{\boldsymbol{u}_{\alpha\beta}(t)} t_{rpr} \tag{5.2a}$$

$$\text{s.t.} \quad \frac{\mathrm{d}}{\mathrm{d}t}\boldsymbol{\psi}_{\alpha\beta}(t) = \boldsymbol{u}_{\alpha\beta}(t), \quad \boldsymbol{\psi}_{\alpha\beta}(kT_s) = \boldsymbol{\psi}_{\alpha\beta}[k], \tag{5.2b}$$

$$\|\boldsymbol{u}_{\alpha\beta}(t)\| \leq u_{max} \quad \forall t \in [kT_s, kT_s + t_{rpr}], \tag{5.2c}$$

$$\boldsymbol{\psi}_{\alpha\beta}(kT_s + t_{rpr}) = \boldsymbol{\psi}^*_{\alpha\beta}(kT_s + t_{rpr}). \tag{5.2d}$$

Here, the ohmic voltage drop for the system dynamics (5.2b) is neglected, since during transients the stator voltage $\boldsymbol{u}_{\alpha\beta}$ is driven into saturation and thus the ohmic voltage drop is small compared to $\boldsymbol{u}_{\alpha\beta}$. Furthermore, the voltage hexagon is approximated with a circular input constraint (5.2c). The magnitude of this circular approximation is set to

$$u_{max} = \frac{2}{\pi} u_{DC}[k], \tag{5.3}$$

which corresponds to the fundamental voltage of six-step operation [5].

To the best of the author's knowledge, the TOC problem for SMs was first studied and solved by Jong-Woo and Sul in [17] with $\boldsymbol{i}_{dq}$ as state variable under the assumption of a linear magnetization. The TOC studies for SMs [15, 18, 20] employed the flux linkage $\boldsymbol{\psi}_{dq}$ in the rotor-fixed dq frame

as state variable. In the following, the TOC problem (5.2) with the flux linkage $\boldsymbol{\psi}_{\alpha\beta}$ in the stator-fixed $\alpha\beta$ frame is solved by applying Pontryagin's principle [67, 78]. Obviously, the solution of the TOC problem must be independent of the chosen state variable. Nevertheless, it is worth mentioning that the choice of $\boldsymbol{\psi}_{\alpha\beta}$ as state variable greatly simplifies the application of Pontryagin's principle compared to the use of $\boldsymbol{\psi}_{\mathrm{dq}}$ and $\boldsymbol{i}_{\mathrm{dq}}$. This is because the ODE describing the dynamics of $\boldsymbol{\psi}_{\alpha\beta}$ is an integrator.

With the help of the Hamiltonian of (5.2)

$$H(\boldsymbol{u}_{\alpha\beta}(t), \boldsymbol{\lambda}(t)) = 1 + (\boldsymbol{\lambda}(t))^{\intercal} \boldsymbol{u}_{\alpha\beta}(t), \tag{5.4}$$

the ODE of the costate (adjoint) variable $\boldsymbol{\lambda}$ evaluates to

$$\frac{\mathrm{d}}{\mathrm{d}t}\boldsymbol{\lambda}(t) = -\frac{\partial H(\boldsymbol{u}_{\alpha\beta}(t), \boldsymbol{\lambda}(t))}{\partial \boldsymbol{\psi}_{\alpha\beta}} = \boldsymbol{0}. \tag{5.5}$$

Hence, the costate $\boldsymbol{\lambda}$ of the TOC problem (5.2) is constant.

Furthermore, the optimal control $\boldsymbol{u}_{\alpha\beta}(t)$ has to satisfy Pontryagin's principle

$$H(\boldsymbol{u}_{\alpha\beta}(t), \boldsymbol{\lambda}) = \min_{\boldsymbol{U}_{\alpha\beta}(t)} \underbrace{1 + \boldsymbol{\lambda}^{\intercal} \boldsymbol{U}_{\alpha\beta}(t)}_{H(\boldsymbol{U}_{\alpha\beta}(t), \lambda)} \tag{5.6a}$$

$$\text{s.t. } \|\boldsymbol{U}_{\alpha\beta}(t)\| \leq u_{\max} \quad \forall t \in [kT_{\mathrm{s}}, kT_{\mathrm{s}} + t_{\mathrm{rpr}}]. \tag{5.6b}$$

From (5.6), the time-optimal $\boldsymbol{u}_{\alpha\beta}(t)$ can be derived as a function of the costate

$$\boldsymbol{u}_{\alpha\beta}(t) = -u_{\max} \frac{\boldsymbol{\lambda}}{\|\boldsymbol{\lambda}\|}. \tag{5.7}$$

Although the optimal control $\boldsymbol{u}_{\alpha\beta}(t)$ is still unknown since the costate $\boldsymbol{\lambda}$ is unknown, two important characteristics can be observed from (5.7):

1. The time-optimal stator voltages $\boldsymbol{u}_{\alpha\beta}(t)$ are constant.
2. The time-optimal stator voltages $\boldsymbol{u}_{\alpha\beta}(t)$ are saturated by the input constraint.

This results in linearly shaped trajectories of the flux linkage $\boldsymbol{\psi}_{\alpha\beta}(t)$ of the SM when the ohmic voltage drop is neglected.

To solve the TOC, a set of nonlinear equations for the time t_{rpr}, that is needed to steer the SM's flux $\boldsymbol{\psi}_{\alpha\beta}$ to its reference $\boldsymbol{\psi}^*_{\alpha\beta}$, and the constant stator voltage $\boldsymbol{u}_{\alpha\beta}$ must be solved:

$$\underbrace{\boldsymbol{T}_{\alpha\beta\mathrm{dq}}(\varepsilon[k] + \overbrace{\omega[k] t_{\mathrm{rpr}}}^{\varepsilon_{\mathrm{rpr}}[k]}) \boldsymbol{\psi}_{\mathrm{dq}}\left(\boldsymbol{i}^*_{\mathrm{dq}}[k]\right)}_{\boldsymbol{\psi}^*_{\alpha\beta}(kT_{\mathrm{s}} + t_{\mathrm{rpr}})} = \underbrace{\boldsymbol{\psi}_{\alpha\beta}[k] + t_{\mathrm{rpr}} \boldsymbol{u}_{\alpha\beta}}_{\boldsymbol{\psi}_{\alpha\beta}\left(kT_{\mathrm{s}} + t_{\mathrm{rpr}}, \boldsymbol{u}_{\alpha\beta}\right)}, \tag{5.8a}$$

$$\|\boldsymbol{u}_{\alpha\beta}\| = u_{\max}. \tag{5.8b}$$

Here, (5.8a) corresponds to the terminal constraint (5.2d), whereas the left side of (5.8a) represents the pre-rotation of the flux reference $\boldsymbol{\psi}^*_{\alpha\beta}$ as a function of the rotation angle $\varepsilon_{\mathrm{rpr}}[k] = \omega[k] t_{\mathrm{rpr}}$ and the right side represents the linear evolution of $\boldsymbol{\psi}_{\alpha\beta}$ as a function of t_{rpr} and $\boldsymbol{u}_{\alpha\beta}$. After a

time duration of t_{rpr}, the predicted flux $\boldsymbol{\psi}_{\alpha\beta}$ must coincide with the reference flux $\boldsymbol{\psi}^*_{\alpha\beta}$, whereby a constant voltage $\boldsymbol{u}_{\alpha\beta}$ with maximum amplitude $u_{\max}$ is applied.

To solve the system of nonlinear equations (5.8) in every sampling instant, numerical methods must be applied. A method to iteratively solve (5.8) for t_{rpr} is given in pseudocode Alg. 1 from line 1 to 9 and a graphical representation is given in Fig. 5.4. Here, N iteration steps are performed from line 6 to 9 to approximate the solution of (5.8) with $t_{\mathrm{rpr}} \approx t_{\mathrm{rpr},n}$ and $\boldsymbol{\psi}^*_{\alpha\beta}\left(kT_{\mathrm{s}} + t_{\mathrm{rpr}}\right) \approx \psi^*_{\alpha\beta,N}$. The iteration step from line 6 to 9 is similar to the iteration step that is only performed once per sampling instant for the RRCC method proposed in [19]. In lines 10 to 14 of Alg. 1, a distinction between transient and steady-state control operation is made. If the time t_{rpr} to steer $\boldsymbol{\psi}_{\alpha\beta}$ to its reference $\boldsymbol{\psi}^*_{\alpha\beta}$ is less than a chosen threshold t_{thresh}, steady-state control operation is present and $\boldsymbol{\psi}^*_{\alpha\beta}[k+1]$ is set according to (5.1). Otherwise, the controller is in transient operation and the reference $\boldsymbol{\psi}^*_{\alpha\beta}$ is pre-rotated by the angle $\omega[k]t_{\mathrm{rpr}}$, cf. (5.8a). The threshold t_{thresh} is a tuning parameter and must be set to $t_{\mathrm{thresh}} \geq T_{\mathrm{s}}$. Here, $t_{\mathrm{thresh}} = T_{\mathrm{s}}$ would be the obvious choice. Since the voltage hexagon is approximated circularly, slightly increased values for t_{thresh} are recommended, e.g., $t_{\mathrm{thresh}} = 1.1T_{\mathrm{s}}$ ... $1.5T_{\mathrm{s}}$.

Applying the DBFC law (3.8) with the calculated flux linkage reference $\boldsymbol{\psi}^*_{\alpha\beta}[k+1]$ of the RPR results in time-optimal transient and accurate steady-state operation. To saturate the voltages (3.8) to the voltage hexagon, the minimum phase error dynamic overmodulation scheme [83] must be applied.

Algorithm 1 Reference Pre-Rotation

Input: $\boldsymbol{i}^*_{\mathrm{dq}}[k], u_{\mathrm{DC}}[k], \omega[k], \varepsilon[k], \boldsymbol{\psi}_{\alpha\beta}[k], T_{\mathrm{s}}$
Output: $\boldsymbol{\psi}^*_{\alpha\beta}[k+1]$

1: Choose $t_{\mathrm{thresh}} \in \mathbb{R}$ s.t. $t_{\mathrm{thresh}} \geq T_{\mathrm{s}}$
2: Choose $N \in \mathbb{N}$
3: Initialize $t_{\mathrm{rpr},0} = 0\,\mathrm{s}$
4: Initialize $\psi^*_{\alpha\beta,0} = \boldsymbol{T}_{\alpha\beta\mathrm{dq}}\left(\varepsilon[k]\right)\boldsymbol{\psi}_{\mathrm{dq}}\left(\boldsymbol{i}^*_{\mathrm{dq}}[k]\right)$
5: Set $\|\boldsymbol{u}_{\alpha\beta}\| = \frac{2}{\pi}u_{\mathrm{DC}}[k]$
6: **for** $n = 1$ to N **do**
7: $\quad t_{\mathrm{rpr},n} = \frac{\|\psi^*_{\alpha\beta,n-1} - \boldsymbol{\psi}_{\alpha\beta}[k]\|}{\|\boldsymbol{u}_{\alpha\beta}\|}$
8: $\quad \psi^*_{\alpha\beta,n} = \boldsymbol{T}_{\alpha\beta\mathrm{dq}}\left(\omega[k]t_{\mathrm{rpr},n}\right)\psi^*_{\alpha\beta,0}$
9: **end for**
10: **if** $t_{\mathrm{rpr},n} > t_{\mathrm{thresh}}$ **then**
11: $\quad \boldsymbol{\psi}^*_{\alpha\beta}[k+1] = \psi^*_{\alpha\beta,N}$
12: **else**
13: $\quad \boldsymbol{\psi}^*_{\alpha\beta}[k+1] = \boldsymbol{T}_{\alpha\beta\mathrm{dq}}\left(\varepsilon[k] + \omega[k]T_{\mathrm{s}}\right)\boldsymbol{\psi}_{\mathrm{dq}}\left(\boldsymbol{i}^*_{\mathrm{dq}}[k]\right)$
14: **end if**

However, TOC performance is achieved by applying the DBFC (3.8) with the RPR, neither unintended current limit violations nor torque overshoots and undershoots can be prevented. This is shown by a simulation, cf. Fig. 5.5, with steps in the reference torque T^* and the corresponding reference currents $\boldsymbol{i}^*_{\mathrm{dq}}$ calculated by the OPC. For the sake of clarity, only the discrete-time samples with $T_{\mathrm{s}} = 62.5\,\mu\mathrm{s}$ that are synchronized with the SVM are shown. Therefore, the current, torque, and flux ripples induced by the switching of the inverter are not visible in the following

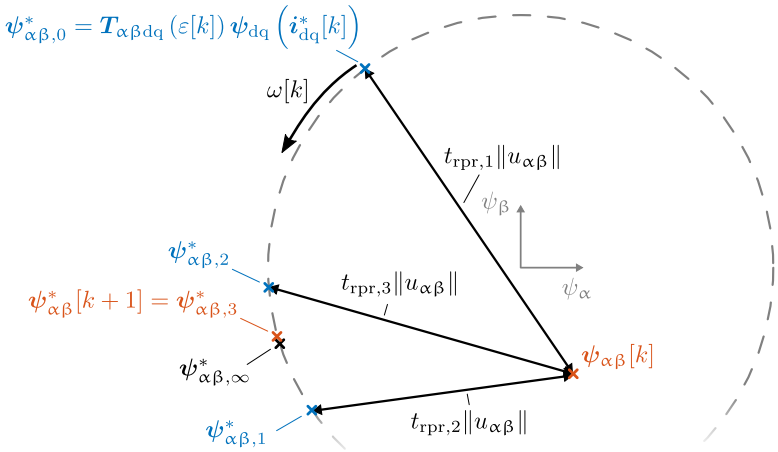

Fig. 5.4: Illustration of the RPR procedure with $N = 3$ [7, Fig. 2]

figures. For this simulation, the linearly magnetized IPMSM is used with the parameters given in Tab. A.2.

In Fig. 5.5a, the flux linkage reference $\boldsymbol{\psi}^*_{\alpha\beta}$ calculated by the RPR and the resulting $\boldsymbol{u}_{\alpha\beta}$ calculated with the deadbeat control law (3.8) including the minimum phase error dynamic overmodulation scheme are depicted. Here, nearly constant flux linkage references $\boldsymbol{\psi}^*_{\alpha\beta}$ and voltages $\boldsymbol{u}_{\alpha\beta}$ during transients can be seen. The slight deviations of the constant voltages $\boldsymbol{u}_{\alpha\beta}$ during transients are caused by the RPR with the circular approximation of the voltage hexagon, the neglected ohmic voltage drop, and the finite number of iterations. However, these deviations can be considered as minor, resulting in the characteristic time-optimal linear evolution of the flux linkage $\boldsymbol{\psi}_{\alpha\beta}$ during transients in the $\alpha\beta$ flux linkage plane, cf. Fig. 5.5c.

Furthermore, the time-optimal trajectories can be visualized in the dq current coordinate system, see Fig. 5.5b. Here, the current change caused by the induced voltage, characterized by $\boldsymbol{E}_{\boldsymbol{i}}(\boldsymbol{i}_{dq})$, is optimally exploited by the RPR to achieve TOC performance. Nevertheless, current limits are violated and torque overshoots and undershoots cannot be avoided, see Fig. 5.5a and Fig. 5.5b.

To investigate the influence of the number of RPR iterations N on the control performance, the transients ① and ② of the scenario depicted in Fig. 5.5 are shown in Fig. 5.6 for $N = \{0; 1; 2; 5; 100\}$. For $N = 0$ no pre-rotation of the flux linkage reference is performed and $N = 100$ represents an approximation of $N = \infty$. It can be seen that the deadbeat controller without pre-rotation of the reference ($N = 0$) cannot reach it's reference within the given time. For $N \geq 5$, the time-optimal characteristic linearly shaped flux linkage trajectories during transient operation are achieved due to the fast convergence of the RPR. Increasing N to more than 5 would not significantly improve the results, but would increase the computational load, which is not desirable.

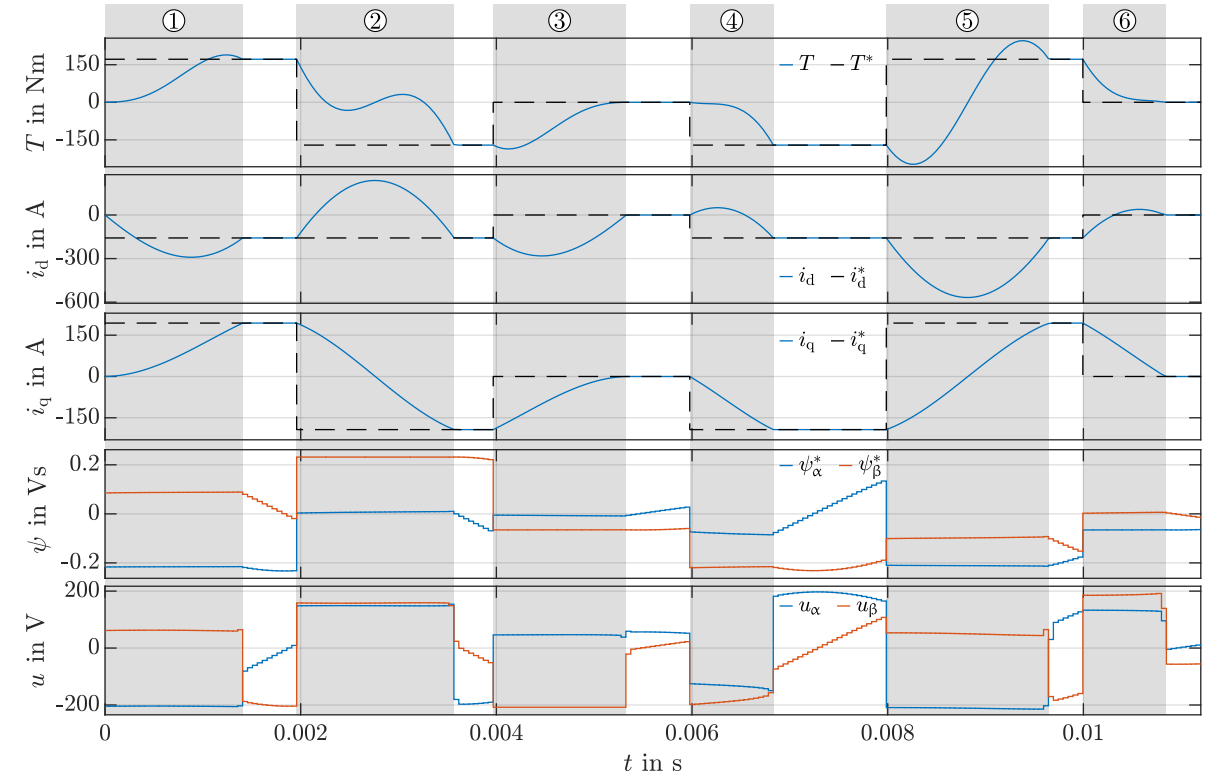

(a) Time courses

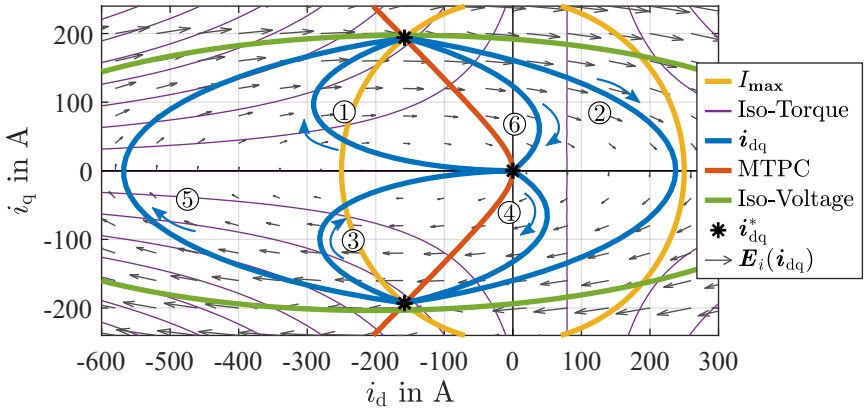

(b) Current trajectories

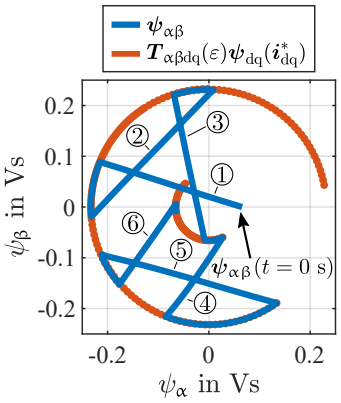

(c) Flux linkage trajectories

Fig. 5.5: Exemplary trajectories with the RPR ($t_{\mathrm{thresh}} = 1.5T_{\mathrm{s}}$, $N = 10$), the DBFC law (3.8), and the initial condition $\varepsilon(t = 0\,\mathrm{s}) = 0$ at $n_{\mathrm{me}} = 2750\,\mathrm{min}^{-1}$ [7, Fig. 3]

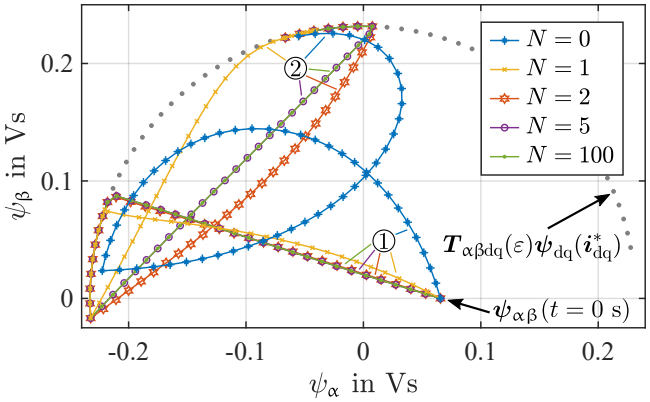

Fig. 5.6: Flux linkage trajectories for the transients ① and ② of the scenario shown in Fig. 5.5 for $N = \{0; 1; 2; 5; 100\}$ [7, Fig. 4]

5.2 Current Constraints

Although the OPC selects operating points $\boldsymbol{i}^*_{\mathrm{dq}}$ within the current limit I_{max}, this limit can be violated during transient operation, see Fig. 5.5b. This can lead to thermal overload or increased thermal cycling of the inverter semiconductors due to their small thermal time constants. To prevent this, a dynamic current limit $I_{\mathrm{max,dyn}}$ is introduced for the CCS-MPFC. The dynamic current limit is a tuning parameter and must satisfy $I_{\mathrm{max,dyn}} \geq I_{\mathrm{max}}$, cf. Fig. 5.7a.

Including a circular current constraint for the predicted current $\boldsymbol{i}_{\mathrm{dq}}[k+1]$ in the CCS-MPFC would lead to an optimization problem with quadratic inequality constraints. Since these would increase the computational burden compared to linear inequality constraints, the circular dynamic current constraint $I_{\mathrm{max,dyn}}$ is approximated by a linear time-varying current constraint, see Fig. 5.7a. This current constraint can be formulated as a linear inequality constraint

$$\frac{(\boldsymbol{i}_{\mathrm{dq}}[k])^{\intercal}}{\|\boldsymbol{i}_{\mathrm{dq}}[k]\|}\boldsymbol{i}_{\mathrm{dq}}[k+1] \leq I_{\mathrm{max,dyn}} \tag{5.9}$$

for the predicted current $\boldsymbol{i}_{\mathrm{dq}}[k+1]$. To avoid non-monotonic torque dynamics due to positive i_{d} currents, as it can be seen in the operating point change ② in Fig. 5.5b, an additional linear current constraint

$$i_{\mathrm{d}}[k+1] \leq i_{\mathrm{d,max}} \tag{5.10}$$

with the tuning parameter $i_{\mathrm{d,max}} \geq 0\,\mathrm{A}$ must be added for IPMSMs and SynRMs, see Fig. 5.7a. Both current constraints (5.9) and (5.10) can be rewritten in matrix-vector notation:

$$\underbrace{\begin{bmatrix} 1 & 0 \\ i_{\mathrm{d}}[k] & i_{\mathrm{q}}[k] \end{bmatrix}}_{\boldsymbol{\mathcal{A}}_{\mathcal{I}}[k]} \boldsymbol{i}_{\mathrm{dq}}[k+1] \leq \underbrace{\begin{bmatrix} i_{\mathrm{d,max}} \\ I_{\mathrm{max,dyn}}\|\boldsymbol{i}_{\mathrm{dq}}[k]\| \end{bmatrix}}_{\boldsymbol{b}_{\mathcal{I}}[k]}. \tag{5.11}$$

To solve the optimization problem of the CCS-MPFC (3.5), the inequality constraint (5.11) for the predicted current $\boldsymbol{i}_{\mathrm{dq}}[k+1]$ must be mapped to the input and optimization variable $\boldsymbol{u}_{\alpha\beta}[k]$. This can be done by inserting the current prediction model (2.11) with the momentary current $\boldsymbol{i}_{\mathrm{dq}}[k]$ into (5.11):

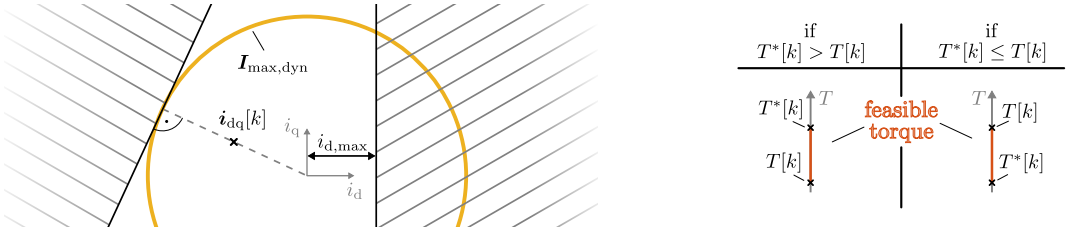

(a) Current constraints **(b)** Torque constraints

Fig. 5.7: State constraints [8, Fig. 5]

$$\begin{aligned} &\boldsymbol{\mathcal{A}}_{\mathcal{I}}[k]\underbrace{\left(\boldsymbol{A_i}[k]\boldsymbol{i}_{\mathrm{dq}}[k]+\boldsymbol{B_i}[k]\boldsymbol{u}_{\mathrm{dq}}[k]+\boldsymbol{E_i}[k]\right)}_{\boldsymbol{i}_{\mathrm{dq}}[k+1]} \leq \boldsymbol{b}_{\mathcal{I}}[k] \\ \Leftrightarrow\ &\underbrace{\boldsymbol{\mathcal{A}}_{\mathcal{I}}[k]\boldsymbol{B_i}[k]\boldsymbol{T}_{\mathrm{dq\alpha\beta}}\left(\varepsilon[k]\right)}_{\boldsymbol{\mathcal{A}}'_{\mathcal{I}}[k]}\boldsymbol{u}_{\alpha\beta}[k] \leq \underbrace{\boldsymbol{b}_{\mathcal{I}}[k]-\boldsymbol{\mathcal{A}}_{\mathcal{I}}[k]\left(\mathrm{A}[k]\boldsymbol{i}_{\mathrm{dq}}[k]+\boldsymbol{E_i}[k]\right)}_{\boldsymbol{b}'_{\mathcal{I}}[k]}. \end{aligned} \tag{5.12}$$

5.3 Torque Constraints

To prevent both torque overshoot and undershoot, and to ensure monotonic torque trajectories during transients, the predicted torque $T[k+1]$ must satisfy

$$T[k] \leq T[k+1] \leq T^*[k] \text{ if } T[k] \leq T^*[k] \tag{5.13}$$

or

$$T[k] \geq T[k+1] \geq T^*[k] \text{ if } T[k] > T^*[k]. \tag{5.14}$$

Both conditions (5.13) and (5.14) can be considered with

$$\operatorname{sign}\left(T^*[k]-T[k]\right)T[k+1] \leq \operatorname{sign}\left(T^*[k]-T[k]\right)T^*[k] \tag{5.15}$$

and

$$\operatorname{sign}\left(T^*[k]-T[k]\right)T[k+1] \geq \operatorname{sign}\left(T^*[k]-T[k]\right)T[k]. \tag{5.16}$$

Furthermore, (5.15) and (5.16) can be rewritten in vector notation:

$$\underbrace{\operatorname{sign}\left(T^*[k]-T[k]\right)\begin{bmatrix}1\\-1\end{bmatrix}}_{\boldsymbol{\mathcal{A}}_{\mathcal{T}}[k]}T[k+1] \leq \underbrace{\operatorname{sign}\left(T^*[k]-T[k]\right)\begin{bmatrix}T^*[k]\\-T[k]\end{bmatrix}}_{\boldsymbol{b}_{\mathcal{T}}[k]}. \tag{5.17}$$

Similar to the current constraint (5.11), the torque constraint (5.17) must be mapped to the optimization variable $\boldsymbol{u}_{\alpha\beta}[k]$ of the CCS-MPFC (3.5). This is achieved by inserting the torque prediction model (2.15) with the momentary estimated torque $T[k]$ into (5.17):

$$\begin{aligned} &\underbrace{\boldsymbol{\mathcal{A}}_{\mathcal{T}}[k]\boldsymbol{B}_T[k]\boldsymbol{T}_{\mathrm{dq\alpha\beta}}\left(\varepsilon[k]\right)}_{\boldsymbol{\mathcal{A}}'_{\mathcal{T}}[k]}\boldsymbol{u}_{\alpha\beta}[k] \leq \underbrace{\boldsymbol{b}_{\mathcal{T}}[k]-\boldsymbol{\mathcal{A}}_{\mathcal{T}}[k]\left(\boldsymbol{A}_T T[k]+\boldsymbol{E}_T[k]\right)}_{\boldsymbol{b}'_{\mathcal{T}}[k]}. \end{aligned} \tag{5.18}$$

5.4 Continuous Control Set Model Predictive Flux Control With State Constraints

The optimization problem of the CCS-MPFC (3.5) extended with state constraints to consider torque and current limits is given by

$$\min_{\boldsymbol{u}_{\alpha\beta}[k]} \|\hat{\boldsymbol{\psi}}_{\alpha\beta}[k+1] - \boldsymbol{\psi}^*_{\alpha\beta}[k+1]\|^2 \tag{5.19a}$$

$$\text{s.t.} \quad \hat{\boldsymbol{\psi}}_{\alpha\beta}[k+1] = \boldsymbol{A}_{\psi}\hat{\boldsymbol{\psi}}_{\alpha\beta}[k] + \boldsymbol{B}_{\psi}\boldsymbol{u}_{\alpha\beta}[k] + \boldsymbol{E}_{\psi}[k], \tag{5.19b}$$

$$\boldsymbol{\mathcal{A}}'_{\mathcal{I}}[k]\boldsymbol{u}_{\alpha\beta}[k] \leq \boldsymbol{b}'_{\mathcal{I}}[k], \tag{5.19c}$$

$$\boldsymbol{\mathcal{A}}'_{\mathcal{T}}[k]\boldsymbol{u}_{\alpha\beta}[k] \leq \boldsymbol{b}'_{\mathcal{T}}[k], \tag{5.19d}$$

$$\boldsymbol{\mathcal{A}}_{\mathcal{U}}\boldsymbol{u}_{\alpha\beta}[k] \leq \boldsymbol{b}_{\mathcal{U}}[k]. \tag{5.19e}$$

Here, the cost function (5.19a), the prediction model (5.19b), and the input constraints (5.19e) are the same as for the CCS-MPFC (3.5). However, the flux linkage reference $\boldsymbol{\psi}^*_{\alpha\beta}[k+1]$ for the state-constrained CCS-MPFC (5.19) is pre-rotated by the RPR which is not the case for the CCS-MPFCs of the baseline control scheme given in Ch. 3 and the extension to the overmodulation range in Ch. 4. Furthermore, the state constraints (5.19c) and (5.19d) were softened with the help of a slack variable to ensure feasibility of the optimization problem [93, 94].

5.5 Simulative Investigation

On the basis of a simulation, the presented TOC method considering torque and current limits (RPR combined with the CCS-MPFC of Sec. 5.4) is investigated. The linearly magnetized IPMSM model characterized by Tab. A.2 is applied for this study. The simulation setup is described in App. A. The parameters of the RPR and the current constraints are listed in Tab. 5.1. Since the discrete-time controller is synchronized with the SVM, the current, torque, and flux ripples induced by the switching of the inverter are not visible in the following figures.

Based on torque step responses, the transient control performance of the proposed method is analyzed for different initial rotation angles $\varepsilon(t = 0\,\mathrm{s})$ and different constant speeds. To illustrate the working principle of the presented control method, an exemplary video animation is available in [95] for the same scenario as depicted in Fig. 5.5.

5.5.1 Initial Rotor Angle Investigation

Due to the voltage constraint (5.19e) and the cost function (5.19a) of the CCS-MPFC (5.19), the corners (elementary vectors) of the voltage hexagon are preferred as input variables $\boldsymbol{u}_{\alpha\beta}$ during transients, since they often reduce the cost function the most as long as torque (5.19d) and current constraints (5.19c) are not active. For this reason, not only the flux linkage trajectory in the $\alpha\beta$ coordinate system depends on the initial rotor angle during transients but also the current trajectories in the dq coordinate system and the torque, see Fig. 5.8. Nevertheless, similar settling times for the torque are achieved without overshoots as well as undershoots and without violating the dynamic current limit $I_{\mathrm{max,dyn}}$, see Fig. 5.8a and Fig. 5.8b. In Fig. 5.8c, the flux linkage trajectories for a step response to the rated torque are shown for equidistantly distributed initial rotor angles $\varepsilon_0 = \varepsilon(t = 0\,\mathrm{s})$ from 0 to $\pi/3$. Here, the flux linkage trajectory for $\varepsilon_0 = 0$ is

Tab. 5.1: Parameters of proposed TOC method (state-constrained CCS-MPFC with RPR) and the PI-FOC

Presented TOC method		
Number of RPR iterations	N	5
Time threshold	t_{thresh}	$1.5T_{\mathrm{s}}$
Dynamic current limit	$I_{\mathrm{max,dyn}}$	270 A
D-axis current limit	$i_{\mathrm{d,max}}$	20 A
PI-FOC		
Controller design	Magnitude optimum	
Dynamic overmodulation scheme	Minimum distance error [83]	
Anti-reset windup method	Back-calculation [96]	

equal to the trajectory for $\varepsilon_0 = \pi/3$ rotated by an angle of $-\pi/3$ due to the symmetry of the voltage hexagon which results in identical dq current and torque trajectories.

5.5.2 Speed Dependency Investigation

Since the pre-rotation of the flux linkage reference depends on the angular velocity ω, the transient trajectories of torque and dq current differ during transient operation for different machine speeds n_{me} even for an identical initial rotor angle ε_0 and identical torque reference trajectories, see Fig. 5.9. Here, step responses to maximum and minimum torque are commanded. For speeds of $n_{\mathrm{me}} = \{0, 2750\}\ \mathrm{min}^{-1}$ the maximum and minimum machine torque can be realized. However, for a speed of $n_{\mathrm{me}} = 13\,000\,\mathrm{min}^{-1}$, the OPC selects the intersections of the voltage limit and the MTPV curve as operating points $\boldsymbol{i}_{\mathrm{dq}}^{*}$ which results in reduced torque values (flux weakening operation) compared to the rated operating point, see Fig. 5.9b. Nevertheless, the maximum and minimum possible torques are achieved.

Although the initial dq current $\boldsymbol{i}_{\mathrm{dq}}(t = 0\,\mathrm{s}) = \mathbf{0}\,\mathrm{A}$ is outside the voltage limit for $n_{\mathrm{me}} = 13\,000\,\mathrm{min}^{-1}$ and, thus, a torque undershoot is inevitable, the optimization problem of the CCS-MPFC (5.19) remains feasible due to its softened state constraints ((5.19c) and (5.19d)) and a solution is found that limits the torque undershoot.

5.5.3 Time-Optimality Investigation

As a result of the state constraints, the possible state trajectories during transient operation are restricted. To empirically investigate whether the application of the presented TOC method leads to time-optimal trajectories even with active state constraints, the control performance is compared to a TOC with the same torque and current constraints. This TOC with state constraints considers the entire future state and input trajectory during transient operation to minimize the time to reach the reference operating point $\boldsymbol{i}_{\mathrm{dq}}^{*}$, i.e., its prediction horizon is practically infinite. The resulting nonlinear constrained optimization problem was solved by the direct method, cf. Sec. 2.5, with a sequential quadratic programming (SQP) algorithm of the Matlab optimization toolbox. This is feasible for an offline simulation comparison, but of course the computational complexity of the TOC solution is far greater than the one-step prediction required to solve the QP problem of the state-constrained CCS-MPFC with the pre-rotated flux linkage reference.

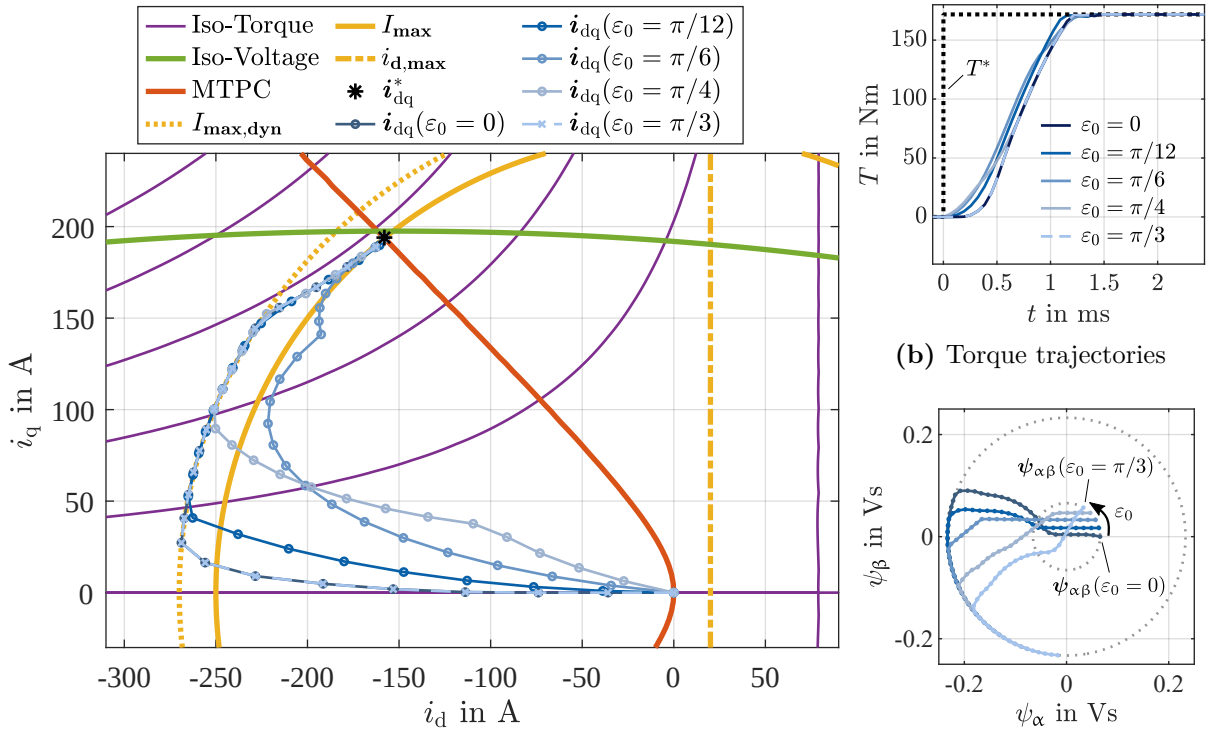

(a) Current trajectories **(b)** Torque trajectories **(c)** Flux trajectories

Fig. 5.8: Simulative trajectories for different initial rotor angles $\varepsilon(t = 0\,\mathrm{s}) = 0$ at $n_{\mathrm{me}} = 2750\,\mathrm{min}^{-1}$ [7, Fig. 6]

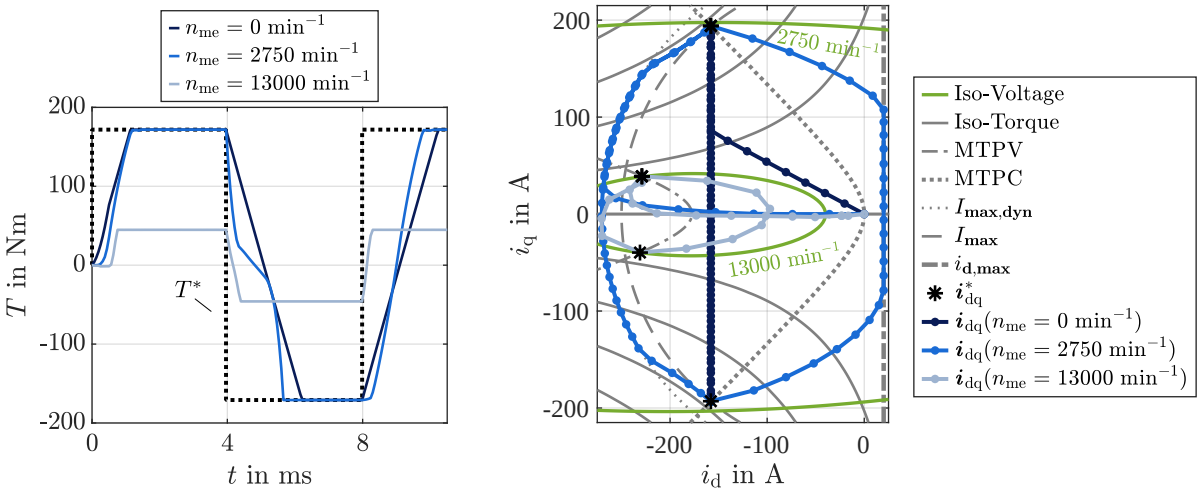

(a) Torque trajectories **(b)** Current trajectories

Fig. 5.9: Simulative TO-MPC trajectories for maximum and minimum torque operation for different speeds n_{me} with an initial rotor angle $\varepsilon(t = 0\,\mathrm{s}) = 0$ [7, Fig. 7]

The sampling instants required to perform the operating point changes of Fig. 5.5 for the presented method and the TOC with state constraints are listed in Tab. 5.2. Here, the presented method achieves the same transient control performance as the state constrained TOC. Thus, empirical evidence is provided that the presented method achieves the same transient performance as the direct TOC approach at a significantly reduced computational cost (one-step vs. unlimited prediction steps).

Furthermore, the required sampling instants for the TOC without state constraints are listed in Tab. 5.2. This TOC corresponds to the DBFC law (3.8). It can be seen that only for the operating point changes ② and ⑤ the required sampling steps are reduced compared to the TOC with state constraints and the presented method for the price of unintended transient current and torque trajectories, cf. Fig. 5.5.

Tab. 5.2: Required sampling instants to conduct the operating point changes defined in Fig. 5.5 for TOC with and without state constraints as well as the proposed method (state constrained CCS-MPFC with RPR) for $T_\mathrm{s} = 62.5\,\mu\mathrm{s}$, $\varepsilon(t = 0\,\mathrm{s}) = 0$, $n_\mathrm{me} = 2750\,\mathrm{min}^{-1}$, $I_\mathrm{max,dyn} = 270\,\mathrm{A}$, $i_\mathrm{d,max} = 20\,\mathrm{A}$

Operating point change	①	②	③	④	⑤	⑥
TOC w/o state constraints (DBFC (3.8) with RPR)	23	26	22	14	28	14
TOC w/ state constraints (quasi-infinite horizon)	23	30	22	14	33	14
Proposed TOC method (CCS-MPFC (5.19) with RPR)	23	30	22	14	33	14

5.5.4 Comparison to State-of-the-Art Methods

In this section, the control performance of the presented method is compared with the state-of-the-art continuous control set methods of PI-FOC, RRCC [19], and the CCS-MPFC (3.5) without state constraints and without RPR. Within this section, the presented method (state-constrained CCS-MPFC with RPR) is referred to as time-optimal model predictive control (TO-MPC) to avoid confusion with the CCS-MPFC (3.5).

The parameters of the decoupled PI-FOC current controllers are listed in Tab. 5.1. Unlike the PI-FOC, the RRCC and CCS-MPFC (3.5) do not contain any tuning parameters. All controllers are sampled with $T_\mathrm{s} = 62.5\,\mu\mathrm{s}$ and synchronized with the SVM in the same way as the TO-MPC.

For this comparison, the same reference torque trajectory is selected as in Fig. 5.9a, consisting of steps to rated motor and generator operation at a speed of $n_\mathrm{me} = 2750\,\mathrm{min}^{-1}$ with an initial rotor angle $\varepsilon(t = 0\,\mathrm{s}) = 0$. The resulting torque and current trajectories for the TO-MPC, PI-FOC, RRCC, and CCS-MPFC are shown in Fig. 5.10. Since the PI-FOC and CCS-MPFC do not consider the torque and current constraints, overcurrents as well as torque overshoots and undershoots cannot be avoided. Furthermore, increased settling times of the PI-FOC and CCS-MPFC can be observed, especially for the transients starting at $t = 0\,\mathrm{ms}$ and $t = 8\,\mathrm{ms}$ compared to the TO-MPC and RRCC. For the transient starting at $t = 0\,\mathrm{ms}$ from zero torque to rated torque, the proposed TO-MPC requires 1.2 ms, the PI-FOC 3.6 ms, and the CCS-MPFC (3.5) 2.8 ms to reach the reference torque which represents a reduction of 67 % and 57 % in settling time for this representative torque transient compared to PI-FOC and the CCS-MPFC (3.5).

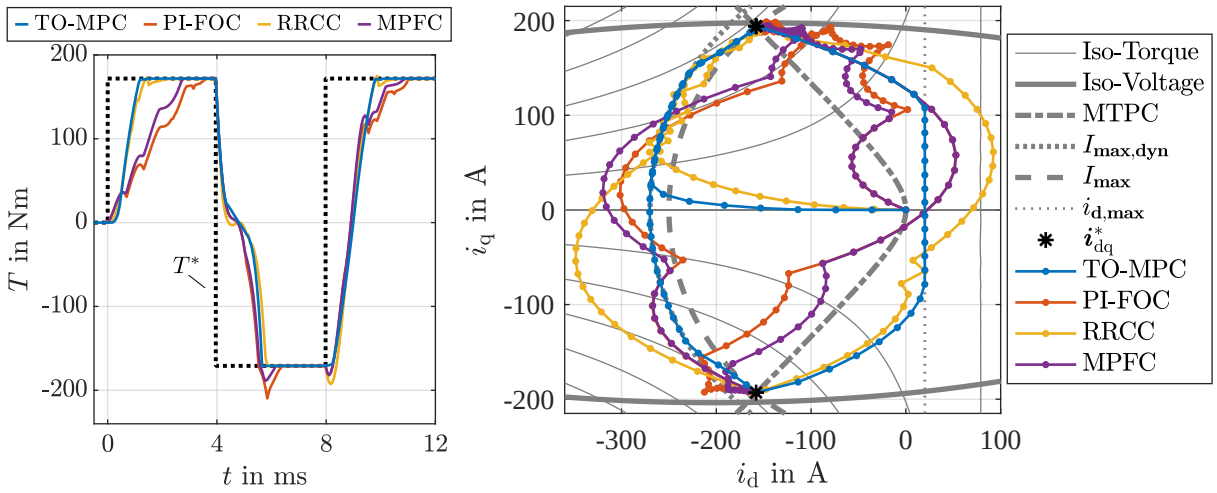

(a) Torque trajectories

(b) Current trajectories

Fig. 5.10: Simulative trajectories at a speed of $n_{\mathrm{me}} = 2750\,\mathrm{min}^{-1}$ with an initial rotor angle $\varepsilon(t = 0\,\mathrm{s}) = 0$ [7, Fig. 8]

Since the CCS-MPFC results in the same control behavior as the deadbeat controller (3.8) with the minimum distance error dynamic overmodulation scheme [83], the settling time reduction of 57 % for the transient to rated torque is valid for the deadbeat control law (3.8) without RPR as well. The RRCC and the TO-MPC achieve similarly fast settling times because both use a pre-rotation of the reference flux linkage. However, the RRCC only heuristically accounts for current and torque constraints and, therefore, cannot guarantee the prevention of overcurrents and torque overshoots and undershoots.

5.6 Experimental Investigation

To experimentally investigate the presented control strategy consisting of RPR and state-constrained CCS-MPFC, several representative experiments are shown in the following. The description of the experimental setup is provided in App. B. The controller parameters of the overall control scheme are listed in Tab. 5.3.

The turnaround times of the OPC, GFO, RPR, CCS-MPFC, auxiliary functions and the overall control strategy are listed in Tab. 5.4. Here, the low computational load of the RPR with an iteration number of $N = 5$ can be seen. The turnaround time reported for the auxiliary functions cover, e.g., SVM, coordinate transformations, analog-digital conversion, as well as processor and host computer communication that must be executed in addition to the OPC, GFO, RPR, and CCS-MPFC, are summarized. Compared to the other parts of the overall control scheme, the CCS-MPFC requires a variable number of computational steps per controller sample. This is due to the varying number of iteration steps required for the embedded activ-set solver applied, cf. [97, 98], to find the global optimum of the QP (5.19). To reduce the number of iterations of the active-set solver, the solution of the previous sampling instant was used as the initial solution guess (hot start). Furthermore, in simulations and experiments it was not observed that more than 11 iterations were needed to find the optimum. Therefore, the required turnaround time of

1.2-10.5 µs corresponds to 1-11 iterations and leads to a varying turnaround time of the entire control strategy of 43.4-52.7 µs, see Tab. 5.4.

Tab. 5.3: Controller parameters

RPR		
Number of RPR iterations	N	5
Time threshold	t_{thresh}	$1.5T_{\mathrm{s}}$
Dynamic current limit	$I_{\mathrm{max,dyn}}$	270 A
D-axis current limit	$i_{\mathrm{d,max}}$	30 A
GFO		
Damping ratio	ξ	1
Characteristic frequency	ω_0	$1492\,\mathrm{s}^{-1}$
FMC		
Low-pass filter time constant	τ	20 ms
Speed threshold	ω_{fmc}	$270\,\mathrm{s}^{-1}$

Tab. 5.4: Turnaround times of the proposed TOC method (state-constrained CCS-MPFC with RPR)

	Turnaround time in µs
OPC	8.4
FMC	1.3
GFO	2.3
RPR	0.9
CCS-MPFC	1.2-10.5
Auxiliary functions	29.3
Overall control strategy	43.4-52.7

5.6.1 Initial Rotor Angle Investigation

In Fig. 5.11, the trajectories for a step response to the rated torque are depicted for equidistantly distributed initial rotor angles $\varepsilon_0 = \varepsilon(t = 0\,\mathrm{s})$ from 0 to $\pi/3$ at rated speed. Here, torque over- and undershoots as well as overcurrents are prevented. Due to non-ideal effects such as parameter and model inaccuracies or measurement noise, prediction errors may result in slight violations of the torque and current constraints. However, these violations can be considered minor. Similar to the simulative investigation in Sec. 5.5.1 for the linearly magnetized IPMSM, the current trajectories differ for different initial rotor angles for the nonlinearly magnetized IPMSM with significant cross saturation, cf. Fig. 5.11a. However, the resulting torque trajectories are similar for different initial rotor angles, see Fig. 5.11b.

5.6.2 Speed Dependency Investigation

The torque and current trajectories for torque reference steps to rated motor and generator operation for different speeds in the entire speed range from standstill to maximum speed are

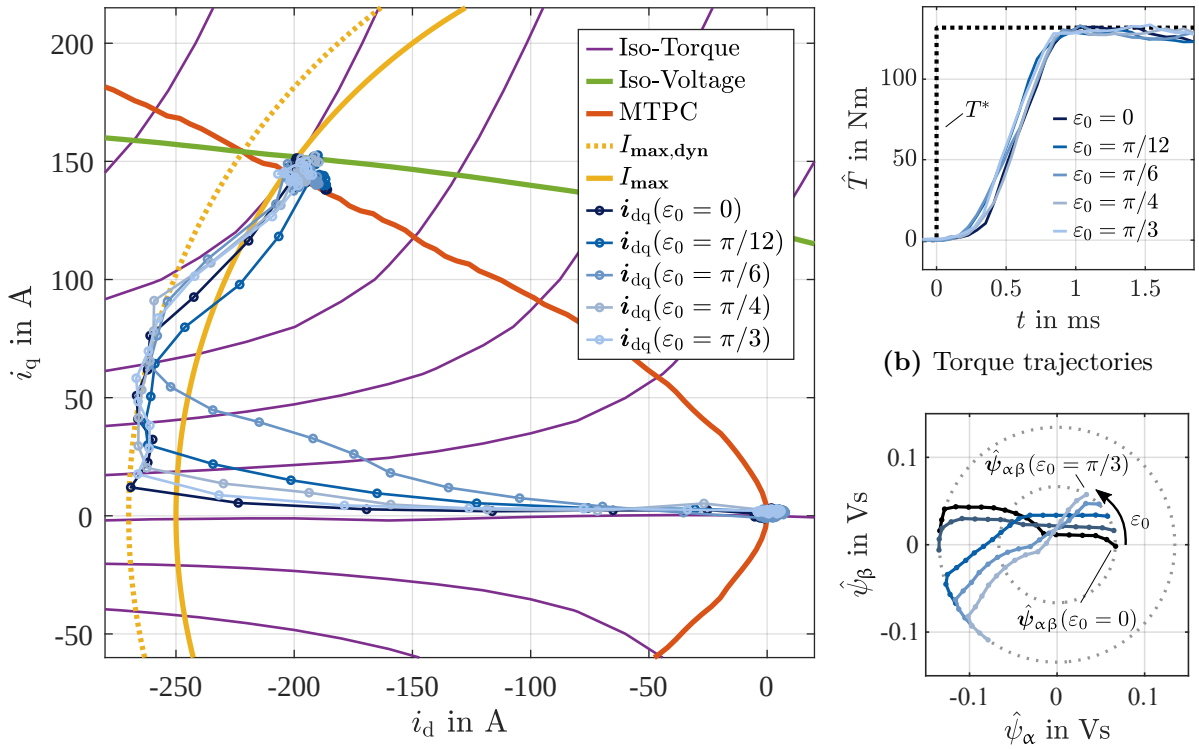

(a) Current trajectories

(b) Torque trajectories

(c) Flux trajectories

Fig. 5.11: Experimental step response trajectories to maximum torque for different initial rotor angles $\varepsilon(t = 0\,\mathrm{s})$ at $n_{\mathrm{me}} = 4750\,\mathrm{min}^{-1}$ [7, Fig. 12]

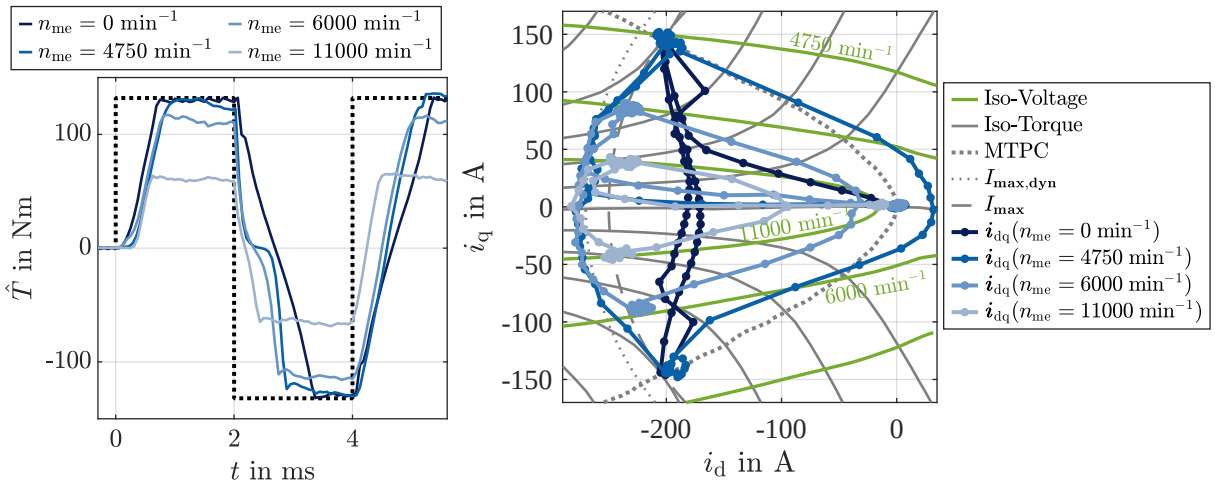

(a) Torque trajectories

(b) Current trajectories

Fig. 5.12: Experimental trajectories for maximum and minimum torque operation for different speeds n_{me} with an initial rotor angle $\varepsilon(t = 0\,\mathrm{s}) = 0$ [7, Fig. 13]

shown in Fig. 5.12. Due to the voltage limit for $n_{\mathrm{me}} = \{6000, 11000\}\ \mathrm{min}^{-1}$, the rated torque can no longer be achieved, see Fig. 5.12a. Nevertheless, the OPC ensures that the maximum and minimum possible torques are achieved for the corresponding speed. Due to the nonlinear magnetization, there are no section-wise linear current trajectories at standstill compared to the current trajectories of the IPMSM with linear magnetization, see Fig. 5.9b.

5.6.3 Dynamic Current Limit Investigation

The state constraints ensure that all selected voltages $\boldsymbol{u}_{\alpha\beta}$ respect the dynamic current limit $I_{\mathrm{max,dyn}}$. Therefore, the dynamic current limit $I_{\mathrm{max,dyn}}$ restricts the set of feasible voltages $\boldsymbol{u}_{\alpha\beta}$ during transient operation at the current limit, the more, the smaller $I_{\mathrm{max,dyn}}$ is chosen. To investigate the influence of the dynamic current limit, the torque, current, and flux linkage trajectories are depicted in Fig. 5.13 for torque reference steps to rated motor and generator operation at $n_{\mathrm{me}} = 4750\,\mathrm{min}^{-1}$. Here, slightly reduced torque settling times can be observed for increased dynamic current limits $I_{\mathrm{max,dyn}}$, as the current trajectories reach the iso-torque loci earlier, see Fig. 5.13b. However, the flux linkage reference operating points are reached with similar settling times, see Fig. 5.13c and Fig. 5.13d. During the transient from the rated generator to the motor operating point at about 4 ms, there are current samples near the d-axis that are slightly below and above the dynamic current limit $I_{\mathrm{max,dyn}}$. This deviation of the current trajectory from the dynamic current limit can be explained by prediction errors of the current prediction model (2.11) due to the rapidly changing differential inductance L_{qq}, cf. Fig. A.3.

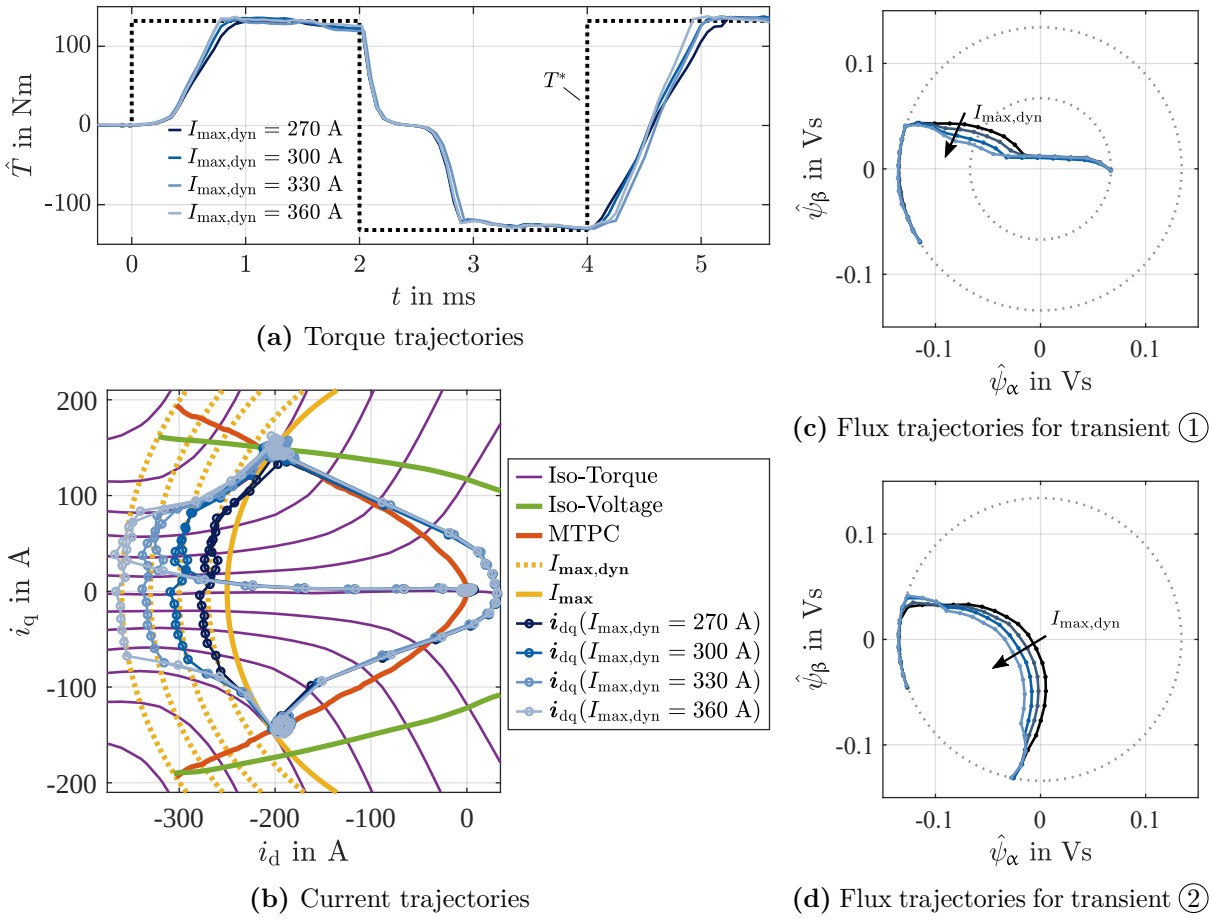

(a) Torque trajectories

(b) Current trajectories

(c) Flux trajectories for transient ①

(d) Flux trajectories for transient ②

Fig. 5.13: Experimental step response trajectories to maximum torque for different dynamic current limits $I_{\mathrm{max,dyn}}$ at a speed of $n_{\mathrm{me}} = 4750\,\mathrm{min}^{-1}$ with an initial rotor angle $\varepsilon(t = 0\,\mathrm{s}) = 0$ [7, Fig. 14]

6 Time-Optimal Control in the Whole Modulation Range

The following chapter is based on the own publication [8]. The author of this thesis contributed the main parts of [8], in particular, the proposed control method concept as well as the simulative and experimental investigations. He also prepared the publication independently, while the contributions of the other co-authors were limited to technical discussions during the investigation phase as well as proofreading of the manuscript. Therefore, parts of the following text have been taken in modified or unmodified form from the mentioned publication. For the sake of readability, the underlying self-citations are not explicitly listed in the following.

In this chapter, the time-optimal harmonic reference generator (TO-HRG) scheme is presented. The TO-HRG enables TOC performance in the whole speed and modulation range without transient overcurrents as well as torque overshoots and undershoots. To achieve this, the TO-HRG manipulates the flux linkage reference of the CCS-MPFC (5.19) with state constraints. This manipulation includes a pre-rotation of the reference during transient operation to achieve TOC performance. It also adds a harmonic content to the flux linkage reference during steady-state operation in the overmodulation range to provide a seamless transition to the overmodulation range. The TO-HRG incorporates the RPR method presented in Ch. 5 and the HRG method presented in Ch. 4 and combines both to achieve their respective advantages. Thus, the TO-HRG can be considered as an extension of the method presented in Ch. 5 to the overmodulation range, or as a maximization of the control dynamics of the HRG method presented in Ch. 4, taking into account current and torque limits. Due to the previously mentioned control characteristics, the overall control scheme depicted in Fig. 6.1 fully utilizes the drive's potential during steady-state and transient operation.

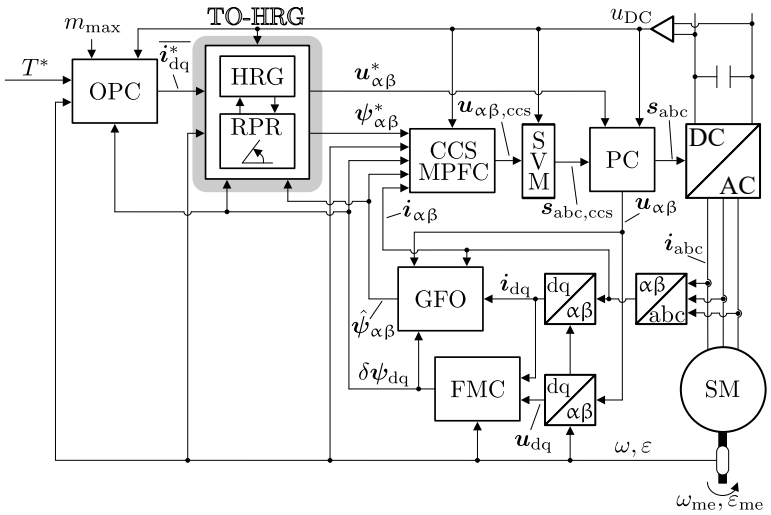

Fig. 6.1: Overall control scheme (gray shaded part is the focus of Ch. 6) [8, derivate of Fig. 3]

6.1 Time-Optimal Harmonic Reference Generator

The calculation steps that must be executed by the TO-HRG can be classified into three subroutines, cf. Fig. 6.2:

1. Calculation of the harmonic flux linkage reference content $\widetilde{\boldsymbol{\psi}}^*_{\alpha\beta}(\varepsilon[k])$,
2. Calculation of the pre-rotation angle $\varepsilon_{\mathrm{rpr}}[k]$ of the flux linkage reference,
3. Calculation of the voltage $\boldsymbol{u}^*_{\alpha\beta}[k]$ for the PC scheme and the flux linkage reference $\boldsymbol{\psi}^*_{\alpha\beta}(\varepsilon[k] + \varepsilon_{\mathrm{rpr}}[k])$.

In the following, these categories are explained in more detail.

6.1.1 Calculation of the Harmonic Flux Reference Content

The RPR can only be applied when the flux linkage reference rotates circularly for a constant mean reference current $\overline{\boldsymbol{i}^*_{\mathrm{dq}}}$. This is only true in the linear modulation range. Instead, in the overmodulation region, additional harmonics occur that would result in a non-circular shape of the flux linkage trajectory. Therefore, the RPR of Ch. 5 cannot be applied directly in the overmodulation region.

However, the RPR can still be used in the overmodulation range by subtracting the harmonic content of the reference flux linkage $\widetilde{\boldsymbol{\psi}}^*_{\alpha\beta}(\varepsilon[k])$ from the reference flux linkage $\boldsymbol{\psi}^*_{\alpha\beta}(\varepsilon[k])$ and the momentary flux linkage $\boldsymbol{\psi}_{\alpha\beta}[k]$, cf. Fig. 6.3, because the reference flux linkage without its harmonic content rotates circularly, see Fig. 6.2. The harmonic content of the reference flux linkage is calculated by

$$\widetilde{\boldsymbol{\psi}}^*_{\alpha\beta}(\varepsilon[k]) = \boldsymbol{\psi}^*_{\alpha\beta}(\varepsilon[k]) - \underbrace{\boldsymbol{T}_{\alpha\beta\mathrm{dq}}(\varepsilon[k])\overline{\boldsymbol{\psi}^*_{\mathrm{dq}}}}_{\overline{\boldsymbol{\psi}^*_{\alpha\beta}}(\varepsilon[k])}. \tag{6.1}$$

Here, the flux linkage reference $\boldsymbol{\psi}^*_{\alpha\beta}(\varepsilon[k])$ is calculated with the HRG described in Ch. 4.

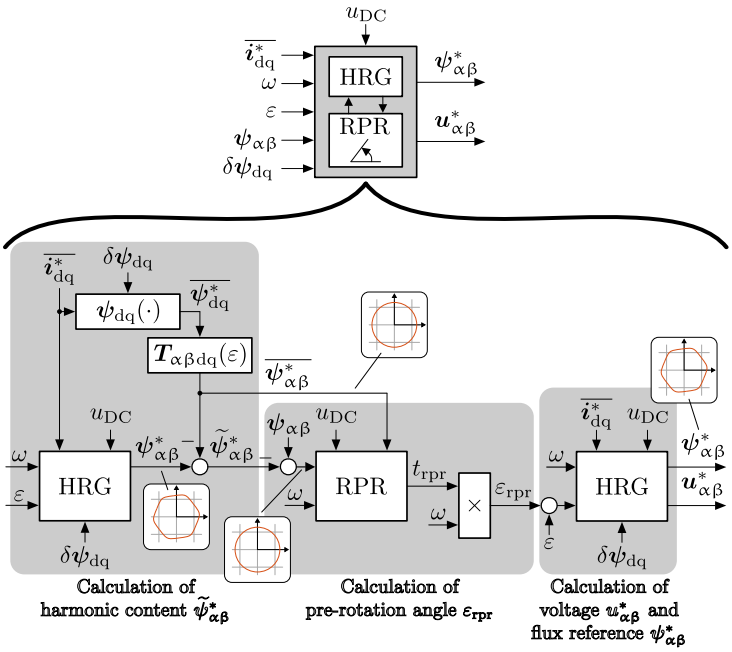

Fig. 6.2: Block diagram of the TO-HRG [8, derivate of Fig. 11]

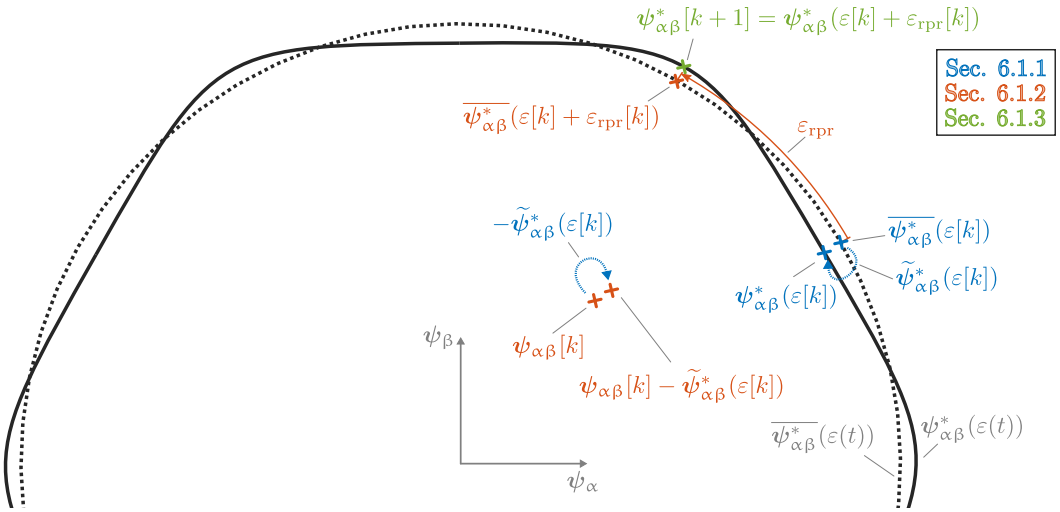

Fig. 6.3: Illustration of the TO-HRG procedure [8, derivate of Fig. 12]

6.1.2 Calculation of the Pre-Rotation Angle

With the mean flux linkage reference $\overline{\boldsymbol{\psi}^*_{\alpha\beta}}(\varepsilon[k])$ and the harmonic content of the flux linkage subtracted from the momentary flux linkage $\boldsymbol{\psi}_{\alpha\beta}[k] - \widetilde{\boldsymbol{\psi}}^*_{\alpha\beta}(\varepsilon[k])$ as inputs, the pre-rotation angle $\varepsilon_{\mathrm{rpr}}[k]$ is calculated with the RPR, cf. Fig. 6.2 and Fig. 6.3. Please note that the pre-rotated mean flux reference $\overline{\boldsymbol{\psi}^*_{\alpha\beta}}(\varepsilon[k] + \varepsilon_{\mathrm{rpr}}[k])$ is shown in Fig. 6.3 for visualization purposes only, but is not required for the implementation of the TO-HRG.

6.1.3 Calculation of the Flux and Voltage Reference

With the pre-rotated angle $\varepsilon[k] + \varepsilon_{\mathrm{rpr}}[k]$ as input of the HRG, cf. Fig. 6.2, the flux linkage reference $\boldsymbol{\psi}^*_{\alpha\beta}[k+1] = \boldsymbol{\psi}^*_{\alpha\beta}(\varepsilon[k] + \varepsilon_{\mathrm{rpr}}[k])$ for the CCS-MPFC (3.5) and the voltage reference $\boldsymbol{u}^*_{\alpha\beta}[k]$ (4.14) for the PC scheme are calculated.

The pre-rotated flux linkage reference $\boldsymbol{\psi}^*_{\alpha\beta}[k+1]$ contains the harmonics induced by the voltage constraints in the overmodulation range and enables TOC performance. Torque overshoots and undershoots as well as overcurrents are not considered by the TO-HRG, but are prevented by the state constraints of the CCS-MPFC.

6.2 Continuous Control Set Model Predictive Flux Control With State Constraints

The CCS-MPFC (5.19) is applied as closed-loop controller combined with the TO-HRG. However, the state-constrained CCS-MPFC (5.19) is intended to control the flux linkage to its steady-state reference within the linear modulation range. Therefore, the resulting current $\boldsymbol{i}_{\mathrm{dq}}[k]$ or flux linkage $\boldsymbol{\psi}_{\mathrm{dq}}[k]$ will always remain within the iso-voltage locus for the end of the linear modulation range ($m = 0.907$). An exemplary iso-voltage locus for ($m = 0.907$) is shown in Fig. 6.4a. If the state of the SM ($\boldsymbol{i}_{\mathrm{dq}}[k]$ or $\boldsymbol{\psi}_{\mathrm{dq}}[k]$) is within the iso-voltage locus for $m = 0.907$, the state can be steered in any direction in the dq plane due to a remaining voltage reserve. Consequently, the torque constraint (5.18) can always be satisfied. In this chapter, the CCS-MPFC (5.19) is extended to operate in the full modulation range. If the state of the SM is outside the iso-voltage locus for $m = 0.907$, the state cannot be continually steered to each direction in the dq plane due to the increased induced voltage and, therefore, the torque constraint (5.18) can no longer be fulfilled always. For this reason, the torque constraint is disabled when the state of the SM is outside the linear modulation iso-voltage locus:

if $\left\| R_{\mathrm{s}} \boldsymbol{i}_{\mathrm{dq}}[k] + \dfrac{\boldsymbol{T}_{\alpha\beta\mathrm{dq}}(T_{\mathrm{s}}\omega[k]) - \boldsymbol{I}_2}{T_{\mathrm{s}}} \boldsymbol{\psi}_{\mathrm{dq}}[k] \right\| \geq \dfrac{u_{\mathrm{DC}}}{\sqrt{3}}$ **then**

    disable torque constraint (5.19d)

else

    enable torque constraint (5.19d)

end if

6.3 Simulative Investigation

The control scheme depicted in Fig. 6.1 is first investigated on the basis of simulation. The linearly magnetized IPMSM model, cf. App. A.1, is applied for this study. The description of the simulation setup is given in App. A.

Based on torque step responses, the transient control performance of the proposed method is analyzed for different initial rotation angles $\varepsilon(t = 0\,\mathrm{s})$ and several stationary speeds. In addition, a comparison is conducted with the HRG method described in Ch. 4 and the time-optimal DBFC method proposed in [16]. The simulation and controller settings are listed in Tab. A.1 and Tab. 6.1.

Tab. 6.1: Controller scheme parameters

Proposed TO-HRG method		
Number of RPR iterations	N	5
Time threshold	t_{thresh}	$1.5T_{\mathrm{s}}$
Dynamic current limit	$I_{\mathrm{max,dyn}}$	280 A
D-axis current limit	$i_{\mathrm{d,max}}$	30 A
Pulse clipping time	T_{c}	15 µs
HRG method, cf. Ch. 4		
Pulse clipping time	T_{c}	15 µs

6.3.1 Initial Rotor Angle Investigation

In Fig. 6.4, the current, torque, and flux trajectories are depicted for uniformly distributed initial rotor angles $\varepsilon_0 = \varepsilon(t = 0\,\mathrm{s}) \in \{0, ..., \pi/3\}$. The flux linkage trajectory for $\varepsilon_0 = 0$ is equal to the trajectory for $\varepsilon_0 = \pi/3$ rotated by an angle of $-\pi/3$ due to the symmetry of the voltage hexagon and, therefore, results in identical dq current and torque trajectories. Since the voltage constraint (voltage hexagon) in the dq frame depends on the rotor angle ε, not only the flux linkage trajectory in the $\alpha\beta$ frame during transients, but also the dq current and torque trajectories depend on the initial rotor angle $\varepsilon_0 = \varepsilon(t = 0\,\mathrm{s})$, see Fig. 6.4. Nonetheless, similar settling times for the torque are achieved without violating the dynamic current limit $I_{\mathrm{max,dyn}}$, see Fig. 6.4a. Furthermore, torque overshoots and undershoots are prevented as long as $\boldsymbol{i}_{\mathrm{dq}}$ is within the linear modulation isovoltage ($m \leq 0.907$). When $\boldsymbol{i}_{\mathrm{dq}}$ enters the region where overmodulation is required, the torque constraints (5.19d) are disabled and the controller can achieve maximum torque at the voltage limit (six-step operation).

6.3.2 Speed Dependency Investigation

Since the pre-rotation angle of the flux linkage reference depends on the rotor speed ω, the transient trajectories of torque and dq current differ during transient operation for different machine speeds n_{me} even for identical initial rotor angles ε_0 and identical torque reference trajectories, see Fig. 6.5. Here, step responses to maximum and minimum torque are commanded. At standstill, the maximum and minimum torque can be realized without additional torque harmonics induced by the voltage limit. Mainly zero voltage vectors $\{s_1, s_8\}$ are selected here during steady-state operation. At the rated speed ($n_{\mathrm{me}} = 3100\,\mathrm{min}^{-1}$) the rated motor operating

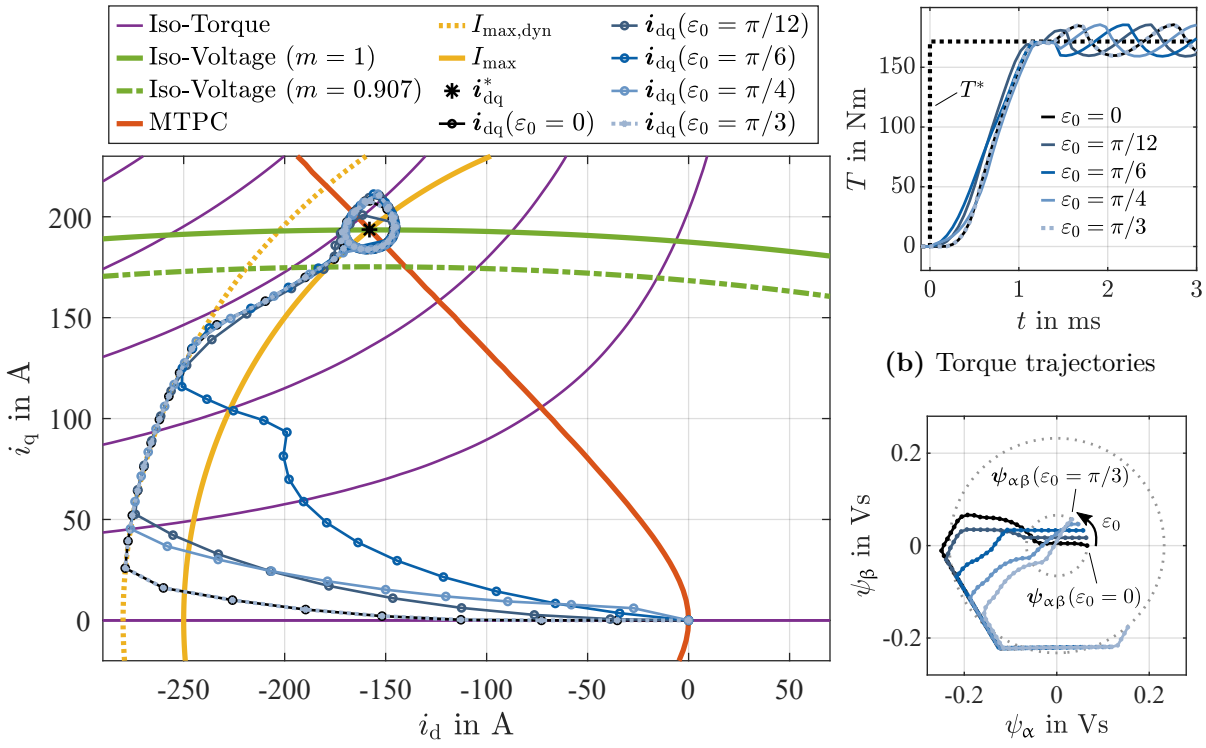

(a) Current trajectories

(b) Torque trajectories

(c) Flux trajectories

Fig. 6.4: Simulative trajectories for different initial rotor angles $\varepsilon(t = 0\,\mathrm{s}) = 0$ at rated speed ($n_{\mathrm{me}} = 3100\,\mathrm{min}^{-1}$) [8, Fig. 13]

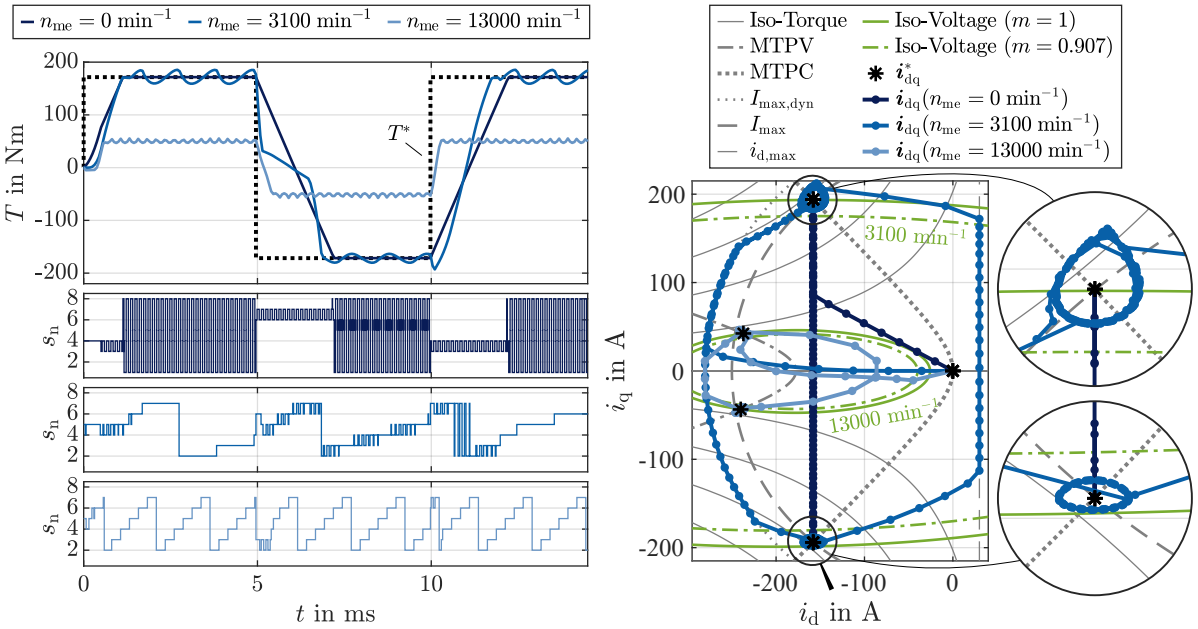

(a) Torque and switching vector trajectories

(b) Current trajectories

Fig. 6.5: Simulative trajectories for maximum and minimum torque operation for different speeds n_{me} with an initial rotor angle $\varepsilon(t = 0\,\text{s}) = 0$ [8, Fig. 14]

point lies on the iso-voltage for $m = 1$. Therefore, six-step operation ($m = 1$) must be utilized to achieve maximum torque operation. Due to the ohmic voltage drop, a slightly reduced voltage is required for minimum torque operation compared to maximum torque operation. In this scenario, a modulation index of $m \approx 0.985$ is sufficient to achieve the rated negative torque operating point at rated speed, resulting in additional switching instants in the range of $t \in [7\,\text{ms}, 10\,\text{ms}]$ during steady-state operation, see Fig. 6.5a. For a speed of $n_{me} = 13\,000\,\text{min}^{-1}$, the OPC selects the intersections of the voltage limit ($m = 1$) and the MTPV trajectory as operating points $\boldsymbol{i}^*_{dq}$ which results in reduced torque magnitudes (flux weakening operation) compared to the rated operating point, cf. Fig. 6.5b. Nevertheless, the maximum and minimum possible torque at the voltage limit is achieved thanks to the ability of the proposed control scheme to operate in six-step mode.

Although the initial dq current $\boldsymbol{i}_{dq}(t = 0\,\text{s}) = \boldsymbol{0}\,\text{A}$ is outside the voltage limit for $n_{me} = 13\,000\,\text{min}^{-1}$ and, thus, a torque undershoot is inevitable, the optimization problem (3.5) of the TO-MPC remains feasible due to its softened state constraints and a solution is found that limits the torque undershoot to the best achievable extent.

6.3.3 Comparison to State-of-the-Art Methods

In this section, the control performance of the proposed control scheme is compared to methods that allow a smooth transition from linear modulation to the entire overmodulation range. For this purpose, the CCS-MPFC and HRG presented in Ch. 4 and the DBFC proposed in [16], which achieves TOC performance, are chosen. Since all three methods achieve the same steady-state

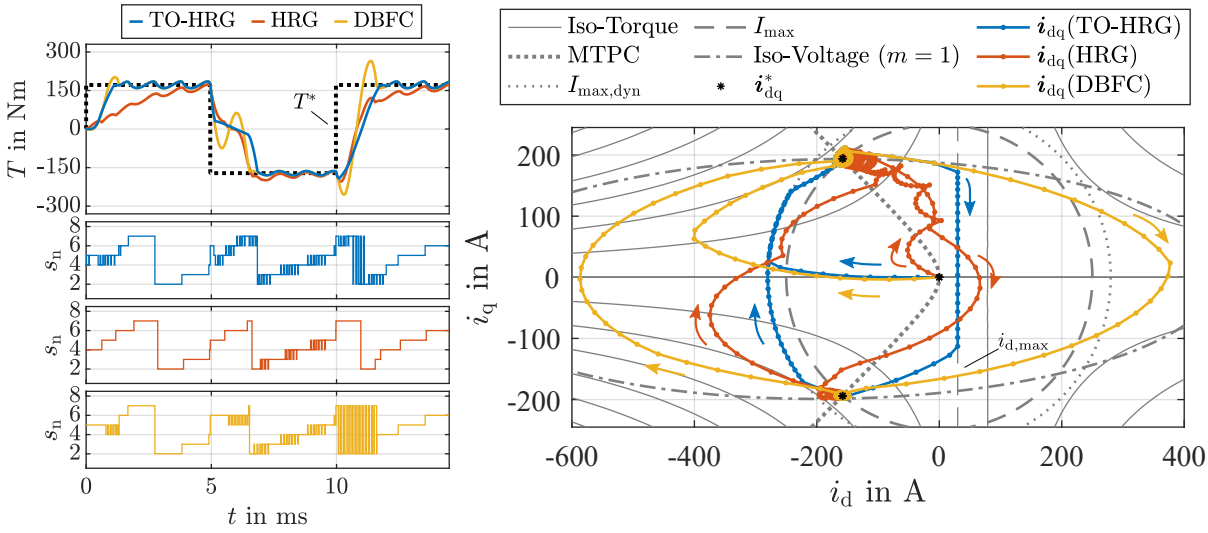

(a) Torque and switching trajectories

(b) Current trajectories

Fig. 6.6: Simulative trajectories of the proposed (TO-HRG) and state-of-the-art methods [6] (HRG), [16] (DBFC) for maximum and minimum torque operation with an initial rotor angle $\varepsilon(t = 0\,\mathrm{s}) = 0$ at rated speed ($n_\mathrm{me} = 3100\,\mathrm{min}^{-1}$) [8, Fig. 15]

control performance, only the transient control performance is investigated. For clarity, the method presented in this chapter will be referred to as TO-HRG and the method presented in Ch. 4 will be referred to as HRG for the experimental and simulative comparison sections of this chapter.

In Fig. 6.6, the trajectories of the TO-HRG, HRG, and DBFC for the challenging torque reference trajectory used for the speed dependency investigation, cf. Fig. 6.5, are depicted for an initial rotor angle $\varepsilon(t = 0\,\mathrm{s}) = 0$ at rated speed ($n_\mathrm{me} = 3100\,\mathrm{min}^{-1}$). Although the trajectories of the TO-HRG for rated speed are already shown in Fig. 6.5, they are also shown in Fig. 6.6 to allow a better comparison with the HRG and DBFC methods.

Both the TO-HRG and DBFC methods achieve TOC performance. The DBFC method does not take into account current and torque constraints, resulting in significant undesired overcurrents, torque overshoots and undershoots, and non-monotonic torque trajectories, see Fig. 6.6a for $t \in [5\,\mathrm{ms}, 7\,\mathrm{ms}]$. The HRG and DBFC methods do not consider torque and current constraints. However, unlike the DBFC method, the HRG is not able to achieve TOC performance which still leads to undesired control behavior, such as overcurrents and torque undershoots, and also to reduced control dynamics. Only the proposed TO-HRG can achieve both TOC performance without overcurrents and without increased torque overshoots and undershoots.

6.4 Experimental Investigation

Several experiments and comparisons with state-of-the-art control methods are carried out to study the TO-HRG. The description of the experimental setup is given in App. B. The controller parameters of the overall TO-HRG control scheme are listed in Tab. 6.2.

The turnaround times of the overall control scheme with its sub-functions (OPC, GFO, TO-HRG, CCS-MPFC, auxiliary functions) are listed in Tab. 6.3. The turnaround time reported for the auxiliary functions summarizes the time that is required to execute, e.g., SVM, PC scheme, coordinate transformations, analog-digital conversion, as well as processor and host computer communication, which must be executed in addition to the OPC, GFO, TO-HRG, and CCS-MPFC. Due to the CCS-MPFC, cf. 5.6, and the deactivation of the TO-HRG in the linear modulation range, the total turnaround time varies (43.4-56.1 µs), see Tab. 6.3.

During steady-state control operation, the flux-linkage reference must not be pre-rotated by the RPR and no state constraints are active. Therefore, the steady-state control performance of the proposed method is the same as the HRG method presented in Ch. 4. Since steady-state investigations for the HRG method have already been thoroughly performed in Sec. 4.4, only highly dynamic transient experiments are performed in this section.

Tab. 6.2: TO-HRG controller parameters

TO-HRG		
Number of RPR iterations	N	5
Time threshold	t_{thresh}	$1.5T_{\mathrm{s}}$
Dynamic current limit	$I_{\mathrm{max,dyn}}$	300 A
D-axis current limit	$i_{\mathrm{d,max}}$	30 A
PC		
Pulse clipping time	T_{c}	15 µs
GFO		
Damping ratio	ξ	1
Characteristic frequency	ω_0	$675\,\mathrm{s}^{-1}$
FMC		
Low-pass filter time constant	τ	20 ms
Speed threshold	ω_{fmc}	$270\,\mathrm{s}^{-1}$

Tab. 6.3: Turnaround times of the proposed TO-HRG control scheme

	Turnaround time in µs
OPC	8.4
FMC	1.3
GFO	2.3
TO-HRG	3.3
CCS-MPFC	1.2-10.5
Auxiliary functions	29.3
Overall control strategy	43.4-56.1

6.4.1 Torque Step Response

In Fig. 6.7 and Fig. 6.8, a torque step response to maximum torque at a speed of $n_{\mathrm{me}} = 5600\,\mathrm{min}^{-1}$ with an initial rotor angle of $\varepsilon(t = 0\,\mathrm{s}) = 0$ is depicted. For the visualization, both, the flux

linkage $\boldsymbol{\psi}_{\alpha\beta}$ and its reference $\boldsymbol{\psi}^*_{\alpha\beta}$ are transformed to the dq frame to allow a better recognition of the flux linkage control error compared to a visualization in the $\alpha\beta$ frame. A slightly increased speed compared to the nominal speed of $n_{\mathrm{me}} = 5350\,\mathrm{min}^{-1}$ is ensured by the load machine, such that the OPC always chooses operating points $\overline{\boldsymbol{i}^*_{\mathrm{dq}}}$ at the voltage limits, even for small variations of DC-link voltage and speed. At this slightly increased speed, the modulation index is permanently in saturation ($m = 1$) and the six-step operation of the control scheme without additional intermediate pulses can be shown, see Fig. 6.7. Due to the torque transient of the test IPMSM, the rotor speed is increased until the speed-controlled load IM reaches its steady state, see Fig. 6.7a. In addition, the DC-link voltage varies due to the increased current demand of the test IPMSM. As both the speed and the DC-link voltage vary, the operating point selected by the OPC varies accordingly, see Fig. 6.7a. This variation inevitably leads to additional oscillations of the current and a change in the diameter of the hexagonal flux linkages during six-step operation, see Fig. 6.8b. Nevertheless, the proposed control scheme is able to handle the given challenging scenario of transiently varying speed and DC-link voltage without overcurrents and without torque overshoots as long as the state (flux linkage or current) of the IPMSM is within the linear modulation iso-voltage loci.

Additionally, the current and flux linkage trajectories for constant speed and constant DC-link voltage ($t > 0.3\,\mathrm{s}$) are highlighted in Fig. 6.8a and Fig. 6.8c. These trajectories represent the steady-state control performance at this operating point. Here, the typical drop shape during six-step operation of the current in the rotor-fixed frame can be seen. Furthermore, the flux linkage coincides closely with its reference.

6.4.2 Speed Dependency Investigation

The torque, current, and switching vector trajectories for torque reference steps to maximum and minimum torque operation for different speeds up to maximum speed are shown in Fig. 6.9. Additionally, the variation of the iso-voltage due to the varying DC-link voltage and speed caused by the torque transients is shown in light green.

The speed of $n_{\mathrm{me}} = 3000\,\mathrm{min}^{-1}$ results in modulation indices within the linear modulation range. Therefore, no additional current, flux, or torque harmonics are induced by the voltage constraint during steady-state operation. Furthermore, the HRGs of the TO-HRG are inactive within the linear modulation range and the proposed control scheme is equivalent to the TOC presented in Ch. 5.

Due to the active voltage limit for speeds of $n_{\mathrm{me}} = \{5600, 7000, 11000\}\ \mathrm{min}^{-1}$, the rated torque can no longer be reached, see Fig. 6.9a. Nevertheless, the proposed control scheme ensures that the maximum and minimum possible torques are achieved for the corresponding speed. To enable maximum and minimum torque operation, six-step operation must be used for $n_{\mathrm{me}} = \{5600, 7000, 11000\}\ \mathrm{min}^{-1}$ during steady-state operation. However, for a speed of $n_{\mathrm{me}} = 5600\,\mathrm{min}^{-1}$ during $t \in [8\,\mathrm{ms}, 10\,\mathrm{ms}]$, additional switching pulses occur. This happens because the transition from maximum to minimum torque temporarily increases the DC-link voltage and decreases the speed. This leads to a short-time relaxation of the iso-voltage locus, with the rated generative operating point (intersection of MTPC and I_{max} loci) lying within the iso-voltage. Consequently, operation at the voltage limit is no longer necessary and additional switching pulses take place.

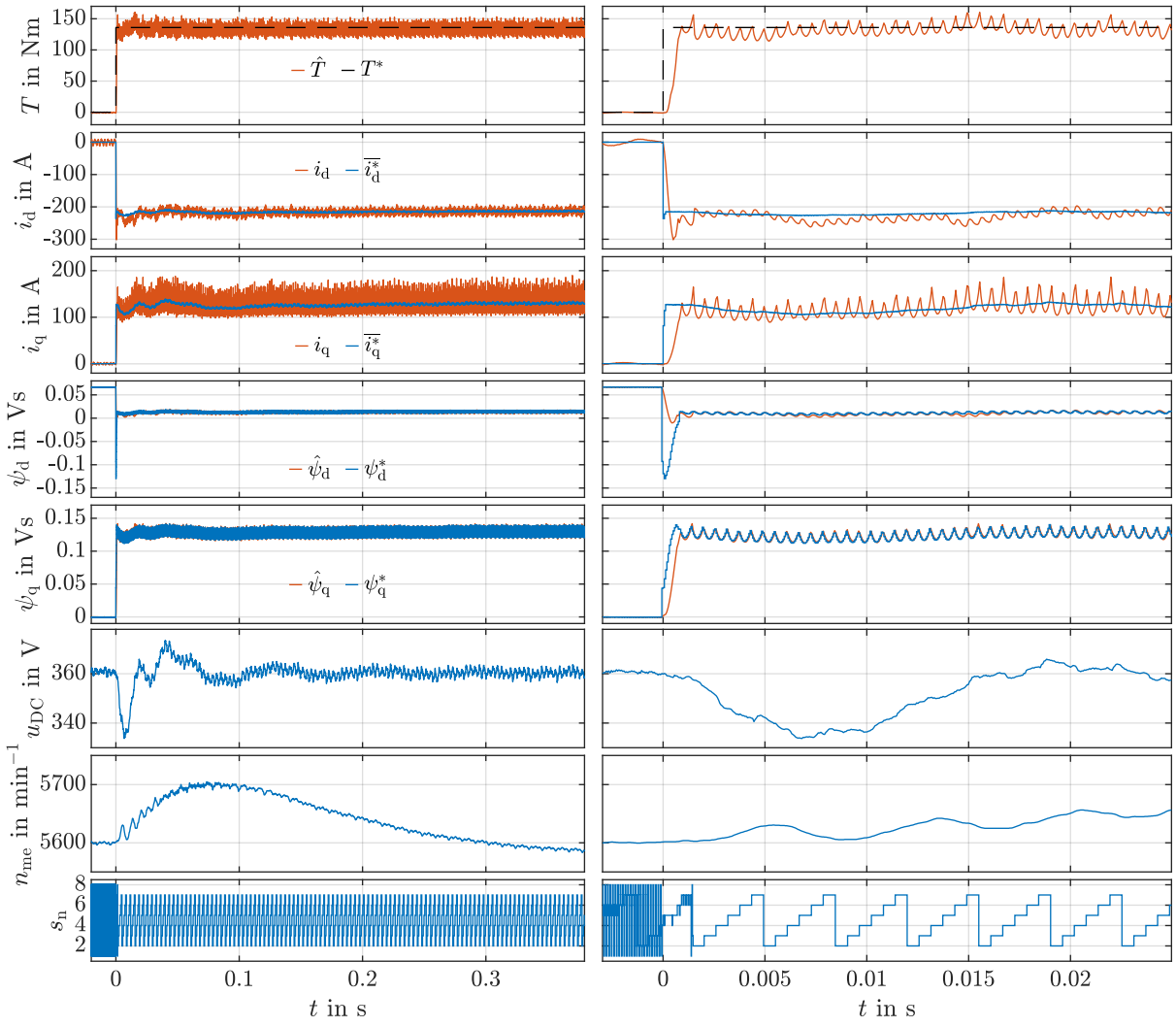

(a) Full view **(b)** Zoom in

Fig. 6.7: Experimental torque step response to maximum torque at a speed of $n_{\mathrm{me}} = 5600\,\mathrm{min}^{-1}$ with $\varepsilon(t = 0\,\mathrm{s}) = 0$ [8, Fig. 18]

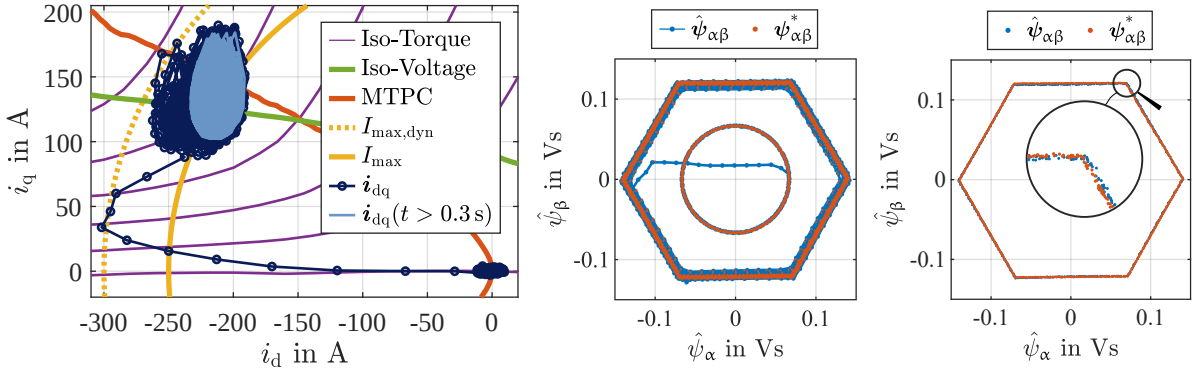

(a) Current trajectories **(b)** Flux trajectories **(c)** Flux trajectories for $t > 0.3\,\mathrm{s}$

Fig. 6.8: Experimental trajectories of Fig. 6.7 in the dq current and αβ flux plane [8, Fig. 19]

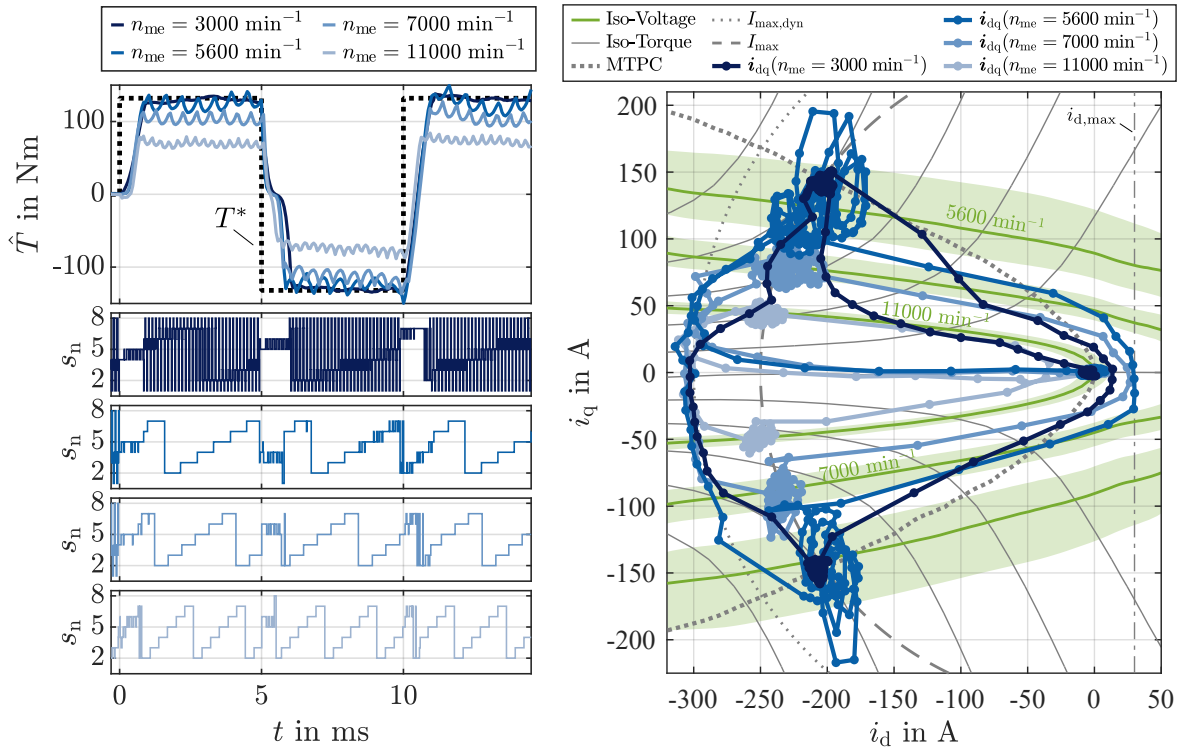

(a) Torque and switching trajectories **(b)** Current trajectories

Fig. 6.9: Experimental TO-MPC trajectories for maximum and minimum torque operation for different speeds n_{me} with an initial rotor angle $\varepsilon(t = 0\,\mathrm{s}) = 0$ [8, Fig. 20]

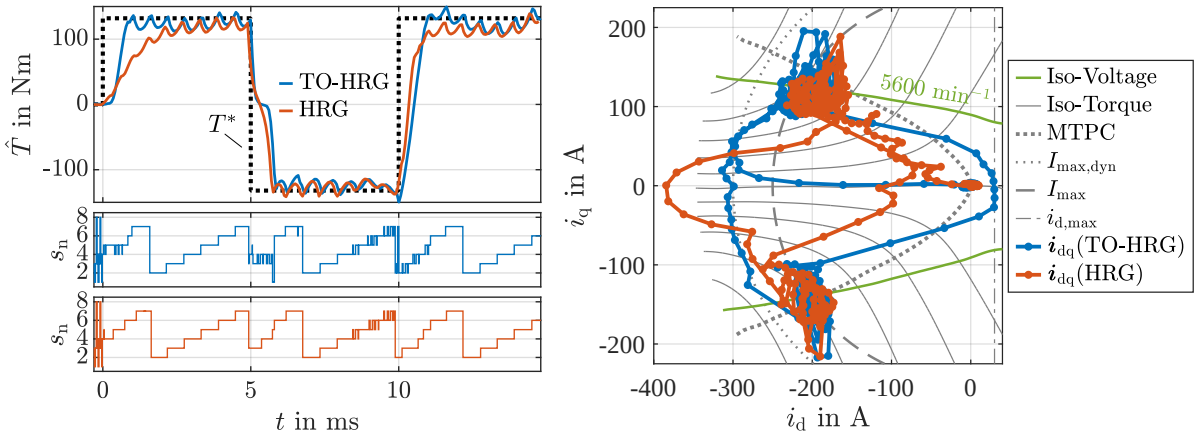

(a) Torque and switching vector trajectories

(b) Current trajectories

Fig. 6.10: Experimental trajectories of the TO-HRG and HRG method for maximum and minimum torque operation at $n_{me} = 5600\,\mathrm{min}^{-1}$ with an initial rotor angle $\varepsilon(t = 0\,\mathrm{s}) = 0$ [8, Fig. 21]

6.4.3 Comparison to State-of-the-Art Methods

The results of the experimental comparison with the nonlinearly magnetized IPMSM shown in Fig. 6.10 coincide with the simulative comparison of the linearly magnetized IPMSM:

- Both the proposed TO-HRG and HRG methods achieve the same steady-state control performance.
- The TO-HRG enables fastest control performance without violating the state constraints.
- Because the flux linkage reference is not pre-rotated for the HRG method, control dynamics are reduced.
- Slight overcurrents can occur with the HRG method because state constraints are not taken into account.

The DBFC method [16] investigated in the simulative comparison, cf. Sec. 6.3.3 led to emergency shutdowns of the testbench because the current limit was exceeded. Therefore, only the TO-HRG and HRG methods are compared experimentally and shown in Fig. 6.10. In [16], smaller steps of the reference torque of the DBFC are commanded, resulting in less prominent torque overshoots and undershoots as well as overcurrents. The authors of [16] suggest either accepting the undesired control behavior or reducing the rate of change of the torque reference for reference steps with increased amplitude. By reducing the rate of change of the reference torque, the TOC performance of the DBFC can no longer be attained.

7 Conclusion and Outlook

7.1 Conclusion

In this work, a continuous control set model predictive flux control (CCS-MPFC) scheme was presented that increases the electromagnetic utilization of synchronous machine (SM) drives with significant magnetic (cross-)saturation effects to its maximum extent during transient and steady-state operation, i.e., maximum control dynamics and maximum voltage utilization during high-speed operation.

The maximization of voltage utilization during steady-state operation (six-step operation) has been achieved by adding a harmonic component to the mean flux linkage reference with the help of a harmonic reference generator (HRG) in combination with a pulse clipping (PC) scheme to suppress short undesired switching pulses of the inverter. Since the maximization of voltage utilization is achieved only with the PC and HRG scheme, there is no need to adapt the CCS-MPFC which allows a seamless transition of the control scheme to the full speed and modulation range without controller reconfiguration.

To reach the operating point in the shortest possible time during transients, the solution of a time-optimal control (TOC) problem is incorporated by an angular flux linkage reference pre-rotation (RPR). To prevent significant overcurrents as well as torque undershoots and overshoots, time-varying torque and current limits were added as state constraints to the CCS-MPFC.

The HRG and PC for maximum voltage utilization was merged with the RPR for TOC performance. This fusion of RPR and HRG, referred to as time-optimal harmonic reference generator (TO-HRG), with the presented state-constrained CCS-MPFC exploits the drive's performance during steady-state and transient operation to full extent with the following main features:

- Transient processes, i.e., operating point changes, are performed in the fastest possible way without overcurrents and torque overshoots or undershoots. Here, the time to reach the rated torque from zero torque at rated speed was reduced by 67 % compared to proportional-integral field-oriented control (PI-FOC) and by 57 % compared to a deadbeat controller.
- During steady-state operation at the voltage limit, the six-step operating capability of the control scheme ensures maximum power and torque conversion of the drive, i.e., an increase of the drive's power of approx. 10 % compared to drives with controller schemes that are limited to the linear modulation range, e.g., PI-FOC.
- Seamless transitions between modulation regions and operating points are enabled without controller reconfiguration and transition shocks.

7.2 Outlook

Based on the results of this work, follow-up studies and extensions of the investigated control concepts result:

- The investigated methods are conceptually designed for highly utilized SMs with two states (i_d and i_q), as it is the case for permanent magnet synchronous machines (PMSM) and synchronous reluctance machines (SynRM). The applicability of the investigated methods with possible extensions to machines with additional degrees of freedom, such as induction machines (IM) or externally excited synchronous machines (EESM), represents an interesting research topic.
- Furthermore, the extension and generalization of the proposed method to multiphase machine and multilevel inverter applications shall be investigated.
- The state-constrained CCS-MPFC with the TO-HRG method (cf. Ch. 6), which achieves time-optimal control in the entire modulation range while respecting torque and current limits, uses a space vector modulation (SVM). Compared to SVM, optimized pulse patterns (OPP) are synchronized to the stator frequency and are applied especially at high speeds with low pulse numbers to minimize the current distortion induced by the switching operation of the inverter. Therefore, an extension of the TO-HRG method to incorporate OPPs is a promising research topic.
- In this work, an angle-dependent magnetization in the dq frame of SMs caused by a non-sinusoidal flux linkage distribution in the air gap is neglected. This simplification leads to additional torque harmonics, resulting in unwanted radiation of structural vibrations and acoustic noise via the machine shaft and machine housing. To prevent these harmonic torques, appropriate harmonic flux linkages must be superimposed on the mean flux linkage. This requires a remaining available DC-link voltage. As a result, the previously mentioned reduction of torque harmonics cannot be realized when operating at the voltage limit. Studies are required to investigate how these harmonic components can be determined during online operation and whether they can be incorporated into the presented control method.

Bibliography

[1] A. T. De Almeida, F. J. T. E. Ferreira, and J. A. Fong, "Standards for efficiency of electric motors," *IEEE Industry Applications Magazine*, vol. 17, no. 1, pp. 12–19, 2011. DOI: 10.1109/MIAS.2010.939427.

[2] J. Holtz, "Advanced PWM and predictive control — An overview," *IEEE Transactions on Industrial Electronics*, vol. 63, no. 6, pp. 3837–3844, 2016. DOI: 10.1109/TIE.2015.2504347.

[3] R. Monajemy and R. Krishnan, "Performance comparison for six-step voltage and constant back EMF control strategies for PMSM," in *34th Annual IEEE Industry Applications Conference*, 1999, pp. 165–172. DOI: 10.1109/IAS.1999.799949.

[4] T. Schoenen, A. Krings, D. van Treek, and R. W. De Doncker, "Maximum DC-link voltage utilization for optimal operation of IPMSM," in *IEEE International Electric Machines & Drives Conference*, 2009, pp. 1547–1550. DOI: 10.1109/IEMDC.2009.5075409.

[5] A. Brosch, O. Wallscheid, and J. Böcker, "Model predictive control of permanent magnet synchronous motors in the overmodulation region including six-step operation," *IEEE Open Journal of Industry Applications*, vol. 2, pp. 47–63, 2021. DOI: 10.1109/OJIA.2021.3066105.

[6] A. Brosch, O. Wallscheid, and J. Böcker, "Model predictive torque control for permanent magnet synchronous motors using a stator-fixed harmonic flux reference generator in the entire modulation range," *IEEE Transactions on Power Electronics*, vol. 38, no. 4, pp. 4391–4404, 2023. DOI: 10.1109/TPEL.2022.3229619.

[7] A. Brosch, O. Wallscheid, and J. Böcker, "Time-optimal model predictive control of permanent magnet synchronous motors considering current and torque constraints," *IEEE Transactions on Power Electronics*, vol. 38, no. 7, pp. 7945–7957, 2023. DOI: 10.1109/TPEL.2023.3265705.

[8] A. Brosch, O. Wallscheid, and J. Böcker, "Time-optimal model predictive control of permanent magnet synchronous motors in the whole speed and modulation range considering current and torque constraints," *Preprint submitted to IEEE Open Journal of the Industrial Electronics Society*, 2023. DOI: 10.36227/techrxiv.22587028.v1.

[9] W. Leonhard, *Control of electrical drives*. Springer Berlin, 2001.

[10] D. Schröder and J. Böcker, *Elektrische Antriebe – Regelung von Antriebssystemen*. Springer, 2021.

[11] C. M. Hackl, J. Kullick, H. Eldeeb, and L. Horlbeck, "Analytical computation of the optimal reference currents for MTPC/MTPA, MTPV and MTPF operation of anisotropic synchronous machines considering stator resistance and mutual inductance," in *19th European Conference on Power Electronics and Applications*, 2017. DOI: 10.23919/EPE17ECCEEurope.2017.8099040.

[12] J. S. Lee, C.-H. Choi, J.-K. Seok, and R. D. Lorenz, "Deadbeat-direct torque and flux control of interior permanent magnet synchronous machines with discrete time stator current and stator flux linkage observer," *IEEE Transactions on Industry Applications*, vol. 47, no. 4, pp. 1749–1758, 2011. DOI: 10.1109/TIA.2011.2154293.

[13] M. Saur, B. Lehner, F. Hentschel, D. Gerling, and R. D. Lorenz, "DB-DTFC as loss minimizing control for synchronous reluctance drives," in *41st Annual Conference of the IEEE Industrial Electronics Society*, 2015, pp. 1412–1417. DOI: 10.1109/IECON.2015.7392298.

[14] F. Blaschke, "Das Verfahren der Feldorientierung zur Regelung der Drehfeldmaschine (in German)," Doctoral thesis, Technische Universität Braunschweig, 1973.

[15] S. Bolognani, M. Tomasini, L. Tubiana, and M. Zigliotto, "DSP-based time optimal current control for high dynamic IPM motor drives," in *IEEE 35th Annual Power Electronics Specialists Conference*, vol. 3, 2004, pp. 2197–2203. DOI: 10.1109/PESC.2004.1355461.

[16] H. El Khatib, D. Gerling, and M. Saur, "Deadbeat flux vector control as a one single control law operating in the linear, overmodulation, and six-step regions with time-optimal torque control," *IEEE Open Journal of Industry Applications*, vol. 3, pp. 247–270, 2022. DOI: 10.1109/OJIA.2022.3222852.

[17] J.-W. Choi and S.-K. Sul, "Generalized solution of minimum time current control in three-phase balanced systems," *IEEE Transactions on Industrial Electronics*, vol. 45, no. 5, pp. 738–744, 1998. DOI: 10.1109/41.720330.

[18] V. Šmídl, A. Glac, and Z. Peroutka, "Time-optimal current control of synchronous motor drives," *Actuators*, vol. 12, no. 1, 2023. DOI: 10.3390/act12010015.

[19] W. Wang, M. Du, and K. Wei, "Rapid torque rising of PMSM by directly chasing rotating flux linkage vector," *IEEE Journal of Emerging and Selected Topics in Power Electronics*, vol. 9, no. 4, pp. 4384–4394, 2021. DOI: 10.1109/JESTPE.2020.3048091.

[20] Y. Wang, W. Xie, X. Wang, W. Yang, M. Dou, S. Song, and D. Gerling, "Fast response model predictive torque and flux control with low calculation effort for PMSMs," *IEEE Transactions on Industrial Informatics*, vol. 15, no. 10, pp. 5531–5540, 2019. DOI: 10.1109/TII.2019.2900116.

[21] W. Peters, O. Wallscheid, and J. Böcker, "A precise open-loop torque control for an interior permanent magnet synchronous motor (IPMSM) considering iron losses," in *38th Annual Conference on IEEE Industrial Electronics Society*, 2012, pp. 2877–2882. DOI: 10.1109/IECON.2012.6389438.

[22] L. Zhong, M. Rahman, W. Hu, and K. Lim, "Analysis of direct torque control in permanent magnet synchronous motor drives," *IEEE Transactions on Power Electronics*, vol. 12, no. 3, pp. 528–536, 1997. DOI: 10.1109/63.575680.

[23] A. Favato, P. G. Carlet, F. Toso, R. Torchio, and S. Bolognani, "Integral model predictive current control for synchronous motor drives," *IEEE Transactions on Power Electronics*, vol. 36, no. 11, pp. 13 293–13 303, 2021. DOI: 10.1109/TPEL.2021.3081827.

[24] S. Hanke, O. Wallscheid, and J. Böcker, "Continuous-control-set model predictive control with integrated modulator in permanent magnet synchronous motor applications," in *IEEE International Electric Machines & Drives Conference*, 2019, pp. 2210–2216. DOI: 10.1109/IEMDC.2019.8785122.

[25] M. Preindl, "Robust control invariant sets and Lyapunov-based MPC for IPM synchronous motor drives," *IEEE Transactions on Industrial Electronics*, vol. 63, no. 6, pp. 3925–3933, 2016. DOI: 10.1109/TIE.2016.2527722.

[26] S. Wendel, P. Karamanakos, P. Gebhardt, A. Dietz, and R. Kennel, "Flux linkage-based direct model predictive current control for synchronous machines," *IEEE Transactions on Power Electronics*, vol. 36, no. 12, pp. 14 237–14 256, 2021. DOI: 10.1109/TPEL.2021.3083657.

[27] T. Huber, W. Peters, and J. Bocker, "Voltage controller for flux weakening operation of interior permanent magnet synchronous motor in automotive traction applications," in *IEEE International Electric Machines & Drives Conference*, 2015, pp. 1078–1083. DOI: 10.1109/IEMDC.2015.7409195.

[28] S.-M. Kim and S.-K. Sul, "Speed control of interior permanent magnet synchronous motor drive for flux weakening operation," in *30th Annual IEEE Industry Applications Conference*, 1995, 216–221 vol.1. DOI: 10.1109/IAS.1995.530304.

[29] N. Bedetti, S. Calligaro, and R. Petrella, "Analytical design and autotuning of adaptive flux-weakening voltage regulation loop in IPMSM drives with accurate torque regulation," *IEEE Transactions on Industry Applications*, vol. 56, no. 1, pp. 301–313, 2020. DOI: 10.1109/TIA.2019.2942807.

[30] W. Peters and J. Böcker, "Discrete-time design of adaptive current controller for interior permanent magnet synchronous motors (IPMSM) with high magnetic saturation," in *39th Annual Conference of the IEEE Industrial Electronics Society*, 2013, pp. 6608–6613. DOI: 10.1109/IECON.2013.6700225.

[31] O. Wallscheid, M. S. Shafiq, and J. Böcker, "Stator flux-based field-oriented position-sensorless control of permanent magnet synchronous motors with limited parameter knowledge," in *IEEE 28th International Symposium on Industrial Electronics*, 2019, pp. 402–407. DOI: 10.1109/ISIE.2019.8781235.

[32] A. Khambadkone and J. Holtz, "Compensated synchronous PI current controller in overmodulation range and six-step operation of space-vector-modulation-based vector-controlled drives," *IEEE Transactions on Industrial Electronics*, vol. 49, no. 3, pp. 574–580, 2002. DOI: 10.1109/TIE.2002.1005382.

[33] K. Kondou and S. Doki, "A study on the application of the PMSM vector control system for high speed motor in inverter overmodulation range," in *IEEE Vehicle Power and Propulsion Conference*, 2014. DOI: 10.1109/VPPC.2014.7007009.

[34] S. Lerdudomsak, S. Doki, and S. Okuma, "A novel current control system for PMSM considering effects from inverter in overmodulation range," in *7th International Conference on Power Electronics and Drive Systems*, 2007, pp. 794–800. DOI: 10.1109/PEDS.2007.4487795.

[35] S. Lerdudomsak, S. Doki, and S. Okuma, "Harmonic currents estimation and compensation for current control system of PMSM in overmodulation range - Analysis for robustness to parameter variations," in *34th Annual Conference of IEEE Industrial Electronics*, 2008, pp. 1216–1221. DOI: 10.1109/IECON.2008.4758128.

[36] H. Nakai, H. Ohtani, and Y. Inaguma, "Novel torque control technique for high efficiency / high power interior permanent magnet synchronous motors," in *RD Review of Toyota CRDL*, 2005.

[37] Y.-C. Kwon, S. Kim, and S.-K. Sul, "Six-step operation of PMSM with instantaneous current control," *IEEE Transactions on Industry Applications*, vol. 50, no. 4, pp. 2614–2625, 2014. DOI: 10.1109/TIA.2013.2296652.

[38] S. Bolognani and M. Zigliotto, "Novel digital continuous control of SVM inverters in the overmodulation range," *IEEE Transactions on Industry Applications*, vol. 33, no. 2, pp. 525–530, 1997. DOI: 10.1109/28.568019.

[39] J. Holtz, W. Lotzkat, and A. Khambadkone, "On continuous control of PWM inverters in the overmodulation range including the six-step mode," *IEEE Transactions on Power Electronics*, vol. 8, no. 4, pp. 546–553, 1993. DOI: 10.1109/63.261026.

[40] F. Allgöwer and A. Zheng, *Nonlinear Model Predictive Control*. Birkhäuser, 2012, vol. 26.

[41] C. F. Garcia, C. A. Silva, J. R. Rodriguez, P. Zanchetta, and S. A. Odhano, "Modulated model-predictive control with optimized overmodulation," *IEEE Journal of Emerging and Selected Topics in Power Electronics*, vol. 7, no. 1, pp. 404–413, 2019. DOI: 10.1109/JESTPE.2018.2828198.

[42] J. Ishida, S. Doki, and S. Okuma, "Fast torque control system of PMSM based on model predictive control considering overmodulation region," in *The International Power Electronics Conference*, 2010, pp. 1403–1406. DOI: 10.1109/IPEC.2010.5544570.

[43] M. Kadota, S. Lerdudomsak, S. Doki, and S. Okuma, "A novel current control system of IPMSM operating at high speed based on model predictive control," in *Power Conversion Conference*, 2007, pp. 1315–1319. DOI: 10.1109/PCCON.2007.373135.

[44] P. Karamanakos and T. Geyer, "Guidelines for the design of finite control set model predictive controllers," *IEEE Transactions on Power Electronics*, vol. 35, no. 7, pp. 7434–7450, 2020. DOI: 10.1109/TPEL.2019.2954357.

[45] G. Pei, L. Li, X. Gao, J. Liu, and R. Kennel, "Predictive current trajectory control for PMSM at voltage limit," *IEEE Access*, vol. 8, pp. 1670–1679, 2020. DOI: 10.1109/ACCESS.2019.2962742.

[46] A. Sarajian, C. F. Garcia, Q. Guan, P. Wheeler, D. A. Khaburi, R. Kennel, J. Rodriguez, and M. Abdelrahem, "Overmodulation methods for modulated model predictive control and space vector modulation," *IEEE Transactions on Power Electronics*, vol. 36, no. 4, pp. 4549–4559, 2021. DOI: 10.1109/TPEL.2020.3023927.

[47] F. Toso, P. G. Carlet, A. Favato, and S. Bolognani, "On-line continuous control set MPC for PMSM drives current loops at high sampling rate using qpOASES," in *IEEE Energy Conversion Congress and Exposition*, 2019, pp. 6615–6620. DOI: 10.1109/ECCE.2019.8912838.

[48] X. Wang, X. Fang, F. Lin, and Z. Yang, "Predictive current control of permanent-magnet synchronous motors for rail transit including quasi six-step operation," in *IEEE Transportation Electrification Conference and Expo*, 2017. DOI: 10.1109/ITEC-AP.2017.8080770.

[49] X. Fang, S. Lin, X. Wang, Z. Yang, F. Lin, and Z. Tian, "Model predictive current control of traction permanent magnet synchronous motors in six-step operation for railway application," *IEEE Transactions on Industrial Electronics*, vol. 69, no. 9, pp. 8751–8759, 2022. DOI: 10.1109/TIE.2021.3114695.

[50] H. El Khatib, D. Gaona, D. Gerling, and M. Saur, "Deadbeat flux vector control with continuous transition from linear to overmodulation including six-step operation considering the voltage and current limits by applying one single control law," in *23rd European Conference on Power Electronics and Applications*, 2021. DOI: 10.23919/EPE21ECCEEurope50061.2021.9570647.

[51] K. Asano, Y. Inaguma, H. Ohtani, E. Sato, M. Okamura, and S. Sasaki, "High performance motor drive technologies for hybrid vehicles," in *Power Conversion Conference*, 2007, pp. 1584–1589. DOI: 10.1109/PCCON.2007.373175.

[52] M. Depenbrock, "Direct self-control (DSC) of inverter-fed induction machine," *IEEE Transactions on Power Electronics*, vol. 3, no. 4, pp. 420–429, 1988. DOI: 10.1109/63.17963.

[53] A. Hava, R. Kerkman, and T. Lipo, "Carrier-based PWM-VSI overmodulation strategies: Analysis, comparison, and design," *IEEE Transactions on Power Electronics*, vol. 13, no. 4, pp. 674–689, 1998. DOI: 10.1109/63.704136.

[54] D.-C. Lee and G.-M. Lee, "A novel overmodulation technique for space-vector PWM inverters," *IEEE Transactions on Power Electronics*, vol. 13, no. 6, pp. 1144–1151, 1998. DOI: 10.1109/63.728341.

[55] H. Lee, J. Kim, J. Hong, and K. Nam, "Torque control for IPMSM in the high speed range based on voltage angle," in *IEEE Applied Power Electronics Conference and Exposition*, 2014, pp. 2500–2505. DOI: 10.1109/APEC.2014.6803655.

[56] M. K. Modi and G. Narayanan, "Improved single-zone overmodulation algorithm for space vector modulated inverters," in *IEEE International Conference on Power Electronics, Drives and Energy Systems*, 2014. DOI: 10.1109/PEDES.2014.7042107.

[57] S. Bolognani and M. Zigliotto, "Space vector Fourier analysis of SVM inverters in the overmodulation range," in *IEEE International Conference on Power Electronics, Drives and Energy Systems*, vol. 1, 1996, pp. 319–324. DOI: 10.1109/PEDES.1996.539559.

[58] B. Han, J.-S. Lee, Y. Bak, and K.-B. Lee, "Six-step operation strategy for direct self-control method of interior permanent magnet synchronous motors based on torque angle," *Journal of Power Electronics*, vol. 21, pp. 1352–1364, 2021. DOI: 10.1007/s43236-021-00281-1.

[59] M. Peña, M. Meyer, O. Wallscheid, and J. Böcker, "Model predictive direct self-control for six-step operation of permanent magnet synchronous machines," *IEEE Transactions on Power Electronics*, 2023. DOI: 10.1109/TPEL.2023.3286713.

[60] A. Gaeta, P. Zanchetta, F. Tinazzi, and M. Zigliotto, "Advanced self-commissioning and feed-forward compensation of inverter non-linearities," in *IEEE International Conference on Industrial Technology*, 2015, pp. 610–616. DOI: 10.1109/ICIT.2015.7125067.

[61] S.-G. Jeong and M.-H. Park, "The analysis and compensation of dead-time effects in PWM inverters," *IEEE Transactions on Industrial Electronics*, vol. 38, no. 2, pp. 108–114, 1991. DOI: 10.1109/41.88903.

[62] Y. Murai, T. Watanabe, and H. Iwasaki, "Waveform distortion and correction circuit for PWM inverters with switching lag-times," *IEEE Transactions on Industry Applications*, vol. 23, no. 5, pp. 881–886, 1987. DOI: 10.1109/TIA.1987.4504998.

[63] M. Seilmeier, C. Wolz, and B. Piepenbreier, "Modelling and model based compensation of non-ideal characteristics of two-level voltage source inverters for drive control application," in *1st International Electric Drives Production Conference*, 2011, pp. 17–22. DOI: 10.1109/EDPC.2011.6085542.

[64] M. Stender, O. Wallscheid, and J. Böcker, "Comparison of gray-box and black-box two-level three-phase inverter models for electrical drives," *IEEE Transactions on Industrial Electronics*, vol. 68, no. 9, pp. 8646–8656, 2021. DOI: 10.1109/TIE.2020.3018060.

[65] J. Böcker, "Discrete-time model of an induction motor," *European Transactions on Electrical Power*, vol. 1, no. 2, pp. 65–71, 1991. DOI: https://doi.org/10.1002/etep.4450010202.

[66] A. Specht, S. Ober-Blöbaum, O. Wallscheid, C. Romaus, and J. Böcker, "Discrete-time model of an IPMSM based on variational integrators," in *International Electric Machines & Drives Conference*, 2013, pp. 1411–1417. DOI: 10.1109/IEMDC.2013.6556322.

[67] M. Papageorgiou, M. Leibold, and M. Buss, *Optimierung*. Springer, 2015, vol. 4.

[68] J. T. Betts, *Practical methods for optimal control and estimation using nonlinear programming*. SIAM, 2010.

[69] J. T. Betts, "Survey of numerical methods for trajectory optimization," *Journal of guidance, control, and dynamics*, vol. 21, no. 2, pp. 193–207, 1998.

[70] L. T. Biegler, *Nonlinear programming: Concepts, algorithms, and applications to chemical processes*. SIAM, 2010.

[71] A. Cervantes and L. T. Biegler, "Optimization strategies for dynamic systems," *Encyclopedia of optimization*, vol. 4, pp. 216–227, 2009.
[72] R. Pytlak, *Numerical methods for optimal control problems with state constraints*. Springer Science & Business Media, 1999.
[73] B. Kouvaritakis and M. Cannon, *Model predictive control*. Springer, 2016.
[74] T. Geyer, *Model predictive control of high power converters and industrial drives*. John Wiley & Sons, 2016.
[75] L. Grüne and J. Pannek, *Nonlinear model predictive control*. Springer, 2017.
[76] J. Maciejowski, *Predictive control: with wonstraints*. Prentice Hall, 2002.
[77] J. Rawlings, D. Mayne, and M. Diehl, *Model predictive control: theory, computation, and design*. Nob Hill Publishing, 2017.
[78] L. S. Pontryagin, *Mathematical theory of optimal processes*. CRC press, 1987.
[79] H. van der Broeck, H.-C. Skudelny, and G. Stanke, "Analysis and realization of a pulsewidth modulator based on voltage space vectors," *IEEE Transactions on Industry Applications*, vol. 24, no. 1, pp. 142–150, 1988. DOI: 10.1109/28.87265.
[80] P. Jansen and R. Lorenz, "A physically insightful approach to the design and accuracy assessment of flux observers for field oriented induction machine drives," *IEEE Transactions on Industry Applications*, vol. 30, no. 1, pp. 101–110, 1994. DOI: 10.1109/28.273627.
[81] A. Yoo and S.-K. Sul, "Design of flux observer robust to parameter variation of interior permanent magnet synchronous motor," in *IEEE Industry Applications Society Annual Meeting*, 2008. DOI: 10.1109/08IAS.2008.221.
[82] H. Eldeeb, C. M. Hackl, L. Horlbeck, and J. Kullick, "A unified theory for optimal feedforward torque control of anisotropic synchronous machines," *International Journal of Control*, vol. 91, no. 10, pp. 2273–2302, 2018. DOI: 10.1080/00207179.2017.1338359.
[83] F. Briz, A. Diez, M. Degner, and R. Lorenz, "Current and flux regulation in field-weakening operation of induction motors," *IEEE Transactions on Industry Applications*, vol. 37, no. 1, pp. 42–50, 2001. DOI: 10.1109/28.903125.
[84] The MathWorks Inc., *Model predictive control toolbox version: 6.4 (R2020a)*, Natick, Massachusetts, United States, 2020. [Online]. Available: https://www.mathworks.com.
[85] J. Böcker, *Paderborn University, lecture notes: Controlled three-phase drives*, URL: https://ei.uni-paderborn.de/fileadmin-eim/elektrotechnik/fg/lea/Lehre/GDA/Dokumente/Geregelte_Drehstromantriebe_DE_EN.pdf. Version: 5.5.2021.
[86] S. Ogasawara, H. Akagi, and A. Nabae, "A novel PWM scheme of voltage source inverters based on space vector theory," *Archiv für Elektrotechnik*, vol. 74, pp. 33–41, 1990. DOI: doi.org/10.1007/BF01573229.
[87] J. Holtz and B. Beyer, "Optimal pulsewidth modulation for AC servos and low-cost industrial drives," *IEEE Transactions on Industry Applications*, vol. 30, no. 4, pp. 1039–1047, 1994. DOI: 10.1109/28.297921.
[88] O. Wallscheid and J. Böcker, "Wirkungsgradoptimale Arbeitspunktsteuerung für einen permanenterregten Synchronmotor mit vergrabenen Magneten unter Berücksichtigung von Temperatureinflüssen (in German)," in *Internationaler ETG-Kongress*, 2013.
[89] M. Ott and J. Böcker, "Sensitivity analysis on production tolerances for electric drive systems in automotive application," in *18th European Conference on Power Electronics and Applications*, 2016. DOI: 10.1109/EPE.2016.7695392.
[90] D. Huger and D. Gerling, "The effects of thermal cycling on aging of Neodymium-Iron-Boron magnets," in *IEEE 11th International Conference on Power Electronics and Drive Systems*, 2015, pp. 389–392. DOI: 10.1109/PEDS.2015.7203464.

[91] A. Brosch, O. Wallscheid, and J. Böcker, "Long-term memory recursive least squares online identification of highly utilized permanent magnet synchronous motors for finite-control-set model predictive control," *IEEE Transactions on Power Electronics*, vol. 38, no. 2, pp. 1451–1467, 2023. DOI: 10.1109/TPEL.2022.3206598.

[92] N. A. F. Senan, "A brief introduction to using ode45 in MATLAB," *University of California at Berkeley, USA*, 2007.

[93] E. Kerrigan and J. Maciejowski, "Soft constraints and exact penalty functions in model predictive control," in *Control Conference*, 2000.

[94] M. N. Zeilinger, M. Morari, and C. N. Jones, "Soft constrained model predictive control with robust stability guarantees," *IEEE Transactions on Automatic Control*, vol. 59, no. 5, pp. 1190–1202, 2014. DOI: 10.1109/TAC.2014.2304371.

[95] A. Brosch, O. Wallscheid, and J. Böcker, *Animation of the TO-MPC*, https://doi.org/10.1109/TPEL.2023.3265705/mm1.

[96] K. Åström and T. Hägglund, *Advanced PID Control*. ISA - The Instrumentation, Systems and Automation Society, 2006.

[97] N. Khaled and B. Pattel, *Practical Design and Application of Model Predictive Control: MPC for MATLAB® and Simulink® Users*. Butterworth-Heinemann, 2018.

[98] C. Schmid and L. Biegler, "Quadratic programming methods for reduced hessian SQP," *Computers & Chemical Engineering*, vol. 18, no. 9, pp. 817–832, 1994. DOI: https://doi.org/10.1016/0098-1354(94)E0001-4.

[99] M. Leuer, "Modellprädiktive Regelung permanent erregter Synchronmotoren im Antriebsstrang von Automobilen (in German)," Doctoral thesis, Paderborn University, 2014.

[100] W. Peters, "Wirkungsgradoptimale Regelung von permanenterregten Synchronmotoren in automobilen Traktionsanwendungen unter Berücksichtigung der magnetischen Sättigung (in German)," Doctoral thesis, Paderborn University, 2014.

Appendix

A Simulation Setup

Simulations are used to investigate the proposed control methods and to compare them with state-of-the-art methods. A linearly magnetized IPMSM model, cf. App. A.1, is mainly used for these studies. The parameters of the linearly magnetized IPMSM model are given in Tab. A.2. A nonlinearly magnetized IPMSM model, cf. App. A.1, is applied only for the studies in Sec. 4.2.4 and Sec. 4.3. This model corresponds to the nonlinearly magnetized IPMSM used for the experimental studies, cf. App. B. The parameters of the nonlinearly magnetized IPMSM, the flux linkages and the differential inductances are given in Tab. A.3, Fig. A.2 and Fig. A.3. It should be noted that the applied linearly magnetized IPMSM model corresponds to the linearly magnetized version of the nonlinearly magnetized IPMSM model.

From a didactical point of view, a linearly magnetized IPMSM was chosen for the simulative investigation. This is because, compared to the nonlinearly magnetized IPMSM, the time-optimal current trajectories, cf. Fig. 5.5b, of linearly magnetized SMs are easier to interpret due to the elliptically shaped motional terms $\boldsymbol{E_i}(\boldsymbol{i}_{\mathrm{dq}})$ in Fig. 5.5b. Furthermore, if readers want to implement the proposed control schemes and verify the results by comparing their resulting trajectories with the given simulated trajectories of this work, it is easier to implement the overall control scheme for a linear magnetization instead of a nonlinear magnetization of the SM.

All simulative investigations in this work were conducted with the software Simulink from MathWorks. Here, the SVM with inverter and IPMSM are modeled in a quasi-time continuous environment based on their equations reported in Sec. 2.2, Sec. 2.3, and Sec. 3.4. All proposed and state-of-the-art controllers in this thesis are simulated in a discrete-time subsystem with a controller sampling time of $T_{\mathrm{s}} = 62.5\,\mu\mathrm{s}$ and a DC-link voltage of $u_{\mathrm{DC}} = 360\,\mathrm{V}$. A simplified block diagram of the simulation setup is shown in Fig. A.1. The resulting ODE of the Simulink model is solved using the adaptive Runge-Kutta method ode45 [92]. The parameters of the simulation settings are listed in Tab. A.1. To fade out the harmonics induced by the inverter switching, the controller sampling is synchronized with the SVM. For the sake of clarity, the current, torque and flux ripples induced by the switching of the inverter are not shown in the figures of the simulated investigations.

A.1 Linearly Magnetized Interior Permanent Magnet Synchronous Machine Model Parameters

The linearly magnetized IPMSM model is the linearized version of the nonlinearly magnetized IPMSM model described in App. A.2. The parameters of the linearized IPMSM model are listed in Tab. A.2. Here, two different values are given for nominal power and speed. Both nominal power and speed depend on the maximum modulation index m_{max} that the controller can achieve during steady-state operation. Since the controller described in Ch. 5 is limited to the linear

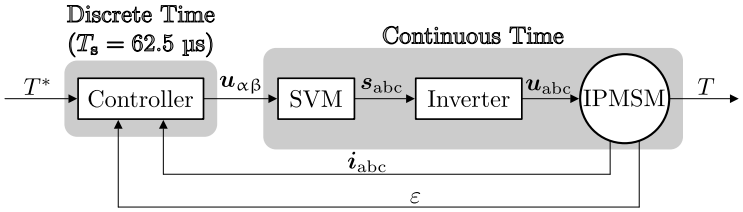

Fig. A.1: Simplified block diagram of the simulative investigations

Tab. A.1: Simulative test setup parameters

Simulation setup		
Software	Simulink	
Solver	ode45 [92]	
Controller sampling period	T_s	62.5 µs
DC-link voltage	u_{DC}	360 V

modulation range ($m = 0.907$) and the controllers proposed in Ch. 4 and Ch. 6 can fully utilize the available DC-link voltage ($m = 1$), the values of nominal power and speed are given for $m_{max} = \{0.907, 1\}$.

Although the proposed control schemes are derived for the more general case of a nonlinearly magnetized IPMSM, a linearly magnetized IPMSM can still be adopted. Here, the linear current-to-flux relation

$$\boldsymbol{\psi}_{dq}(\boldsymbol{i}_{dq}) = \begin{bmatrix} L_d & 0 \\ 0 & L_q \end{bmatrix} \boldsymbol{i}_{dq} + \begin{bmatrix} \psi_p \\ 0 \end{bmatrix} \tag{A.1}$$

with the permanent magnet flux linkage ψ_p and constant differential inductances

$$\boldsymbol{L}_{dq,\Delta} = \begin{bmatrix} L_d & 0 \\ 0 & L_q \end{bmatrix} \tag{A.2}$$

with d- and q-axis inductances L_d, L_q must be inserted into the equations of the nonlinearly magnetized IPMSM. The resulting machine-characteristic MTPC and maximum torque per flux (MTPF) loci are depicted in Fig. A.4b.

A.2 Nonlinearly Magnetized Interior Permanent Magnet Synchronous Machine Model Parameters

The nonlinearly magnetized IPMSM model of the simulative studies in Sec. 4.2.4 and Sec. 4.3 corresponds to the nonlinearly magnetized IPMSM that is utilized for the experimental investigations. The parameters of the nonlinearly magnetized IPMSM are listed in Tab. A.3. Flux linkages and differential inductances of the nonlinearly magnetized IPMSM showing significant (cross-)saturation effects are depicted in Tab. A.3, Fig. A.2, and Fig. A.3. Especially along the q-axis a strong saturation is apparent which leads to a variation of the differential inductance $L_{qq}(\boldsymbol{i}_{dq})$ by a factor of approx. 10. The method proposed in [91] was used for the identification of flux linkages and differential inductances. Here, 80 equispaced stationary operating points with

Tab. A.2: Linearly magnetized IPMSM model parameters

Nominal speed ($m_{\max} = \{0.907, 1\}, u_{\mathrm{DC}} = 360\,\mathrm{V}$)	$n_{\mathrm{me,nom}}$	$\{2800, 3100\}$ min^{-1}
Nominal torque	T_{nom}	172 Nm
Nominal current	I_{nom}	177 A
Pole pair number	p	3
Stator resistance	R_{s}	18 mΩ
Permanent magnet flux	ψ_{p}	68 mVs
Inductances	L_{d}	0.37 mH
	L_{q}	1.2 mH

a maximum length of $\|\boldsymbol{i}_{\mathrm{dq}}\| = 350\,\mathrm{A}$ covering the left i_{d}-i_{q} half-plane were recorded. Machine-characteristic loci, i.e., MTPC and maximum torque per flux (MTPF) loci, are shown in Fig. A.4b. The MTPV locus is slightly different from the speed-independent MTPF locus due to the ohmic stator resistance. Since the ohmic voltage drop is small compared to the induced voltage at high speeds, the difference between the MTPV and MTPF loci can be considered minor. Additionally, the iso-voltage locus for the maximum speed of the machine of $n_{\mathrm{me}} = 11\,000\,\mathrm{min}^{-1}$ for $m = 1$ is shown. There is no intersection between MTPF or MTPV and the maximum speed iso-voltage locus within the current limit $I_{\max}$. Hence, MTPV operation is not necessary for the applied nonlinearly magnetized IPMSM and is not reported in this work.

Tab. A.3: Nonlinearly magnetized IPMSM model parameters

IPMSM	Brusa HSM16.17.12-C01	
Nominal power ($m_{\max} = \{0.907, 1\}, u_{\mathrm{DC}} = 360\,\mathrm{V}$)	P_{nom}	$\{67, 74\}$ kW
Nominal speed ($m_{\max} = \{0.907, 1\}, u_{\mathrm{DC}} = 360\,\mathrm{V}$)	$n_{\mathrm{me,nom}}$	$\{4850, 5330\}$ min^{-1}
Nominal torque	T_{nom}	132 Nm
Nominal current	I_{nom}	177 A
Maximum speed	$n_{\mathrm{me,max}}$	11 000 min^{-1}
Pole pair number	p	3
Stator resistance	R_{s}	18 mΩ
Permanent magnet flux	ψ_{p}	68 mVs

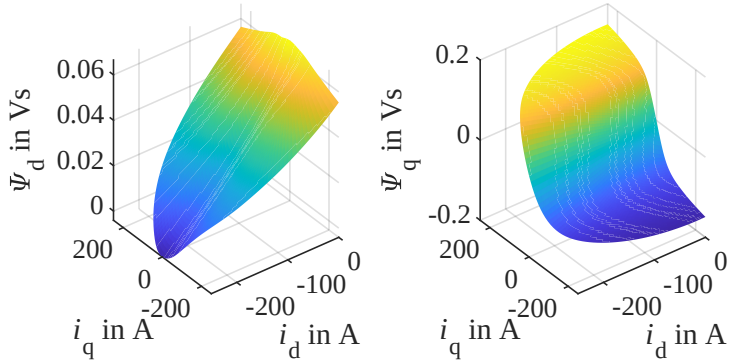

Fig. A.2: Flux linkage maps of the nonlinearly magnetized IPMSM model

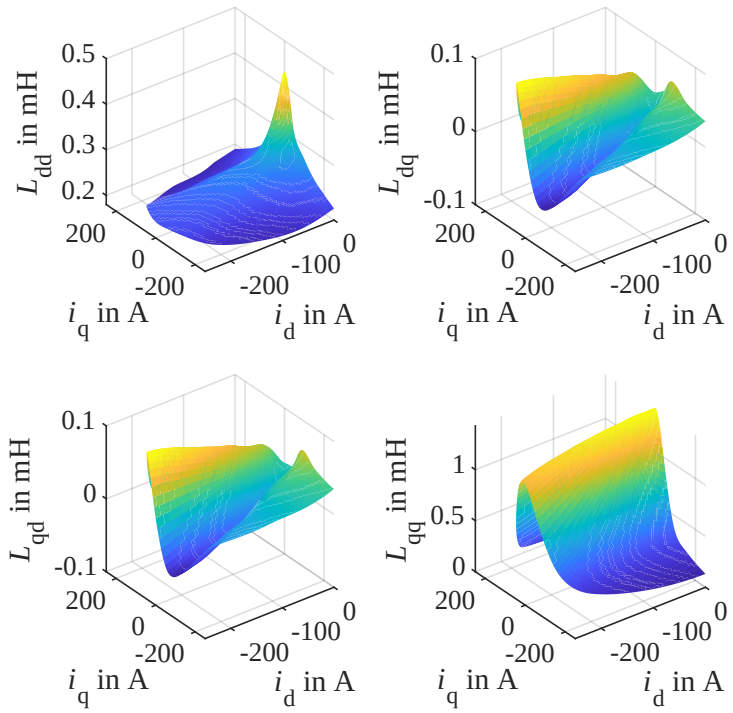

Fig. A.3: Differential inductances maps of the nonlinearly magnetized IPMSM model

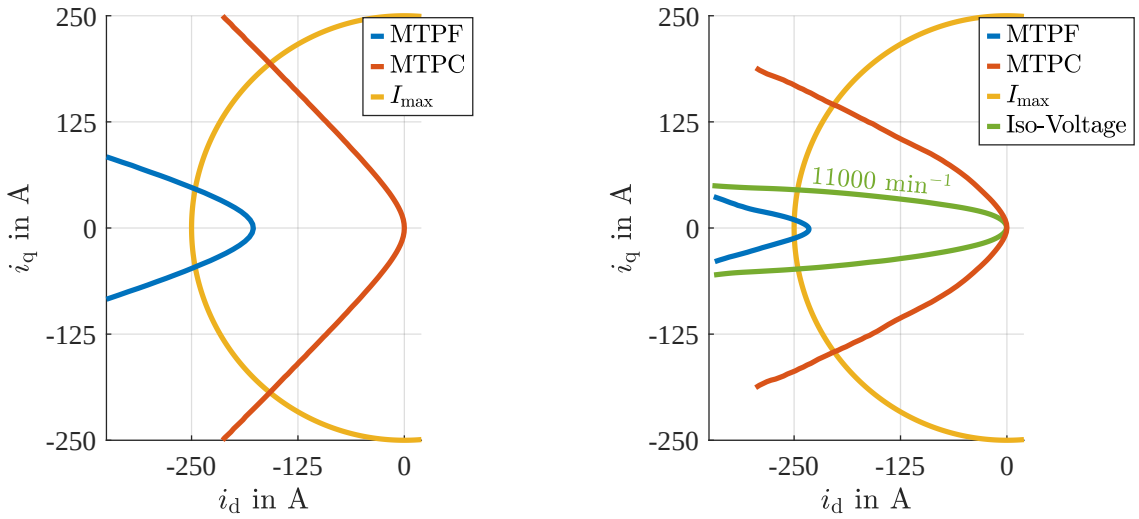

(a) Linearly magnetized IPMSM

(b) Nonlinearly magnetized IPMSM

Fig. A.4: Machine characteristic loci

B Experimental Setup

All experimental results were obtained in a test bench cabin at the Department of Power Electronics and Electrical Drives of the Paderborn University which is depicted in Fig. B.1.

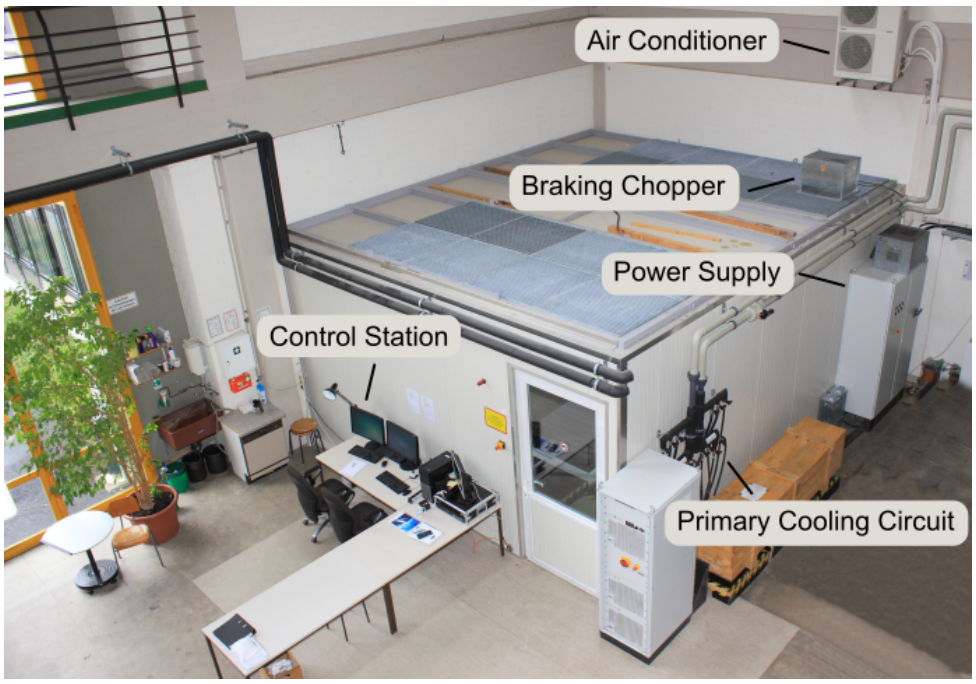

Fig. B.1: Test bench cabin [99, derivate of Fig. 8.1]

The electrical drive system under test consists of a water-cooled highly-utilized IPMSM (Brusa: HSM1-6.17.12-C01) for automotive applications and a two-level IGBT inverter (Semikron: 3×SKiiP 1242GB120-4D). The parameters, flux linkages, and differential inductances of the test IPMSM can be seen in Tab. A.3, Fig. A.2, and Fig. A.3. A speed-controlled IM that is mechanically coupled to the test motor via the shafts with a torque sensor acts as load (machine), see Fig. B.2. The nominal nameplate parameters of the load IM (Schorch: LU8250M-AZ83Z-Z) are listed in Tab. B.1. Due to the high rated power and its wide speed range, the load IM is able to reach every possible operating point of the test IPMSM and can provide highly dynamic speed changes. The schematics of the testbench, i.e., speed-controlled load and torque-controlled test drives are shown in Fig. B.3. Due to the coupled DC-links of load and test machine via a DC-DC converter, only the losses of both drives must be compensated by the AC-DC rectifier during stationary operation. Thanks to the DC-DC converter, the DC-link voltage of the test machine can be varied between 6 V and 600 V. However, in this work the DC-link voltage reference of the DC-DC converter is 360 V for all experimental investigations.

Both drives are equipped with dSPACE rapid control prototyping systems for a fast and flexible model-based design of the control algorithms. The test machine is controlled by the dSPACE DS1006MC system. It is worth noting that only one of the four processor cores was used in this work. All measurements have been obtained using dSPACE analog-to-digital converters synchronized with the control task and the switching of the inverter. Therefore, flux linkage,

Fig. B.2: Test bench with load machine (IM) and test machine (IPMSM) [8, derivate of Fig. 16]

Tab. B.1: Nameplate parameters of the load IM

IM	Schorch LU8250M-AZ83Z-Z
Nominal power	260 kW
Nominal torque	500 Nm
Nominal voltage	400 V
Nominal current	480 A
Nominal speed	4970 min^{-1}
Maximum speed	12 300 min^{-1}
Pole pair number	1

torque, and current harmonics induced by the switching of the inverter are not visible in the figures of the experimental results. For all investigations in this thesis, a controller sampling time of $T_\mathrm{s} = 62.5\,\mu\mathrm{s}$ is chosen, which leads to a switching frequency in the linear modulation range ($m < 0.907$) of $f_\mathrm{sw} = 8\,\mathrm{kHz}$. In the overmodulation range, the switching frequency decreases with increasing modulation index due to voltage limitations. Furthermore, the torque shown in the figures of the experimental results is not directly measured by a torque sensor, but estimated using (2.12). The reliance on the air gap torque estimation (2.12) instead of the direct shaft torque measurement can be justified for two reasons:

- Highly dynamic experiments are investigated in this work and, therefore, the moment of inertia of the rotor shaft as well as the limited bandwidth of the torque sensor distort the measurement.
- Due to the finite stiffness of the connected motor shafts, mechanical resonance frequencies occur that can be excited by the torque harmonics in the overmodulation range, further distorting the torque measurement results.

The most important inverter and test bench parameters are summarized in Tab. B.2.

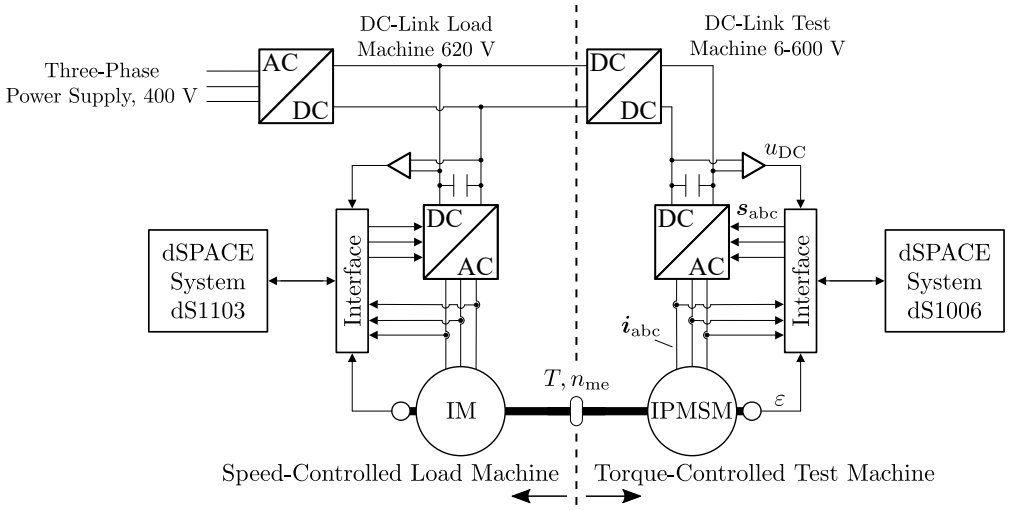

Fig. B.3: Test bench schematics [100, derivate of Fig. 6.30]

Tab. B.2: DC-link, inverter, and test bench parameters of the test drive (cf. Fig. B.3)

DC-link	Gustav Klein	
Topology	DC-converter	
DC-link capacitance	29 mF	
Rated power	200 kW	
Inverter	3×SKiiP 1242GB120-4D	
Topology	Voltage-source inverter 2-level, IGBT	
Inverter interlocking time	T_i	3.3 µs
Switching frequency ($m < 0.907$)	f_s	8 kHz
Controller hardware	dSPACE	
Processor board	DS1006MC, 4 cores, 2.8 GHz	
Sampling time	T_s	62.5 µs
Measurement devices		
Oscilloscope	Tektronix MSO58	
Current probes (zero-flux transducers)	3×Yokogawa, 500 A, 2 MHz	
Torque sensor	HBM, T10FS, 2 kNm	